Downloaded from orbit.dtu.dk on: May 05, 2023

DTU Library

Intermediate Temperature Steam Electrolysis with Phosphate-Based Electrolytes

Prag, Carsten Brorson

Publication date:
2014

Document Version
Publisher's PDF, also known as Version of record

Link back to DTU Orbit

Citation (APA):
Prag, C. B. (2014). *Intermediate Temperature Steam Electrolysis with Phosphate-Based Electrolytes*. Department of Energy Conversion and Storage, Technical University of Denmark.

General rights
Copyright and moral rights for the publications made accessible in the public portal are retained by the authors and/or other copyright owners and it is a condition of accessing publications that users recognise and abide by the legal requirements associated with these rights.

- Users may download and print one copy of any publication from the public portal for the purpose of private study or research.
- You may not further distribute the material or use it for any profit-making activity or commercial gain
- You may freely distribute the URL identifying the publication in the public portal

If you believe that this document breaches copyright please contact us providing details, and we will remove access to the work immediately and investigate your claim.

Technical University of Denmark

Intermediate Temperature Steam Electrolysis with Phosphate-Based Electrolytes

PhD thesis

Carsten Brorson Prag

Kgs. Lyngby
October 10th 2014

Proton Conductors Group
DTU Energy Conversion
Technical University of Denmark

DTU Energy Conversion
Department of Energy Conversion and Storage

Author:
Carsten Brorson Prag

Supervisor:
Professor Niels J. Bjerrum
Co-supervisors:
Senior Researcher Erik Christensen
Associate Professor Qingfeng Li
Associate Professor Irina Petrushina

Date of submission:
October 10th 2014
Revised on:
February 2nd 2015

This work recieved financial support from The Danish Council for Strategic Research through the MEDLYS project.

Proton Conductors Group
DTU Energy Conversion
Technical University of Denmark
Kemitorvet building 207
2800 Kgs. Lyngby
Denmark

www.pro.ecs.dtu.dk
Tel:(+45) 45252312
Fax:(+45) 45883136
E-mail: cbrpr@dtu.dk

ISBN 978-87-92986-29-0

Abstract

Water electrolysis for hydrogen production has been predicted to play a prominent role in the energy system of the future. Current low temperature technologies rely on expensive noble metal catalysts and high temperature systems requires special construction materials to withstand the high temperatures. Electrolysis in the intermediate temperature (IT) region (200-400 °C) is of interest as it would allow for the use of non-noble metal catalysts, due to the improved kinetics, and a wide range of construction materials as a result of the more benign temperature. At these temperatures water is supplied as steam.
This work centred on the design and development of a novel steam electrolysis concept based on phosphate electrolytes capable of operating in the IT range. Central for the work was the selection and evaluation of the materials and components for the test setup and cells as well as the technological issues and challenges faced.
A setup suitable for intermediate temperature electrolysis has been constructed in order to accommodate testing in the IT region. This included the evaluation of multiple generations of components such as end plates and flow plates. Chemical vapour deposition of tantalum was used to protect stainless steel components from the highly oxidative environment of the oxygen side of the electrolyser. While such protection should not be necessary on the hydrogen side, it was found that the best results were obtained using tantalum coated stainless steel flow plates not only on the oxygen side but at the hydrogen side as well.
Additional key steps and components for electrolysis testing are detailed in this thesis. This includes gas diffusion layers (GDL), sealing, cell assembly techniques, test operation, electrolytes and electrocatalysts.
Gas diffusion layers of carbon with a PTFE bound micro-porous layer was used for the cathode side and tantalum coated stainless steel felt was used for the anode side due to the need of corrosion protection. For the cathode side a platinum electrocatalyst was used as benchmark (Pt-black $\approx$ 8 mg/cm^2) and iridium oxide was used for the anode ($\approx$ 3 mg/cm^2). Symmetrical cell testing for hydrogen pumping at 200 °C revealed the cathode gas diffusion layers to be unstable over time. After 60 hours, the electrode resistance was more than tripled. The most prominent reason for this was thought to be a softening of the PTFE in the cathode micro-porous layer.
CsH_2PO_4 and $Sn_{0.9}In_{0.1}P_2O_7$ were used as proof-of-concept electrolytes, with emphasis on the latter electrolyte. Evaluation of electrolysis cells with these electrolytes was done with a range of tools constantly under development. These tools included regression analysis of I-V curves, reference electrode measurements and electrochemical impedance spectroscopy (EIS). While reference electrode measurements were found hard to optimise, EIS, and especially complex non-linear least-square (CNLS) fitting, was found very useful. CNLS allowed for the estimation of electrolyte resistance and polarisation resistances giving a detailed view of the novel system.
Electrolysis with CsH_2PO_4 as electrolyte revealed a need for steam on both

cathode and anode in order to prevent dehydration of the electrolyte. Additional stabilisation in the form of SiC fibres was found to increase longevity considerably. Highest achieved current density was 60 mA/cm^2 at 2.0 V and 250 °C.

Measurements using $Sn_{0.9}In_{0.1}P_2O_7$ as electrolyte, Pt black as cathode electrocatalyst and IrO_2 as anode electrocatalyst gave current densities as high as 313 mA/cm^2 at 1.9 V and 200 °C. The stability of the electrolyte was found to be high at 200 °C and a water partial pressure of 0.05 atm. For stabilisation of the electrolyte at 250 °C a higher water partial pressure is needed. Variation of temperature from 200-250 °C showed both signs of activation of electrode processes and electrode degradation.

Efforts were done to optimise the synthesis of $Sn_{0.9}In_{0.1}P_2O_7$ in order to establish a reproducible synthesis procedure. The synthesis used in this work required two heat treatment steps. Fourier transform infrared spectroscopy (FT-IR) shows an O-H band in the IR spectrum from 1500 cm^{-1} to 3800 cm^{-1} strongly dependent on the first heat treatment step of the synthesis. It was found that initial heating of the synthesis precursors to 270 °C gave a high quality sample in a reproducible fashion.

Investigations of two additional novel phosphates was attempted. These were phosphoric acid treated $Nb_5P_7O_{30}$ and a mixture of $Bi_2P_4O_{13}$, $BiPO_4$ and 2 wt.% Polybenzimidazole (PBI). Both were found to be lacking in stability.

As a central attraction of IT electrolysis is the possible use of non-noble electrocatalysts such materials were tested using $Sn_{0.9}In_{0.1}P_2O_7$ as an electrolyte. Tungsten carbide was tested as an alternative cathode electrocatalyst. Two samples were prepared by carburisation and tested. One prepared from WO_3 and one prepared from W_2N. Current densities at 1.9 V were measured as high at 129 mA/cm^2 and 73 mA/cm^2 for the two samples respectively. While WC gave lower performance than Pt black its stability was found to be higher. Furthermore, testing WC and Pt black at increasing temperatures revealed an increase in performance for a WC cathode but a decrease for a Pt black electrode. This bodes well for the further use of WC as cathode electrocatalyst.

Ni foam tested as a cathode electrocatalyst showed fair stability but lacked activity. Ni was tested as anode electrocatalyst as well. Here it showed low activity and poor stability. $LaNiO_3$ was tested as cathode electrocatalyst where it was found to be lacking in activity. It was however stable over polarisation indicating the possible use of similar materials in this role.

Resumé

Brintproduktion via vandelektrolyse er blevet spået en central rolle i fremtidens energisystem. Dog kræver lavtemperaturteknologier inden for dette felt brug af dyre ædelmetalkatalysatorer og højtemperatur systemer kræver særlig konstruktionsmaterialer for at kunne modstå høje temperaturer. Elektrolyse i mellemtemperaturområde (200-400 °C) er af interesse, da det ville give mulighed for at anvende ikke-ædelmetalkatalysatorer på grund af forbedret kinetik samt tillade anvendelse af en bred vifte af konstruktionsmaterialer som følge af en mere godartet temperatur. I dette temperature område vil vand brugt til elektrolyse optræde i form af damp.
Denne afhandling beskriver et indledende studie af elektrolyse i mellemtemperaturområdet hvor fosfatbaserede materialer er blevet brugt som protonledende elektrolytter. Centralt i arbejdet var udvælgelsen og evalueringen af materialer og komponenter brugt i såvel elektrolyseopstillingen som elektrolysecellerne. Ligeledes blev der fokuseret på teknologiske udfordringer mødt i arbejdet.
En elektrolyseopstilling designet til brug i mellemtemperaturområdet blev bygget med henblik på anvendelse i mellemtemperaturområdet. Dette arbejde inkluderede en udvælgelse af komponentdesigns for komponenter så som endeplader og flowplader. Komponenter beregnet til anvendelse på oxygen siden af opstillingen blev beskyttet mod korrosion ved hjælp af kemisk dampudfældning af tantal. Dette var nødvendigt pga. det stærkt oxiderende miljø på denne elektrode. Denne form for beskyttelse burde ikke være nødvendig på hydrogen elektroden. De bedste resultater blev dog opnået ved brug af tantal belagte rustfrit stål flowplader på brintsiden af systemet såvel som iltsiden.
En gennemgang af komponenter så som gasdiffusionslag, pakninger, elektrolytter og elektrodematerialer er givet i denne afhandling. Derudover behandles samling af celler og test parametre.
På hydrogensiden af systemet blev et gasdiffusionslag på carbon brugt. Dette bestod af et mikroporøst carbonlag med Teflon som binder. Et tantalbelagt rustfritstål filt blev anvendt til anodesiden da beskyttelse mod det oxiderende miljø er nødvendigt. En platin elektrokatalysator blev som udgangspunkt anvendt på katodesiden (Pt loading ≈ 8 mg/cm^2) og iridiumoxid blev anvendt på anodesiden (≈ 3 mg/cm^2).
Gasdiffusionslaget på katodesiden var ustabilt over tid. Dette blev set vha. et brintpumpe forsøg på en symmetrisk celle ved 200 °C. Elektrodemodstanden mere end tredoblede over 60 timers forsøg. Dette skønnes hovedsageligt at skyldes en blødgøring af Teflonen i det mikroporøse lag på katoden.
CsH_2PO_4 og $Sn_{0.9}In_{0.1}P_2O_7$ blev brugt til at demonstrere den praktiske udførelse af elektrolyse i mellemtemperatureområdet. Den største vægt blev lagt på $Sn_{0.9}In_{0.1}P_2O_7$. Elektrolysecellerne blev evalueret med en række værktøjer. Her kan nævnes regressionsanalyse of I-V kurver, referenceelektrodemålinger og elektrokemisk impedansspektroskopi (EIS). Det viste sig at være svært at optimere referenceelektrodemålingerne. EIS blev fundet højst brugbart, specielt ved anvendelse af complex non-linear least-square (CNLS) fitting. CNLS tillod estimering af elektrolytmodstanden og polarisationsmodstanden i cellerne.

Dette gav et grundigt indblik i disse nye elektrolysesystemer.
Elektrolyse med CsH_2PO_4 som elektrolyt viste sig at kræve damp på både katoden og anoden for at undgå dehydrering af elektrolytten. Yderligere stabilisering af elektrolytten ved tilsætning af SiC fibre øgede levetiden betydeligt. Den højeste opnåede strømtæthed var 60 mA/cm^2 ved 2.0 V og 250 °C.
Strømtætheder på 313 mA/cm^2, ved 1.9 V og 200 °C blev opnået for elektrolyseceller med $Sn_{0.9}In_{0.1}P_2O_7$ som elektrolyt, platin som katodeelektrokatalysator og IrO_2 som anodeelektrokatalysator. Stabiliteten af elektrolytten ved 200 °C og et vanddamptryk på 0.05 atm var høj. Det blev dog fundet at dette vanddamptryk ikke var nok til at sikre en stabil elektrolyt ved 250 °C. Test ved gradvist hævet temperature (200-250 °C) viste både tegn på aktivering af processerne i elektroderne samt degradering af selvsamme.
Optimering af syntesevejen for fremstilling af $Sn_{0.9}In_{0.1}P_2O_7$ blev udført. Syntesen af dette materiale kræver varmebehandling af to omgange. En sammenhæng imellem temperaturen brugt i den første varmebehangling og et bånd i IR-spektrummet (1500 cm^{-1} til 3800 cm^{-1}) viste sig at være tilstede. De bedste resultater blev opnået ved en temperature på 270 °C.
To yderligere elektrolytter blev forsøgt anvendt. Det drejede sig om phsophorsyrebehandlet $Nb_5P_7O_{30}$ og en blanding af $Bi_2P_4O_{13}$, $BiPO_4$ og 2 wt.% Polybenzimidazole (PBI). Begge materialer udviste mangelfuld stabilitet.
Da en central fordel ved elektrolyse i mellemtemperaturområdet er den potentielle anvendelse af elektrokatalysatorer som ikke er ædelmetaller blev sådanne alternative elektrodematerialer undersøgt. Wolframkarbid blev undersøgt med henblik på anvendelse som katodeelektrokatalysator. To wolframkarbid prøver blev testede med $Sn_{0.9}In_{0.1}P_2O_7$ som elektrolyt og IrO_2 som anodeelektrokatalysator. Den ene var fremstillet ved opkulning af WO_3 og den anden ved opkulning af W_2N. Strømtætheder på 129 mA/cm^2 og 73 mA/cm^2 blev målt ved 1.9 V for de to prøver henholdsvis. Disse strømtætheder var lavere end hvad var set for platinelektroder. Dog var wolframkarbidelektroderne mere stabile end platinelektroderne. Samtidig udviste de højere aktivitet ved højere temperature, modsat platinelektroderne. Dette tyder godt for videre anvendelse af wolframkarbid som katodeelektrokatalysator i vanddampelektrolyse.
Nikkel blev undersøgt som en katodeelektrokatalysator. Nikkel udviste en hæderlig stabilitet, men dårlig aktivitet. Nikkel blev også undersøgt som anodeelektrokatalysator. Her blev det fundet uvirksomt. $LaNiO_3$ blev undersøgt som katode elektrokatalysator. Det udviste mangelfund aktivitet men var stabilt over polarisation. Dette tyder på at andre lignende materialer ville kunne bruges i denne funktion.

Preface

The work presented in this PhD thesis was conducted from September 15^{th} 2011 to October 10^{th} 2014 in the Proton Conductors Group at DTU Energy Conversion.

First and foremost I would like to extend my gratitude to my main supervisor Professor Niels J. Bjerrum for granting me the opportunity to further my studies in this group. Further thanks goes to Associated Professor Qingfeng Li and Associated Professor Irina Petrushina for support and fruitful conversations along the way. I would especially like to thank Senior Researcher Erik Christensen for his invaluable insights and the endless amounts of time he spent helping me find my way in this maze of a project.

I would also like to thank all the co-workers in the Proton Conductors Group who helped me with my practical work and put up with my constant bothering: Chao Pan, Claus Burke Mortensen, Larissa Serup, Lars Nilausen Cleemann, Mo Hongling and Steen Blichfelt. Without your help this thesis would have been a lot shorter.

My gratitude goes to Simon Meyer and Professor Klaus Köhler from the Technical University of Munich for assistance with tungsten carbide samples and worthwhile discussions during the MEDLYS meetings. I am likewise grateful for the collaboration with Daniel Risskov Sørensen from the University of Southern Denmark in the investigation of silicon carbide stabilisation of caesium dihydrogen phosphate and the amorphous phase in tin indium pyrophosphate by ^{31}P NMR. A large thank you is also due to Troels Lie-Andersen and Erik Pristed Jensen who laid the foundation of the investigation of tin pyrophosphates. This work was later expanded by Jakob Sværke who investigated the synthesis and the conductivity of doped and undoped tin indium pyrophosphate. His help was very valuable.

This kind of work can be lonely but it was made a lot less lonely by the rest of the past and present PhD students in the group: Anastasia Permyakova, Annemette Hindhede Jensen, Anton Vassiliev, Antonio García, James Mugabi, Martin Kalmar Hansen, Mikkel Rykær Kraglund, Stine Søndergaard, Tatiana Anfimova and Tonny Jakobsen. We drank coffee, discussed, argued, worked, shared our concerns and frustrations and laughed. Thank you all for helping me getting to the finish line. A special thanks goes to Søren Lyng Ebbehøj for always being ready to listen to my stories of the plight of the PhD student and sharing some of his.

Gratitude for patience and support goes to my friends and family: the Gourmet Association, the FF's, the role play gamers of Copenhagen and beyond, my kind and loving in-laws, my brother and his energetic family and my wonderful mother and father. I promise that you will all see a lot more of me from now on.

Most importantly I owe everything to my kind, loving, patient and supportive wife Marie. You have put up with a lot and helped me through all kinds of dark times. Thank you my love.

Carsten Brorson Prag

Kongens Lyngby, October 10th 2014

Contents

List of Figures

List of Tables

List of Acronyms

ΔG	Gibbs' free energy
ΔH	Reaction enthalpy
ΔH_{vap}	Evaporation enthalpy
ΔS	Molar entropy
η	Over potential
η_{an}	Anode overpotential
η_{cat}	Cathode overpotential
σ	Conductivity
σ_e	Electrolyte conductivity
E_{act}	Activation loss
E_{cell}	Cell voltage
E_{ohm}	Ohmic loss
R_{ohm}	Ohmic resistance
Z_{im}	Imaginary impedance
Z_{re}	Real impedance
CNLS	Complex non-linear least-squares
CPE	Constant phase element
CVD	Chemical vapour deposition
DMAC	Dimethylacetamide
DRT	Distribution of relaxation times
E_{rev}	Reversible voltage
E_{TN}	Thermoneutral voltage
EDS	Energy Dispersed Spectroscopy
EIA	U. S. Energy Information Administration
EIS	Electrical impedance spectroscopy

EJ	Exajoules
F	Faradays constant
FC	Fuel cell
FT-IR	Fourier transform infrared spectroscopy
GDL	Gas diffusion layer
HER	Hydrogen evolution reaction
I	Current density
I_0	Exchange current density
ICP-MS	Inductively coupled plasma mass spectrometry
IT	Intermediate Temperature
KK	Kramers-Kronig
LSM	Lanthanum strontium cobaltite
LSM	Lanthanum strontium ferrite
LSM	Lanthanum strontium manganite
MAS	Magic-angle spinning
mW_2N	Mesoporous tungsten nitride
mWO_3	Mesoporous tungsten oxide
n	number of electrons in reaction
NMR	Nuclear magnetic resonance
OER	Oxygen evolution reaction
PBI	Polybenzimidazole, Poly-[2,2′-(m-phenylen)-5,5′-bisbenzimidazole]
PEM	Proton exchange membrane/polymer electrolyte membrane
R	Gas constant
R	Resistance
R_e	Electrolyte resistance
R_s	Ohmic resistance
R_{p_1}	High frequency polarisation resistance
R_{p_2}	Low frequency polarisation resistance
R_p	Polarisation resistance

R_{tot}	Total resistance
S	Entropy
SA	Solid acid
SDU	University of Southern Denmark
SEM	Scanning electron michroscopy
SHE	standard hydrogen electrode
SOEC	Solid oxide electrolyser cell
SOFC	Solid oxide fuel cell
SSF	Stainless steel felt
Ta SSF	Tantalum coated stainless steel felt
WC	Tungsten carbide
XRD	X-ray Powder diffraction
YSZ	Yttria stabilised zirconia

PART I

INTRODUCTION

CHAPTER 1

Introduction

Energy is one of our most precious resources on a global scale. It is contested only by clean drinking water, and its scarcity will be one of the largest challenges in the history of modern society. In the years from 1971 to 2011 the global energy consumption has all but doubled[1] and recent estimates from the U. S. Energy Information Administration (EIA) predicts a further growth[2] from 2010 to 2040 by 56 %.
For more than a century, the most important energy source has been fossil fuels. We rely on coal, oil derivatives and natural gas for 84 % if our energy needs with 11 % renewable and 5 % nuclear making up the rest.[2] The depletion of fossil fuels has been predicted to hit the following decade as far back as the 1950's.[3] Advances in oil location and drilling technology has continually pushed this boundary. However, the fossil resource depletion is inevitable and we will need replacements within decades rather than centuries. Furthermore, other factors than oil and gas availability points to the necessity of shifting away from fossil fuels, some of which may very well be more pressing than the depletion itself.
One factor is the addition of greenhouse gasses to the atmosphere caused by the combustion of fossil fuels. Over the last 800.000 years, the amount of carbon dioxide in the atmosphere has oscillated between 180 ppm and 280 ppm[4] and it has been established that the mean temperature of the earth follows the amount of CO_2 in the atmosphere. At time of writing, the amount of CO_2 globally in the atmosphere is reported to be 396.33 ppm,[5] an increase of 116 ppm since the beginning of the industrial revolution. Secondly, most nations rely on energy import from foreign nations. This need could be removed by eschewing fossil fuels. Thirdly the risk of human and environmental catastrophe is increasing in tact with easily accessible oil reservoirs are being depleted.
Such concerns have prompted the Danish parliament to set ambitious goals for Denmark's future energy supply. By 2020 Denmark must have reduced its greenhouse gas emissions by 40 % (as measured against the 1990 emission levels), by 2035 heat and power generation must be entirely renewable and by 2050 every sector including transportation must be covered entirely by renewable energy sources.[6] Meeting these targets requires a fast and decisive shift to non-fossil energy systems. The most prominent alternative energy systems are based on energy from the sun e.g. solar and wind energy. It has been estimated that the earth receives 3,850,000 exajoules (EJ) of energy from the sun each year.[7] The world's primary energy consumption for 2011 has been estimated to be in the range of 370 to 565 EJ.[1,2] This corresponds to approximately 0.01 % of the yearly solar energy flux that reaches the Earth's surface. Energy is in abundance. The challenge is to harness it.
While technologies for solar and wind energy utilisation are commercially available and widely used they have limitations. The intermittent nature of the energy sources are a bad

fit for our energy consumption habits. The average pattern of consumption tends towards peak hours around dinner time and off peak hours during the night. Solar and wind energy does not follow the same pattern meaning some sort of mitigation is needed. In 2013 energy storage was proposed as the prime solution for this problem in the DTU International Energy Report.[8]
The Danish Energy Agency have in their recent report sketched out 4 different energy scenarios[9] to evaluate which routes can lead Denmark to be self-sufficient in regards to energy. The two scenarios that reaches this goal both requires hydrogen. If this goal of self-sufficiency is to be coupled with sustainability this hydrogen cannot come from traditional reforming processes. It must come from a sustainable source such as water electrolysis i.e. the electrochemical splitting of water into oxygen and hydrogen.

1.1 Intermediate temperature electrolysers

The existing electrolysis technologies operates either below 100 °C or above 500 °C. Proton exchange membrane (PEM) electrolysers operates below 100 ° and relies on expensive transition metals such as platinum and iridium for electrode materials. Alkaline electrolysis uses cheap electrode materials but have a lower performance than PEM electrolysis and requires a complex recirculation and handling system for its highly corrosive potassium hydroxide electrolyte. Solid oxide electrolysis (SOE) operates above 500 °C requiring advanced ceramic construction materials to withstand temperature cycling and the high temperature requires the system to be stationary.
Solid materials suitable for operation in the temperature gap from 200 °C to 400 °C, the so-called intermediate temperature (IT) range , would allow for the use of inexpensive transition metal electrocatalyst not available for PEM as well as a higher performance due to kinetic activation. Compared to alkaline electrolysis the electrolyte would be easier to handle and would give a higher performance as well. Compared to PEM electrolysers no liquid phase is present as water is supplied as steam. This allows for ease of handling and strongly reduces the risk of flooding of the electrodes. Lowering the temperature compared to SOE would allow for the use of cheaper construction materials such as readily available metals, alloys and plastics. Furthermore no ceramic construction components are needed.

1.2 Project objectives

The central goal of this project was to assemble and demonstrate electrolysis cells at 200 °C to 400 °C. This required the construction of a setup designed for electrolysis in this temperature range and capable of handling the harsh electrolysis conditions. This was achieved by testing and selection of construction materials through multiple iterations. Secondly, the components for the electrolysis itself needed to be selected and made into electrolysis cells ready for testing at actual electrolysis conditions. Electrolytes and electrocatalysts had to be selected and synthesised. Thirdly cheap alternative electrocatalyst materials needed to be tested in conjunction with selected electrolyte materials and gas diffusion layers (GDLs). This was considered the most prominent goal as this builds on the previ-

ous goals and the use of cheap electrocatalysts is the most alluring aspect of IT electrolysis.

1.3 Thesis outline

In Chapter 2 the thermodynamic and kinetic considerations behind electrolysis will be discussed together with a brief overview of the components of an electrolyser cell. This is followed by an introduction to the three central types of electrolysis, alkaline electrolysis, PEM electrolysis and SOE, available today.
Chapter 3 gives a literature review on the available electrolyte and electrocatalyst materials. Phosphate based electrolytes such as CsH_2PO_4, SnP_2O_7 and its aliovalent doped derivatives are discussed. Electrocatalysts such as IrO_2, Pt and WC are treated as well.
Chapter 4 gives an overview of the experimental techniques used in this work. Physicochemical techniques are considered known and only stated while electrochemical techniques are treated in more theoretical depth.
The fabrication and synthesis of components used for electrolysis in this work are detailed in Chapter 5. This includes electrolytes, electrocatalysts, GDLs, electrode inks and electrodes.
Chapter 6 treats the construction and operation of the setup used for electrolysis experiments. The choice of construction materials is discussed and the method of assembly of test cells is explained. Sealing and start-up and shut-down procedures are detailed as well. Lastly the influence of the electrolysis testing on the components of the setup is discussed.
The results of the work with pyrophosphates are reported and discussed in Chapter 7. The consequences of synthesis temperature of the electrolyte are illuminated and electrolysis results with $Sn_{0.9}In_{0.1}P_2O_7$ as electrolyte are presented.
Test results for alternative electrolytes such as CsH_2PO_4, niobium and bismuth phosphates are given in Chapter 8.
Electrode materials for anode and cathode alike are discussed in Chapter 9. Apart from platinum this includes alternative materials such as WC and Ni.
Chapter 10 gives the conclusions of this work together with thought on further works.

PART II

THEORETICAL ASPECTS

CHAPTER 2

Theory and technology

In this Chapter hydrogen production and the theoretical aspects of water electrolysis will be introduced. The material will be treated from a steam electrolysis vantage point. This is especially relevant when thermodynamics is considered. After this theoretical background has been established different technologies applying these principles in practice will be discussed.

2.1 Hydrogen production

For all practical purposes hydrogen is not found in free molecular form in Earth's atmosphere. It is however found bonded to other atoms in compounds all around us. Therefore hydrogen must be produced from such hydrogen containing compounds. In 2004 it was estimated that 96 % of the hydrogen produced was made from coal, oil and natural gas by steam reforming and partial oxidation.[10] 4 % was produced by electrolysis and the amount produced by technologies such as pyrolysis, fermentation, thermolysis and photolysis was on a global scale insignificant.
If hydrogen is to become a central energy vector production must be increased. The fossil material technologies are problematic as they require the introduction of more fossil material into the carbon cycle when hydrogen is produced. As the effect of carbon on the climate is cumulative this additional introduction of carbon is highly undesirable. The possibility of depletion of fossil fuel sources should be taken into consideration as well when the energy system of the future is designed. Additionally the technology does not interface well with renewable energy sources and their intermittent nature.
It is assumed that a central point in securing our energy supply will be the storage of hydrogen and recombination with oxygen into water in fuel cells. The hydrogen produced by steam reforming and partial oxidation has a maximum purity of 75 % before purification with CO levels between 1 and 4 %.[11] High temperature proton exchange membrane fuel cells (PEMFCs) have a hard time handling impurities at 1% CO and above[12] and for solid oxide fuel cells (SOFCs) CO may promote the formation of free carbon, called coke, on the fuel electrode.[13]
A convenient way of alleviating the problems sketched above is by electrolysis water or steam. Electrolysis gives very pure hydrogen (up to 99.9999%[14]) with no emissions and interfaces well with renewable energy sources.

2.2 Electrolysis

The concept or perhaps more accurately the application of electrolysis dates back at least 200 years. The birth of electrolysis can be said to be 1789, 1775 or the third century BC depending on preference.[15] Most agree however that when William Nicholson and Anthony Carlisle in 1800, building on the work of Alessandro Volta and the invention of the voltaic pile, made hydrogen and oxygen by electrolysis of water they started the proliferation of electrolysis.[16] Thus electrolysis has definitely been around for at least 200 years and been around since the birth of electrochemistry.
In electrolysis a direct current is passed between two electrodes through an electrolyte resulting in chemical reactions on the two electrodes. At one electrode an oxidation takes place and at the other a reduction happens. These electrodes are named the anode and the cathode respectively. In the case of water electrolysis oxygen is evolved (oxygen evolution reaction, OER) at the anode and hydrogen at the cathode (hydrogen evolution reaction, HER). If the electrolyte transports protons the whole process can be described as:

$$\begin{aligned} &\text{Anode :} && \mathrm{H_2O}(g) \rightarrow \frac{1}{2}\mathrm{O_2}(g) + \mathrm{H^+} + 2\mathrm{e^-} \\ &\text{Cathode :} && 2\mathrm{H^+} + 2\mathrm{e^-} \rightarrow \mathrm{H_2}(g) \\ &\text{Total :} && \mathrm{H_2O}(g) \rightarrow \mathrm{H_2}(g) + \frac{1}{2}\mathrm{O_2}(g) \end{aligned}$$

here written for steam electrolysis as all reactants and products are in gas phase. As oxygen is evolved at the anode and hydrogen at the cathode it is possible to isolate the two gasses from each other giving products with a purity approximating 100 % purity.[17]

2.2.1 Thermodynamics

Electrolysis of water converts electric energy into chemical energy. The energy is stored in the hydrogen produced and can be (partly) regained by a conversion back to electrical energy using a fuel cell. Electrolysis can only happen if energy is supplied. The amount of energy needed for the process is determined by the reaction enthalpy ΔH. Part of this can be supplied as heat and part of it must be supplied as electric energy. The part corresponding to electric energy is the change in Gibbs' free energy ΔG and the part that can be supplied as thermal energy corresponds to the change in entropy times the reaction temperature, T·ΔS. As electrolysis of water is not a spontaneous process and does not release heat $\Delta G > 0$ and $\Delta H > 0$. The relation between enthalpy, entropy and Gibbs' energy change is thus:

$$\Delta \mathrm{G} = \Delta \mathrm{H} - \mathrm{T} \cdot \Delta \mathrm{S} \tag{2.1}$$

These concepts are related to the voltage of an electrolysis cell the following way:

$$\mathrm{E_{TN}} = -\frac{\Delta \mathrm{H}}{\mathrm{nF}} \tag{2.2}$$

$$\mathrm{E_{rev}} = -\frac{\Delta \mathrm{G}}{\mathrm{nF}} \tag{2.3}$$

where F is Faradays constant, n is the amounts of electrons involved in the reaction, in the case of water electrolysis 2, $\mathrm{E_{TN}}$ is the thermoneutral voltage of the cell and $\mathrm{E_{rev}}$ is the

reversible voltage. The reversible voltage is the lowest amount of electric energy that must be supplied for electrolysis to happen. The thermoneutral voltage is the voltage needed if all necessary energy is to be supplied as electric energy. It is also the voltage where the process neither releases heat to nor requires heat from the surroundings. The enthalpy and entropy can be calculated by the following relation:

$$H = H^\circ + C_P \cdot \Delta T \tag{2.4}$$

$$S = S^\circ + C_P \cdot \ln \frac{T}{T^\circ} \tag{2.5}$$

where ΔT is the change from standard to reaction temperature and C_P is the specific heat capacity. Using Equation 2.4 and 2.5 together with Equations 2.1,2.2 and 2.3 the reversible and thermoneutral voltages can be calculated. Figure 2.1 shows this from 25 °C to 1000 °C under the assumption of a constant specific heat capacity for water and steam when temperature is varied.

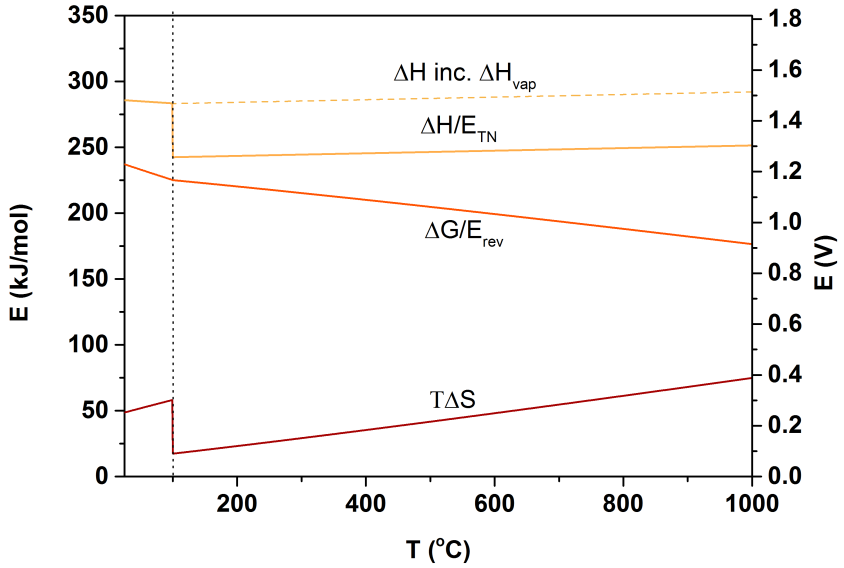

Figure 2.1: Enthalpy change, free Gibbs energy change and temperature times entropy change for an electrolysis process as a function of temperature. Also shown is the proportionality of ΔH and ΔG to the thermoneutral (E_{TN}) and reversible (E_{rev}) potential respectively.

When temperature is raised the required amount of electric energy decreases. In turn the amount of energy that can be supplied as heat rises. This is one of the attractive features of elevated temperature electrolysis. Heat is commonly available as a cheap by product from various processes. Below 100 °C the overall energy needed for the process decreases with temperature. When going from liquid water to steam an abrupt fall in energy demand is seen followed by a very slow increase. This fall may be a bit misleading. It is due to the enthalpy of evaporation of water (ΔH_{vap}) not being included. The dotted line shows the full picture as ΔH_{vap} is included. When discussing electrolysis on cell

basis ΔH_{vap} is often not included and it is assumed that pre-evaporated water is supplied. When looking at electrolysis from a system point of view this may make less sense as the energy to evaporate the water must come from somewhere. If a process supplying steam or heat at the right temperature is available e.g. as a by-product from another process ΔH_{vap} can be excluded but should be kept in mind. On any account it can, as mentioned, be supplied as heat and does not impact the fact that the electrical energy needed for the process decreases with temperature.
Assuming that all energy that can be supplied as heat is supplied this way and that steam is readily available the reversible cell voltage (E_{rev}) changes from 1.23 V at 25 °C to 1.14 V at 200°C.
The previous considerations have been under the assumption that the pressure is constant at 1 bar. If this is not the case the voltage of a cell in equilibrium, that is with no applied current, is related to the activities of the reactants and products by the Nernst equation. For the case of steam electrolysis all activities may be substituted by partial pressures:

$$E = -\frac{\Delta G}{2F} + \frac{RT}{2F} \cdot \ln \frac{p_{H_2} \cdot p_{O_2}^{\frac{1}{2}}}{p_{H_2O}} \tag{2.6}$$

2.2.2 Kinetics

The thermodynamics described above is only applicable at no applied voltage. In order to ensure an actual hydrogen production a current must be applied to the electrolysis cell. When a current is applied the voltage of the cell will rise above the reversible voltage due to kinetic losses. These are irreversibilities in the cell stemming from the different components. The total voltage of an electrolysis cell can be expressed as:

$$\begin{aligned} E_{cell} &= E_{rev} + E_{ohm} + E_{act} \\ &= E_{rev} + I \cdot R_{ohm} + \eta_{an} + \eta_{cat} \end{aligned} \tag{2.7}$$

E_{ohm} is the ohmic contributions to the cell overpotential and where I is the current density. These include contact resistance from electrodes, resistance from current collectors and especially electrolyte resistance. The latter is dominating in most instances and the ohmic resistance is from time to time assumed to be the electrolyte resistance. All these contributions add up to an overall resistance, R_{ohm}, and its contribution to the cell voltage follows the current linearly as per Ohms law. E_{act} is the activation overpotential which primarily stems from the electrode kinetics. In the case of water and steam electrolysis the anode contribution η_{an} dominates the electrode overpotential dwarfing the cathode contribution η_{cat}. The electrode overpotential arises when the electrode reactions between electrode, more specifically the electrocatalyst, and the electrolyte happens.

Figure 2.2 illustrates Equation 2.7 and its different contributions of loss when current is applied to an electrolyser cell. The losses are dominated by the ohmic loss, which is in turn dominated by the electrolyte resistance, and the anodic overpotential. While the figure is idealised it still illustrates the magnitudes of the contributions. The activation overpotentials dominates the cell at small current densities as the electrode-electrolyte processes are activated. At higher current densities the ohmic loss of the cell starts

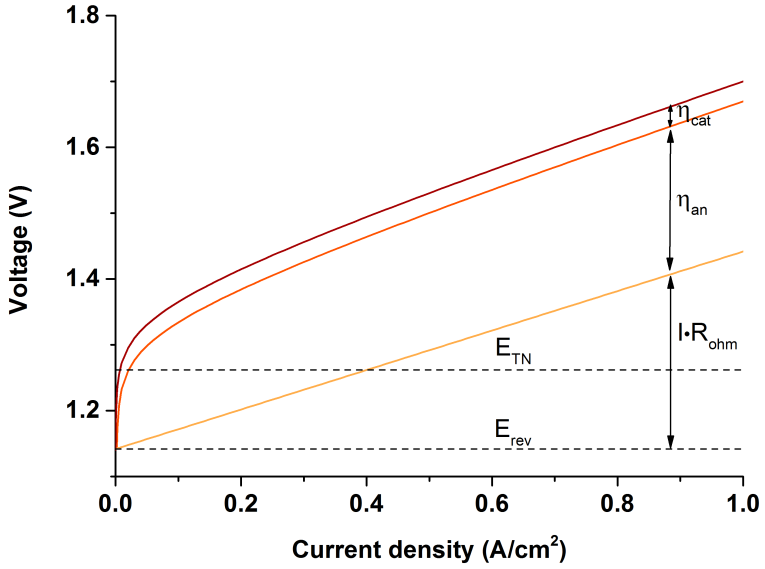

Figure 2.2: Idealised polarisation curve detailing ohmic and activation losses

dominating as it grows linearly with current density. This gives rise to the linear nature of the polarisation curve at increased current densities. Not shown here is the diffusion losses which may happen at even higher current densities. If transport of reactant to the electrode or transport of products away from the electrodes is not fast enough the voltage will rise drastically reaching a current limit where the potential rises asymptotically.
For a simple electrode reaction with sufficient reactant present and at equilibrium the relation between current density and overpotential at the electrode can be expressed by the Butler-Volmer equation:

$$\mathrm{I} = \mathrm{I}_0 \left[\exp\left(\frac{\alpha \mathrm{nF}}{\mathrm{RT}} \eta \right) - \exp\left(- \frac{(1-\alpha)\mathrm{nF}}{\mathrm{RT}} \eta \right) \right] \tag{2.8}$$

where I is the current density, I_0 is the exchange current density (the equilibrium current density), T is the temperature, R is gas constant, F is Faradays constant, n is the number of electrons exchanged in the reaction, η is the overpotential. I_0 and α are parameters linked to the kinetics of the electrode reaction. I_0 is the equilibrium current density, in the sense that it is the absolute value of the cathodic and anodic currents that cancel each other out at equilibrium. It is the current density at complete reversibility. α is a value between 0 and 1 and, as each of the parenthesis in Equation 2.8 describes one of the redox reactions on the electrode, can be seen as a measure for how much one half reaction is favoured over the other.
When going to higher anodic overpotentials away from equilibrium the Butler-Volmer equation can be simplified and rewritten as the so-called Tafel equation:

$$\eta = \frac{-2.3\mathrm{RT}}{\alpha \mathrm{nF}} \log(\mathrm{I}_0) + \frac{2.3\mathrm{RT}}{\alpha \mathrm{nF}} \log(\mathrm{I}) \tag{2.9}$$

As the anodic overpotential in steam electrolysis dominates the cathodic overpotential this expression can be used as a representation for the electrode overpotential. This expression for the overpotential at the electrodes has the general form:

$$\eta = a + b \cdot \log(I) \tag{2.10}$$

This can be exploided to do fitting of recorded polarisation curves. With the addition of a term for the ohmic resistance an expression for a polarisation curve can be found from Equation 2.10:

$$E_{cell} = A + b \cdot \log(I) + I \cdot R \tag{2.11}$$

This will be used later in this work to separate the activation contribution of a polarisation curve from the ohmic contribution. More on this in Section 4.2.1.

2.2.3 Electrolyser Cell Components

In practice an electrolyser consists of a number of components. The three main components, already mentioned above, are the anode or oxygen electrode, the cathode or hydrogen electrode and the electrolyte which is responsible for insulating the electrodes electrically, preventing gas crossover and conducting ions. The most important additional components are the gaskets, flow plates and end plates. A schematic representation of these components and their relative positioning in an electrolyser can be seen in Figure 2.3.

The electrolyte is the central component in an electrolyser. It is ionically conductive and its nature defines the rest of the electrolyser. Because of its defining character electrolyser technologies are named after the type of electrolyte used. The most prominent types of technologies are treated in the next section and their deviations from the following standard description of components will be discussed.

In general electrodes consists of a gas diffusion layer (GDL), a support or microporous layer and an electrocatalyst. An electrocatalyst is a material which lowers the activation energy of the electrochemical process taking place at the electrode without itself being consumed. As it catalyses an electrochemical process electric conductivity is highly important. Furthermore a high number of available reactive sites is desired and high surface area materials with small particle sizes are preferably used. If the material itself lacks stability e.g. its small particles sinters during operation they may be stabilised using a support. This support should be highly electronically conductive. The microporous layer is a highly porous material of small pore size, preferably a few microns or less,[18] onto which the catalyst layer is sprayed. It allows for unhindered diffusion to the electrocatalyst and supports the electrocatalyst at the same time. This is in contrast to the GDL which supports the microporous layer and has larger pores and higher mechanical strength. Its role is to allow for gas to diffuse into or out of the electrode structure and allowing for electrical contact from the electrocatalyst through the microporous layer to the flow plates. For most technologies the GDL is the structural backbone of the electrode. Apart from the mentioned parts of the electrode some electrolyte may be added to the electrode together with the electrocatalyst. The OER and HER can only happen at interfaces where electrocatalyst and electrolyte are present as the ionic species involved in the reaction has to be transported to or from the electrocatalyst surface. If no electrolyte is added to the structure the reaction can only take

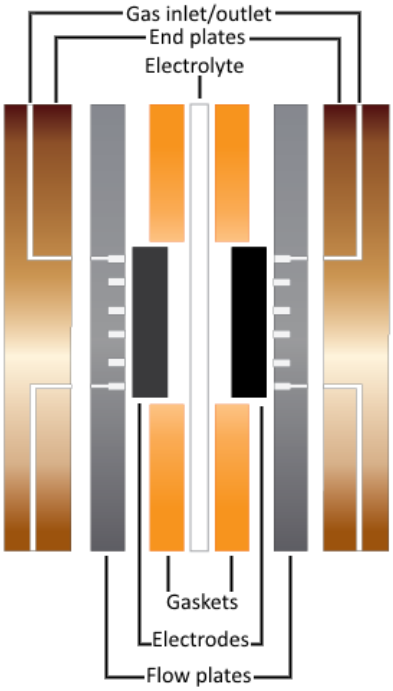

Figure 2.3: Exploded view of an electrolyser

place at the interface between the electrocatalyst and the bulk electrolyte severely limiting the performance of the electrolyser as a whole. Lastly gas must be able to evolve at these interfaces and water must be able to reach the interfaces on the relevant electrode.
The flow plates are also responsible for the electrical connection as the power source is connected directly to them. Gas flowing in from the end plates or out from the electrodes is distributed into flow channels and lead to or from the electrode structure. Lastly they support the entire electrode/electrolyte system mechanically. The end plates are responsible for gas in and out of the entire system as well as keeping the entire structure in place.

2.3 Water electrolysis technologies

2.3.1 Alkaline Electrolytes

Alkaline electrolysis is a highly mature technology based on highly alkaline solutions as electrolytes. The most commonly used is KOH at concentrations from 27 wt.% to 35 wt. % chosen for optimal conditions at a given temperature.[19,20] Temperatures are usually between 25 °C and 100°C. The electrodes are immersed in the solution and to prevent gas crossover a diaphragm separates them. Water present at the cathode side is converted to hydrogen and hydroxide ions which are consumed at the anode to form oxygen and water. The electrolyte is circulated to keep the hydroxide concentration constant.
These types of electrolysers are usually limited to fairly low current densities, such as

0.4 A/cm^2 for commercial systems and have to compensate with large active areas. This is possible as the materials used are inexpensive. The electrolyte is as mentioned KOH and the electrodes are commonly nickel coated stainless steel felt. No high surface area electrocatalyst or microporous layer is needed. Another method used to offset the low current density is operation at higher pressure, typically 25-30 bar.[20]
Previously the diaphragm was most commonly made of asbestos but due to corrosion and it being highly toxic and carcinogenic it has been replaced by materials such as Teflon® bonded potassium titanate (K_2TiO_3),[21] zirconium dioxide in a polysulfone matrix (Zirfon®)[22] and Teflon® and polysulfone diaphragms.[23]
Another direction this field has expanded into is hydroxide conducting polymer membranes. These so-called zero-gap electrolysers[24] use solid polymers allowing for direct contact between the electrode and the membrane. This limits the distance between the two electrodes and reduce the ohmic resistance considerably. A study using such a membrane reported a stable current density of 1A/cm^2 at 2.12 V,[25] 60 °C and ambient pressure.
Finally stabilisation of the liquid electrolyte in matrices has been done. Allebrod et al.[26] demonstrated a current density of 1 A/cm^2 at 1.5 V with immobilised KOH in mesoporous $SrTiO_3$ at 250 °C and 42 bar. The cell used very cheap materials such as a nickel foam anode and an Inconel foam cathode.

2.3.2 PEM Electrolysis

Proton exchange membrane or polymer electrolyte membrane (PEM) water electrolysis is defined by a thin (20 μm to 200 μm) proton conducting polymer electrolyte. Water is fed to the anode where oxygen is evolved. Protons are transported over the membrane to the cathode where hydrogen gas is evolved.
The most widely used membrane is Nafion®. This membrane relies on the protonic conductivity of water and water is retained in the membrane. Sulphonic acid functional groups in the membrane are responsible for this retention of water. Conductivity for this membrane has been reported as high as $7.8{\cdot}10^{-2}$ S·cm^{-1}.[27] Current densities as high as 2 A/cm^2 can be reached[17] and systems can be pressurised to 30 bar.
The low membrane thickness can be achieved due to a very low gas permeability of the materials and the purity of hydrogen evolved is commercially reported as high as 99.9999%.[14]
Among the more negative aspects of PEM is the need for expensive noble metal electrocatalysts, a need created by the hostile electrolysis environment. The anode usually uses IrO_2 or $Ir_xRu_{1-x}O_2$ and the cathode uses Pt as electrocatalyst. All are very expensive, Iridium in particular as it can only be obtained as a bi-product in platinum mining. The hostile environment calls for expensive building materials as well. Expensive sintered titanium GDLs have traditionally been used on the anode as the highly oxidative environment corrodes the commonly used carbon materials.
Another limit is temperature. With the existing membranes all electrolysis is confined to temperatures below 100 °C i.e. water electrolysis. This excludes cheap alternative electrocatalyst materials which would function at higher temperature. Raising the temperature would also allow for more effective electrolysers. Steam electrolysis with alternative membranes such as Poly-[2,2′-(m-phenylen)-5,5′-bisbenzimidazole] (PBI) [28] and Aquivion™[29] has been attempted. Hansen et al.[29] reached a current density of 700

mA/cm^2 at 1.775 V with a phosphoric acid impregnated Aquivion^{TM}membrane (50 μm) at 130 °C.

2.3.3 Solid Oxide Electrolytes

So far the only viable steam electrolysis technology is solid oxide electrolyser cells (SOECs). This technology operates between 600 °C and 900 °C. The electrolytes used conducts oxide ions and steam is fed to the cathode of the system. Here hydrogen is evolved and oxide ions are conducted to the anode where oxygen is evolved. The most commonly used electrolyte is yttria (Y_2O_3) stabilised zirconia (ZrO_2) (YSZ) thin films of 10-15 μm thickness.[30] These ceramic layers are very dense even at low thickness. The oxide ion conductivity of YSZ is highly dependent on the temperature[31] and zirconia stabilised with 8 mol% yttria can go from $5.9 \cdot 10^{-4}$ S·cm^{-1} at 600 °C to $3.8 \cdot 10^{-2}$ S·cm^{-1} 1000 °C. Ceramics like these allow for very thin dense electrolyte layers and operation at lower temperatures is still viable for this reason, even with the diminished conductivity.
The electrodes are commonly composites of the electrolyte with an electrocatalyst formed into thin porous layers (10-15 μm) with percolating networks of electrocatalyst and electrolyte. This structure allows for utilisation of a larger volume of the electrode in the electrochemical reaction. Cathodes are usually Ni/YSZ composited where the Ni is introduced as NiO and reduced in situ to metallic nickel. The anodes are commonly composites of electrolyte and perovskites doped with strontium. Commonly used materials include strontium doped $LaMnO_3$ (LSM), $LaFeO_3$ (LSF) and $LaCoO_3$ (LSC).
The high operation temperature allows not just for steam electrolysis but also electrolysis of CO_2 to CO[32] and co-electrolysis[33] where CO_2 and water is converted to a mixture of H_2 and CO called syngas. This gas mixture can be used as a precursor for synthesis of hydrocarbons.
Most SOECs are solid oxide fuel cells (SOFCs) operated under reverse conditions and it has been determined that they are much more prone to degradation in this reverse operation mode.[34] While sudden failure is rarely observed delamination of the ceramic layers and poisoning of the cathode with silica from the sealing have been seen to cause degradation over time. For commercial cells degradation rates as high as 16% per 1000 hours has been reported.[35] The highly oxidative environment on the anode has also been proposed as detrimental to the ceramic components in general.
The system components need to be able to withstand the high temperature. This requires highly specialised building materials. Also the high temperature makes the system stationary of nature. Even if the issues with degradation could be solved these systems will not be viable for mobile applications.

CHAPTER 3

Electrolyte and electrode materials

3.1 Ionic conductors

As mentioned in Section 2.2.3 the defining component of an electrochemical cell is the electrolyte. This component defines operation conditions such as temperature and pressure and it dictates which materials can be used for additional components such as electrodes. In the case of an electrolyser cell it also stipulates the materials for gaskets, flow plates, cell housing, whether an electrolyte recycling system is needed and more. As such it is important to select the correct electrolyte as exchanging it may require a complete reworking of the system.
A lot of demands are put on the electrolyte. The most important are the following:

- Ionically conductive — If the ions cannot move from electrode to electrode no reaction happens. The higher the conductivity the thicker the electrolyte may be without the ionic transport being the bottleneck. Ionic conductivity is much harder to optimise than electrode performance so it is better to optimise the electrodes to fit the electrolyte than the other way round.
- Electronically insulating — If the electrons can move through the electrolyte the electrodes will short circuit and the desired reaction will not happen. A small amount of electronic conductivity can be accepted and is sometimes hard to avoid.
- low gas permeability — Gas crossover can lower the potential of the cell giving falsely enhanced "performance" results. Additionally it will lead to impure gas and possible danger if a combustible mixture of H_2 and O_2 is formed.
- Chemically stable — Electrolysis conditions are harsh and the electrolyte must be able to withstand oxidising and reducing environments, elevated temperature, possibly high or low pH and high potentials.
- Mechanically stable — This ties into ionic conductivity and gas permeability especially. The electrolyte must be thin enough to allow for a good performance but may not allow for gas to travel through. It must also be dimensionally stable during heating and not become soft or brittle. All of these would lead to failure of the cell.

When investigating novel electrochemical methods the first point of focus is the selection of a suitable electrolyte. In the case of water and steam electrolysis this electrolyte must be an oxide ion conductor, a protonic conductor or a proton conductor.

3.1.1 Conductivity mechanisms

In general terms there are two types of conductivity mechanisms when it comes to transport of protons. The Grotthuss mechanism and the vehicle mechanism.[36] For reasons that will be made clear these two mechanisms will also be termed proton and protonic transport respectively. While there are a host of transport pathways on a more detailed level they all fall into one of these two categories on a higher level.

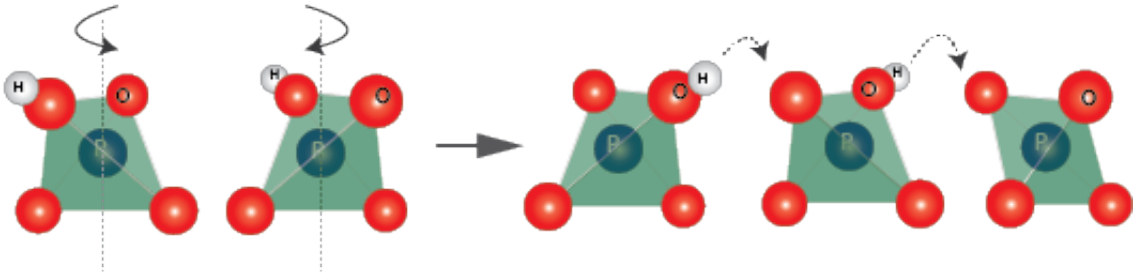

Figure 3.1: The Grotthuss mechanism as seen for PO_4. Rotation of PO_4 tetrahedra allows for hydrogen bond delocalisation and thus makes proton hopping possible.

The Grotthuss mechanism is the transport of protons between two stationary but freely rotating host species. As such it is a transport of free, or more precisely unaccompanied, protons and we call it proton transport. This mechanism was first suggested by von Grotthuss in 1806[37] as an explanation for the transport of charge during electrolysis of water. Hydrogen bonds are constantly reorganised at a fast pace and if a proton is bonded to a freely rotating species it may come into close enough contact with another anion to become delocalised. This may trigger the delocalisation of a second proton bonded to the second species leading to a "swap" of protons as seen in Figure 3.1. Thus, while it is not the same proton travelling from one end of this chain to another there is a net transport of protons. In high temperature proton conductors such as perovskites a similar mechanism is responsible for proton transport. Incorporation of water or hydrogen into the crystal lattice gives mobile protons on lattice oxygen which can move from oxygen to oxygen.[38] The mechanism of incorporation for water is as follows:

$$H_2O\,(g) + O_O^x + V_O^{\cdot\cdot} \rightarrow 2OH_O^{\cdot} \tag{3.1}$$

Where O_{O^x}, $V_O^{\cdot\cdot}$ and $OH_O^{\cdot}$ denote a lattice oxide ion, an oxygen vacancy and a hydroxyl ion respectively. An important fact surrounding this mode of transport is that it does not require any presence of a mobile charge carrier and it is thus the most prominent mechanism for conduction in anhydrous environments.
The vehicle mechanism relies on the mobility of various charged species for the transport of protons. The protons are incorporated into a molecule which in turn moves by electronic interactions. The protons are accompanied by a molecule. Since the protons do not move themselves from molecule to molecule this type of transport is titled protonic. While the net effect of the mechanism is a transport of protons they themselves are merely passengers. The moving species may be proton carriers such as H_3O^+, NH_{4+}, OH^- or HS^-. In water based systems, apart from the hydronium ion, it is ions such as the Zundel ($H_5O_2^+$) and Eigen ($H_9O_4^+$) cations that are involved in the transport.[39] The

more detailed explanation on how this transport occurs is still disputed[40] and a topic currently investigated by computational chemists. The vehicle mechanism is the transport mechanism seen in fluids and by extension the transport mechanism of PEM electrolytes.

3.2 Phosphate based electrolytes

Suitable solid non-polymer proton conducting electrolytes for IT operation are not abundant. However, one class (or collection of classes) of compounds have shown some promise the last decade and a half: the phosphate based electrolytes. This is not a homogeneous group of materials. While they differ structurally, mechanically and in regards to conductivity mechanism they all show high proton(ic) conductivity in some part of the lower intermediate temperature range (200-270 °C). Among these compounds are solid acids (SA) such as CsH_2PO_4, mixed phosphate compounds such as the niobium phosphates and pyrophosphates such as SnP_2O_7. Most of them owe their high conductivity at intermediate temperature to phosphoric acid in some way. The exception is the solid acids where a structural changes at elevated temperatures are responsible for the conductivity.
In the literature the compounds detailed in this section have mostly been investigated in a fuel cell context. In seldom cases electrolysis have been tried. Thus by necessity these next pages will concern themselves with fuel cells more than with electrolysis.

3.2.1 Caesium dihydrogen phosphate

Solid acids are materials with a behaviour lying in between those of actual acids and normal salts. Their structure is typical one of oxyanions linked together by O···H interactions. Prominent among these oxyanions are SO_4 and PO_4. Compounds of the general formula MH_nXO_4 (M = Cs, NH_4 and Rb; X = S and P) began gathering attention in regards to fuel cell application when Haile demonstrated an anhydrous cell with an $CsHSO_4$ electrolyte[43] running at 160°C. This class of compounds undergoes a phase transition at elevated temperatures leading to a greatly increased proton conductivity (e.g. $\approx 3{\cdot}10^{-6}$ to $\approx 5{\cdot}10^{-3}$ S·cm^{-1} for $CsHSO_4$).[44] This superprotonic material state and the fact that the cell worked anhydrously drew attention. $CsHSO_4$ unfortunately turned out to react with hydrogen to form H_2S[45] leading to a switch of focus to CsH_2PO_4.[41] This material has a phase transition at $\approx$ 230 °C raising the conductivity from $8.5{\cdot}10^{-6}$ to $1.8{\cdot}10^{-2}$ S·cm^{-1} [46] making it ideal for IT operation.
CsH_2PO_4 has degradation behaviour which is highly dependent on humidity.[47,48] It may polymerise as by the following expression:

$$CsH_2PO_4 \leftrightarrow Cs_2H_2P_2O_7 \leftrightarrow CsPO_3 \tag{3.2}$$

At low partial pressures of steam this may happen in the region where conductivity is seen to begin. This has previously caused some controversy as some authors believed the dehydration to be the origin of the conductivity.[49] The general consensus has however settled on the dehydration products not being responsible for the increased ionic conductivity. Instead it is the increased freedom of rotation of the phosphate groups that at elevated temperature gives rise to fast proton hopping.[50] The dehydration and subsequent decomposition of CsH_2PO_4 does create a need for hydration during operation as can be

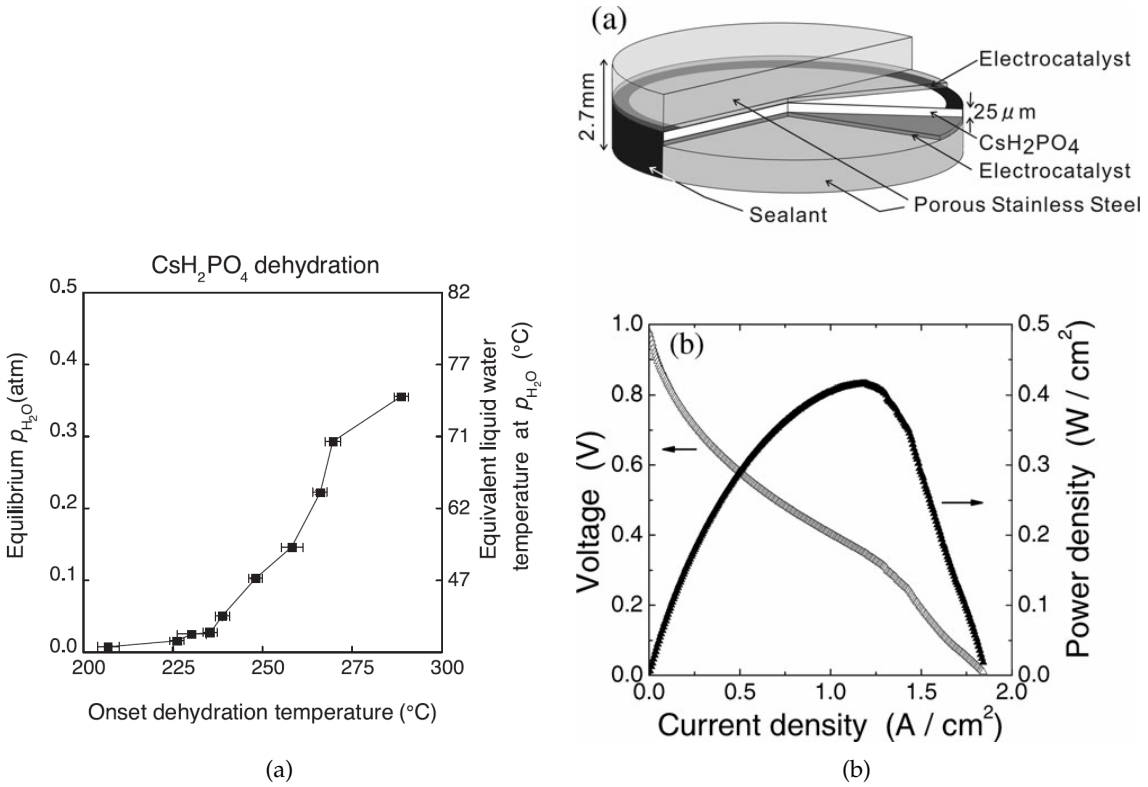

Figure 3.2: (a) Dehydration of CsH_2PO_4 is highly dependant of water partial pressure and can be suppressed up to 280 °C with p_{H_2O}= 0.35 atm.[41] (b) Demonstration of a fuel cell with a 25 μm CsH_2PO_4 electrolyte at 240 °C.[42]

seen in Figure 3.2(a). This makes a fuel cell or electrolyser with this electrolyte more complex. Luckily the dehydration process is highly reversible as Ikeda has demonstrated[51] and addition of water allows for regeneration of the lost conductivity. It has been determined that operation at 265 °C would require a water partial pressure of 0.22 atm to prevent the dehydration. Care must be taken during start-up of such a system as CsH_2PO_4 is water soluble. In the context of electrolysis the need for steam is of little concern at least on the anode as steam would have to be supplied anyway. This may however be less desirable for the cathode as the hydrogen would need to be dried after evolution which would introduce an additional step in the production.

Multiple full fuel cells have been reported in the literature with CsH_2PO_4 electrolytes. A schematic of one reported by Uda and Haile is shown in Figure 3.2(b) along with a power curve for the operation of said cell. Peak power density is reported to be 415 mW/cm^2 at $\approx$ 240 °C with humidified H_2 and O_2. The performance of this cell has yet to be beaten by other authors. Hallinder et al.[52] investigated CsH_2PO_4 as electrolyte in CO_2 reduction and co-electrolysis. While this endeavour was largely unsuccessful hydrogen evolution was observed showing for the first time a working electrolysis cell using CsH_2PO_4.[53]

3.2.2 Niobium phosphates

Amorphous niobium based phosphates show high surface acidity.[54] This trait has lead to their use in solid selective catalysis e.g. of 3,3-dimethyl-1-butene into 2,3-dimethyl-l- and -2-butenes.[55] Armaroli et al.[56] saw that prolonged treatment of Niobic acid ($Nb_2O_5 \cdot nH_2O$) with phosphoric acid create an amorphous material with a highly acidic surface and discrepancy in the coordination between surface and bulk. Weng and coworkers showed that it is possible to make particles with a crystalline backbone with much of the same properties.[57] Three different synthesis routes were used to create materials with the bulk consisting mainly of $Nb_2P_4O_{15}$, $NbOPO_4$ and $Nb_{1.91}P_{2.82}O_{12}$ respectively. They did show signs of amorphous residues and additional crystalline phases however, a trait seen by other authors as well.[58,59] Since amorphous niobium phosphate shows strong acidic traits the surface acidity of crystalline samples may be related to phosphoric acid retention on the surface and grain boundaries.

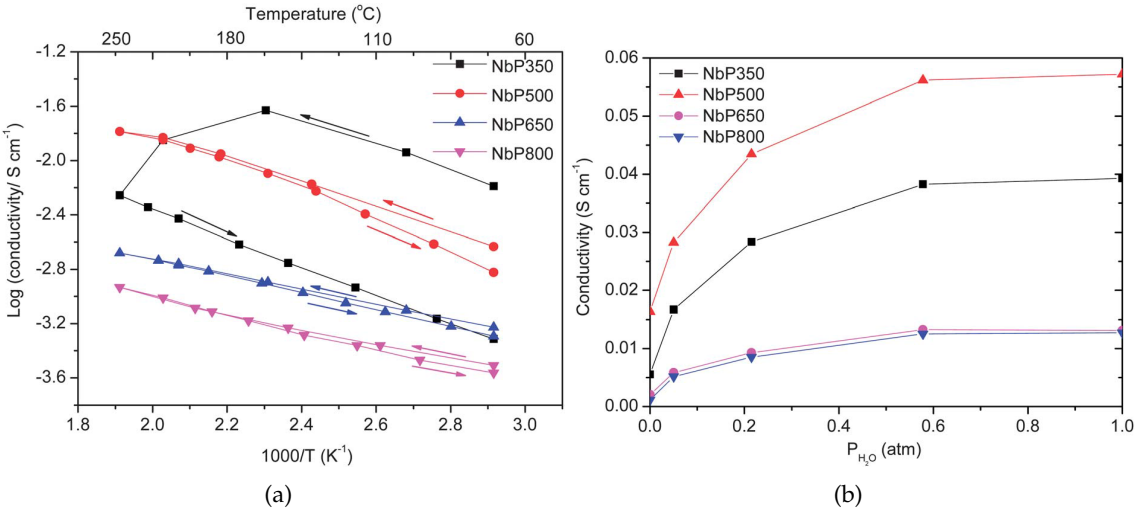

Figure 3.3: Conductivity of niobium phosphate in (a) dry air and (b) as a function of humidity at 250 °C.[60] Numbers in names denotes calcination temperature.

The high acidity seen for these compounds has lead to investigations into their possible use as electrolytes for electrochemical cells. Work done in our group by Huang et al.[60] have shown niobium phosphates to have conductivities as high as $1.6 \cdot 10^{-2}$ S·cm^{-1} in dry air (Figure 3.3). The conductivity is highly dependant on calcination temperature. Conductivity follows temperature with inverse proportionality. However, calcination at 350 °C gives a material that despite its high initial conductivity has poor stability. This has been interpreted as an incomplete crystallisation as well as too loosely bonded or too mobile phosphoric acid. The same interpretation may be given when looking at the effect of water content in the atmosphere. Here conducting species may be lost during heat-up for NbP350 giving a lower conductivity in general. Even though NbP500 shows some signs of loosing conductivity after thermal cycling it does have promising conductivity especially at high humidity making it of interest in electrolysis application.

3.2.3 Metal Pyrophosphates

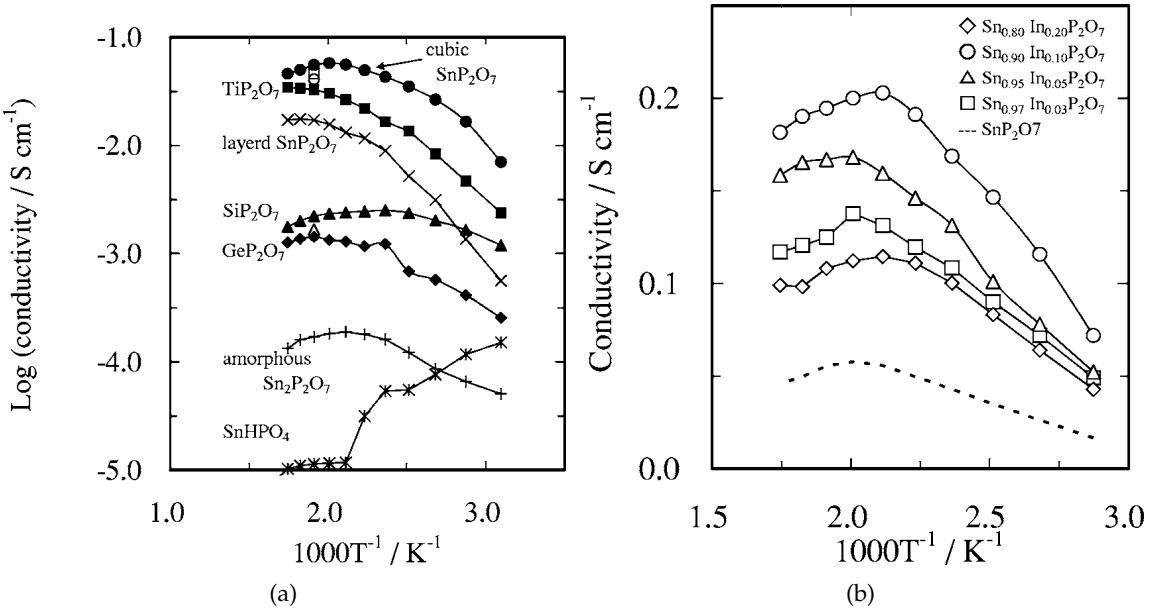

Figure 3.4: Conductivity of (a) MP_2O_7 samples (M= Ti, Sn, Si, Ge) and (b) $Sn_{1-x}In_xP_2O_7$ samples.[61] Both are under unhumidified conditions ($p_{H_2O} \approx 0.0075$ atm)

Within the last decade a new group of electrolytes has attracted attention in connection with IT operation. This is the metal pyrophosphates, MP_2O_7 (M=Sn, Ti, Zr, Si, Ge,...). This group of compounds got noticed when TiP_2O_7 was investigated as a support for ammonium polyphosphate based electrolytes and showed proton conductivity itself.[62] This conductivity was reported to be $2.4{\cdot}10^{-2}$ S·cm^{-1} at 250 °C in dry atmosphere and $6.6{\cdot}10^{-2}$ S·cm^{-1} at 200°C in wet atmosphere.[63] At the same time SnP_2O_7 was reported to show proton conductivity up to 1.0 S·cm^{-2} [64] above 80 °C in unhumidified air. A thorough investigation into the protonic conductivity was seen from Nagao and coworkers showing at 250 °C of $1.7{\cdot}10^{-3}$, $4.6{\cdot}10^{-2}$ and $4.7{\cdot}10^{-2}$ S·cm^{-1} for SiP_2O_7, TiP_2O_7 and SnP_2O_7 respectively.[61,65–67] These results are presented in Figure 3.4(a). The cubic form of SnP_2O_7 gave the highest conductivity results spurring a focus on this material and away from e.g. TiP_2O_7 for IT applications. For SnP_2O_7 other groups showed similar conductivities. Wang and coworkers as an example showed conductivities as high as $2.17{\cdot}10^{-2}$ S·cm^{-1} for this material at 448 K and in wet atmosphere.[68]
These materials were all made by mixing of an oxide precursor (e.g. SnO_2) with an excess of H_3PO_4 heated to 300 °C until a viscous paste was formed. They were heat treated at 650°C or in the case of Wang et al.[68] and Matsui et al.[62] 500 and 700°C respectively. The excess of phosphoric acid was seen to have a huge impact on the conductivity of the resulting compound. Nagao speculated that the reason for the lower conductivities reported by Matsui et al.[63] was a slight evaporation of phosphate species due to the slightly higher heat treatment temperature giving a $P_2O_7^{4-}$ deficiency which in turn affected the crystal structure.[61] This lead Nagao to the conclusion that the conductivity of SnP_2O_7 was a form of bulk conductivity as this is more affected by structural changes than surface

or grain boundary conductivity. In the case of Wang at al.[68] the SnP_2O_7 was made with a high initial excess of phosphorous (P/Sn = 2.8) in the form of phosphoric acid and heat treated at lower temperature than what was seen from other groups (500°C). This gave a material that performed well at low temperature, 175°C, with conductivities as high as $2.7{\cdot}10^{-2}$ S·cm^{-1}. Wang and coworkers attributed the performance of the material to an amorphous phase in the grain boundary. This was contrary to what was suggested by Nagao. This dispute will be detailed in Section 3.2.4.
In the work of Nagao and coworkers products of aliovalent doping of the pyrophosphates showed more promise than undoped materials and as will be seen in Section 3.2.4 these materials became the frontrunners of the pyrophosphate based IT electrolytes. As these doped pyrophosphates began to dominate the IT regime the focus of research for the undoped materials has shifted to higher temperatures. For SnP_2O7 alternative synthesis routes such as a chlorite precursor method[69] and a acetate precursor method[70] have lead to the study of high purity nano powder samples and they have shown bulk conductivities in the vicinity of $1.0{\cdot}10^{-7}$ S·cm^{-1} at 1000°C.[69] This is believed to be a combination of bulk and grain boundary conductivity. At these high temperatures TiP_2O_7 has proven to yield better results with values of conductivity ranging from $1.0{\cdot}10^{-5}$ S·cm^{-1} to $1.0{\cdot}10^{-3}$ S·cm^{-1} at 900 °C depending on the wetness of atmosphere.[71,72]

3.2.4 Aliovalent doped pyrophosphates

While looking at metal pyrophosphates Nagao et al. also investigated the aliovalent doping of these materials with cations such as In^{3+}, Sc^{3+}, Mg^{2+} and Al^{3+} and its influence on the protonic conductivity of said dopees. These materials exhibited a substantially higher conductivity than their undoped counterparts. An example of this can be seen in Figure 3.4(b) for In^{3+} doping.[61] Of this class of compounds $Sn_{0.9}In_{0.1}P_2O_7$ has shown the highest conductivity. Published conductivities are found to be as high as $2{\cdot}10^{-1}$ S·cm^{-1} [61,73,74] at 250°C in unhumidified air. These results all stem from the same group of authors using the same synthesis, namely the previously mentioned oxide precursor method. Authors using the alternative methods such as the chlorite or acetate precursor methods have not been able to reproduce such results in the IT range. Park using the acetate method did not provide conductivity results[70] but Tao reported a conductivity of $3.8{\cdot}10^{-8}$ S·cm^{-1} at 250°C.[69] Going up in temperature to 900°C the conductivity reached $8.0{\cdot}10^{-6}$ S·cm^{-1}.
For all materials made by the oxide route a conductivity maximum was seen at 200 - 220 °C. Chen and coworkers reported this maximum to be independent of water content in the atmosphere.[75] While the conductivity increased with water partial pressure the maximum did not move (Figure 3.5). This excludes the possibility that the loss of conductivity is due to escape of water from the electrolyte surface or bulk as the maximum should move towards lower temperature with lower water partial pressure. It was also seen that water partial pressure had a profound effect on the conductivity of the material. These two findings combined suggest a mode of conduction that does not in itself include water but can be enhanced by water.
Nagao and coworkers investigated the conductivity mechanism of their synthesised compounds by the H/D isotope effect. A lower activation energy (ΔE_a = 0.03 eV) was seen for D_2O than for H_2O containing atmospheres. This was interpreted as a result of dissociation

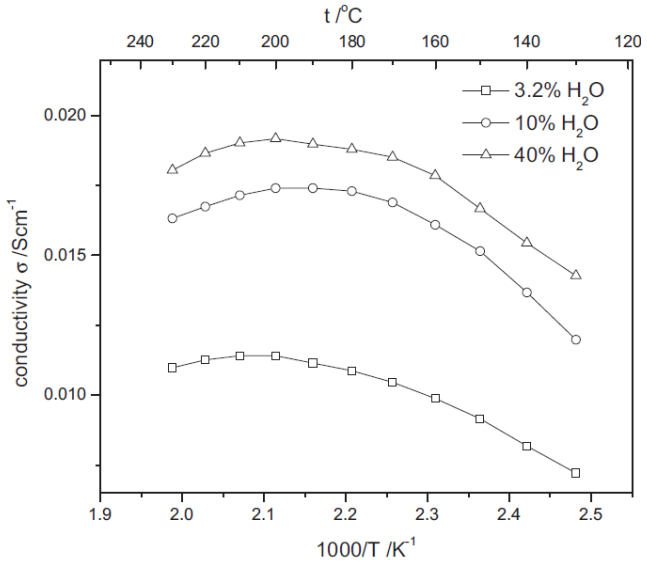

Figure 3.5: Conductivity of $Sn_{0.9}In_{0.1}P_2O_7$ in relation to atmosphere water content[75]

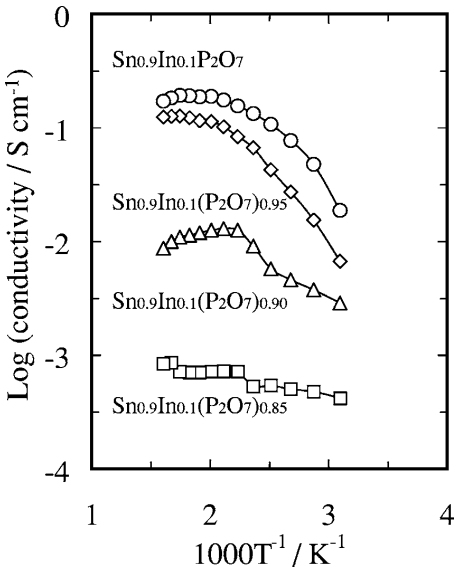

Figure 3.6: The relation between conductivity and deficiency of phosphorous[61]

of the O-H bound being the rate-determining step in the proton conduction. This lead to a Grotthuss mechanism interpretation. Based on their findings Nagao et al.[65] proposed a proton conductivity mechanism similar to that seen for high temperature perovskites with a similar method of proton incorporation (see Equation 3.1) for $Sn_{0.9}In_{0.1}P_2O_7$ and similar compounds. This choice of mechanism has been backed by Heo,[74] Sato[73] and Chen.[75] As an increase in conductivity is seen for addition of In^{3+} up to and including 10 mol % this may be a result of an ease of formation for oxygen vacancies driving the formation of interstitial protons.[76] Nagao observed a small change in the lattice parameter in XRD from 0 to 10 mol % doping correlating with the theory that the larger In^{3+} ion (r = 0.92 Å) creates vacancies when substituting for the smaller Sn^{4+} ion. Other studies have not seen this rise in lattice parameter until above 10 mol % doping[70] and then the effect has been much more pronounced.

The effect of water on conductivity seen in Figure 3.5 was explained as an effect of water incorporation into the structure via oxygen vacancies.[75]

Another tendency observed is the fact that phosphate deficiency substantially reduces the conductivity of a material.[65] When a deficiency of above 5 mol % is introduced the conductivity decreases by more than a factor of ten (Figure 3.6). At 15 % the conductivity is in the order of 10^{-4} S·cm^{-1}. It should be noted that this deficiency was introduced by withholding phosphoric acid in the first step of the oxide synthesis.

The bulk conductivity interpretation met some resistance. It was noted that higher firing temperature of the material severely reduces the conductivity.[69] This must be the result of a loss of some sort of conductive component as the structure of the material does not show signs of change. Furthermore Einsla at al.[77] discovered by neutron scattering a proton rich phosphate phase not detected by the most commonly used evaluation technique, X-ray powder diffraction (XRD) . This led them to speculate on the existence of a phosphorous rich amorphous phase present at the grain boundaries and it being respons-

ible for the protonic conductivity. This would be hidden from XRD due to its amorphous nature. This thought has been supported by the work of Kreller et al.[78] Here it was seen that increasing the phosphate to metal ratio did not result in any structural changes as seen in XRD but did have a drastic effect on the conductivity of $Sn_{0.9}In_{0.1}P_2O_7$. This may be caused by residual phosphoric acid or a similar phosphorous containing species. Xu and coworkers[79] showed that higher conductivity in SnP_2O_7 was related to a condensed P rich phase. This was detected by ^{31}P NMR as well as seen as a broad O-H bond in Fourier transform infrared spectroscopy (FT-IR). They concluded that the conductivity was not due to surface phosphoric acid which would be washed away easily but to an immobilised or polymerised phase sitting at grain boundaries and between particles. This notion was backed up by the work done by Harley et al.[80] where $LaPO_4$ was shown to owe its conductivity at 500 °C exactly to such an amorphous phase. Such an amorphous phase would be much harder to get rid of and still give rise to protonic conduction. While the work of Xu et al.[79] was done on SnP_2O_7 it is still believed to be valid for samples of $Sn_{0.9}In_{0.1}P_2O_7$ made by similar synthesis methods. This theory also explains why Chen and coworkers[75] did not see any loss of conductivity during washing of their samples. To remove the amorphous phase much more drastic methods are needed, such as prolonged boiling. This also explains the previously seen relation between deficiency of phosphorus and loss of conductivity as less of the amorphous phase would have been created during the synthesis when phosphoric acid was withheld.
While indium doped pyrophosphates are the most thoroughly described aliovalent doped pyrophosphates in literature they are not unique. As the acidity of $Sn_{0.9}In_{0.1}P_2O_7$ was conjectured to promote degradation in carbon electrodes[81] efforts were made to synthesise less acidic versions of this material. Genzaki and coworkers[82] showed results comparable to those of $Sn_{0.9}In_{0.1}P_2O_7$ for $Sn_{0.9}Mg_{0.1}P_2O_7$ and $Sn_{0.95}Al_{0.05}P_2O_7$. The conductivities reported were as high as $8.3{\cdot}10^{-2}$ and $7.5{\cdot}10^{-2}$ $S{\cdot}cm^{-1}$ respectively at 300 °C. These results are in good agreement with the study of Tomita[83] on Al^{3+} doping of tin pyrophosphate. Here conductivities above $1.0{\cdot}10^{-1}$ was seen with the best performing doping level begin 5 mol % Al^{3+}. Another interesting material is $Fe_{0.4}Ta_{0.5}P_2O_7$. This was reported in a study by Shen and coworkers looking at the conductivity of material with the general formula $A^{III}_{0.5}B^{V}_{0.5}P_2O_7$. It was seen that introducing a bulk deficiency into the material improved the conductivity.[84] $Fe_{0.4}Ta_{0.5}P_2O_7$ gave the best results with $2.7{\cdot}10^{-1}$ at 300 °C. It should be noted that these materials were calcined at the very low temperature of 450 °C. Even though this material seems promising it has yet to be investigated by other groups.

3.2.5 Applications of doped pyrophosphates

Most groups working with the conductivity aspect of metal pyrophosphates and their doped forms do so from a fuel cell point of view. This means that most electrochemical application tests seen in the literature are of full fuel cells. Quite a variety can be found in the literature with varying electrolyte thickness, catalyst loadings and conditions. The first fuel cell seen was from Nagao et al.[65,74] The electrolyte was a pressed pellet of $Sn_{0.9}In_{0.1}P_2O_7$ with a thickness 350 μm and Pt/C cathodes with a Pt loading of 0.6 mg/cm^2 (see Figure 3.7). This cell was tested at 250 °C with dry O_2 and H_2 and reached a maximum power density value of 264 mW/cm^2. The cell showed a great tolerance for CO with no loss of performance with up to 10 % CO in the fuel. Attempts of improving upon

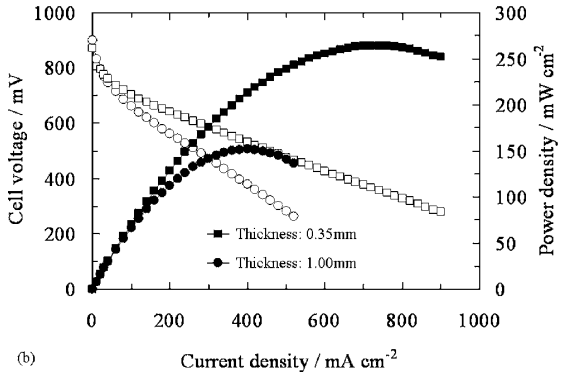

Figure 3.7: Fuel cell with $Sn_{0.9}In_{0.1}P_2O_7$ electrolyte at 250 °C in dry H_2 and O_2 [74]

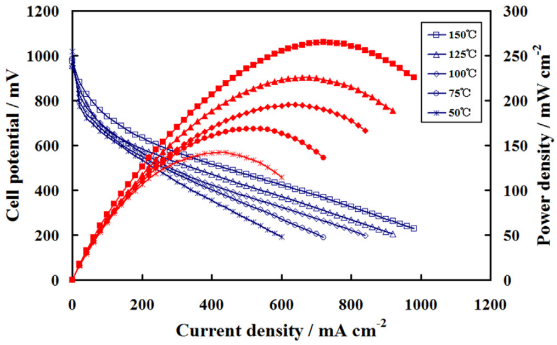

Figure 3.8: Performance of a sSEBS-$Fe_{0.4}Ta_{0.5}P_2O_7$ composite fuel cell under unhumidified conditions [85]

these results have centred around methods of creating thin layers of pyrophosphates. As sintering is made impossible by phosphate evaporation creation of composites have been in focus. To date most successful result is again by Heo et al. [85,86] and can be seen in Figure 3.8. With the addition of sulfonated polystyrene-*b*-poly(ethylene/butylenes)-*b*-polystyrene (sSEBS) to $Fe_{0.4}Ta_{0.5}P_2O_7$ they were able to create functional membranes of thicknesses down to 50 μm without any greater loss of performance and reaching a peak power density of 265 mW/cm^2 at 150 °C. Unfortunately no stability data for these full cells are published. This would be of great interest as recent results for TiP_2O_7 indicates that long term stability may be an issue. [87]

Apart from fuel cell applications Nagao also demonstrated an electrochemical cell for NO_x reduction using $Sn_{0.9}In_{0.1}P_2O_7$ with the intention of use as sensors or selective catalytic reduction (SCR) of NO_x in diesel exhaust. [66,67] As the preferred operation temperature for $Sn_{0.9}In_{0.1}P_2O_7$ is close to the exhaust temperature of diesel engines (200-350 °) integration would be somewhat easy. The principle was demonstrated using Pt and Pt-Rh electrocatalysts. [88]

Lastely, Hibino has reported identifying hydroxide ion conductivity in antimony doped tin pyrophosphate ($Sn_{0.92}Sb_{0.08}P_2O_7$). [89] Conductivity is reported to be as high as $1.0{\cdot}10^{-2}$ S·cm^{-1}. With this material a possible alkaline fuel cell has been demonstrated with a 100 μm membrane stabilised by PTFE yielding a maximum power density of 147 mW/cm^{-2} at 200 °C. [90] The same type of membrane has also been used to demonstrate a rechargeable air battery. [91]

3.3 Electrocatalysts

The benchmark electrocatalysts in PEM electrolysis are platinum for the hydrogen evolution reaction (HER) and iridium oxide for the oxygen evolution reaction (OER). As this work can be seen as an evolution of the PEM electrolyser tradition these benchmarks have been inherited. This section will give a short presentation of these two benchmarks as well as some interesting alternatives. First the oxygen evolution electrocatalysts will be discussed and then the hydrogen evolution electrocatalysts.

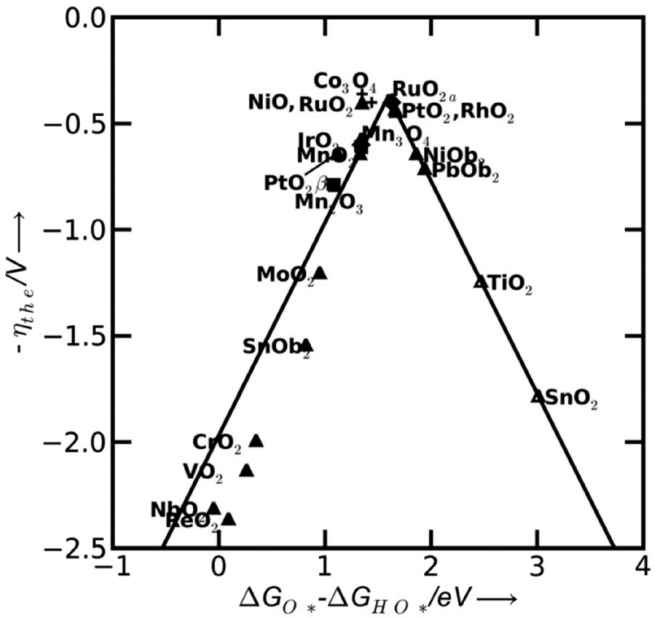

Figure 3.9: The activity towards oxygen evolution of oxides. Overpotential is represented as a function of difference in Gibbs' free of subsequent intermediates in the oxygen evolution reaction[92]

3.3.1 Anode electrocatalysts

As mentioned in Section 2.2.2 the slow kinetics of the OER is responsible for the largest contribution to the overpotential of an electrolyser cell. It is therefore of utmost importance that the anode electrocatalyst intrinsically adds as little as possible to the overpotential of the process. It must be able to bind the species involved in the reaction to its surface strongly enough for reaction to occur but not so strong that reaction sites become unavailable. In acidic environment binary oxides of transition metals are most commonly used. RuO_2 and IrO_2[93] are the most prominent of these. The difference in energy states of two subsequent intermediates in the OER reaction has been seen to be an indicator of catalytic activity. This is illustrated in a so called volcano-plot in Figure 3.9 where IrO_2 and RuO_2 are seen to give rise to a low overpotential as neither of the two intermediates limits the OER reaction. While RuO_2 has the lowest overpotential it is unstable. As part of the OER mechanism RuO_2 is oxidised to RuO_4 which, depending on the operation temperature of the electrolysis, is a liquid or a gas and can dissolve or evaporate.[94] Thus pure RuO_2 has poor stability and IrO_2 which has higher stability has long been the preferred electrocatalyst. It has been used extensively in PEM electrolysis.[29,95,96] Combination of RuO_2 and IrO_2 ($Ir_xRu_{1-x}O_2$) to stabilise the former and improve the performance of the latter have been seen regularly in the literature as well.[96–98] Marshall et al.[96] reported a cell voltage of 1.567 V at 1A/cm^2 for $Ir_{0.6}Ru_{0.4}O_2$ with a Nafion 115 membrane, an improvement of 125 mV compared to IrO_2. Addition of further elements have also been seen. Cheng[99] reported a reduction of 40 mV at 1 A/cm^2 with the addition of Mo to $Ir_{0.4}Ru_{0.6}O_2$ ($Ir_{0.4}Ru_{0.6}Mo_xO_y$). These are just to name a handful of the numerous studies of transition metal oxides.

Attempts to reduce the amount of IrO_2 due to costs have also been seen. Examples of this includes the stabilisation of IrO_2 on TaC.[100,101] As an example Polonsky and coworkers[101] saw a 36% performance increase with the addition of 30 wt.% TaC to IrO_2. This was explained as due to a lowering of the contact resistance and reduced penetration of electrocatalyst into the GDL during spraying.
While a host of variations have been seen over the binary and mixed transition metal oxides no non-noble metal alternatives for acidic media have to this authors knowledge been reported in a peer reviewed journal.
For low acidity electrolytes some possibilities may exist. Nickel is widely used in alkaline water electrolysis where a surface layer of NiOOH is created on the metal during operation. This surface oxide layer is believed to be the active species in the OER on nickel in alkaline media.[93] Kjartansdóttir et al.[102] showed in a Pourbaix diagram that this oxide layer exists into the lightly acidic region, e.g. pH = 6, at voltages above 1.5 V. At the same time Ni has been seen to have a remarkable stability in KH_2PO_4 at 260 °C.[103] This indicates a possible use with electrolytes such as CsH_2PO_4 and $Sn_{0.9}In_{0.1}P_2O_7$ if their surface acidity is found to be on the scale of molten KH_2PO_4. This is however dependant on a handful of factors including how the acidic media influences the mechanism of the OER.
A second possibility would be mixed oxides such as perovskites and spinels. These material classes includes electrocatalyst previously investigated as OER electrocatalysts in the framework of alkaline electrolysis. This is materials such as $LaNiO_3$,[104] $Ba_{0.5}Sr_{0.5}Co_{0.8}Fe_{0.2}O_{3-\delta}$ (BSCF)[105] and $NiCo_2O_4$.[24] A lower acidity of the electrolyte could allow for their use without corrosion. $LaNiO_3$ have shown high electric conductivity[106] and could be an interesting material for an initial test.

3.3.2 Cathode electrocatalysts

The most commonly used cathode electrocatalyst in PEM water electrolysis is platinum, either as Pt-black or as Pt supported on carbon. Supporting platinum nano-particles on high surface area carbon stabilises the platinum in regards to particle sintering, gives a high active surface area and ensures a good electric conductivity. While loadings of platinum are fairly low, in the range of 1 - 0.5 mg/cm^2,[17] further reduction or complete substitution is still a goal due to the high cost of platinum and the fact that 86 % of the worlds platinum production is controlled by only two nations, Russia and South Africa.[107] Ways of reducing the Pt contents in the cathode include core-shell electrocatalyst such as Pt @ Cu,[108] the production of platinum carbon nano-tubes[109] and Pt Bulk metallic glass nanowires.[110]
Contrary to the OER a range of alternative non-noble metal electrocatalysts have been proposed for the HER such as MoS_2[111] and boron-capped trix(glyoximato) cobalt complexes.[112]
In the context of phosphate based electrolytes two materials, namely Ni and WC, have recently been seen to give good results for HER. Papandrew and coworkers[113] demonstrated the use of unsupported Ni nano particles for the HER with CsH_2PO_4 as electrolyte at 250°C. By sequential uniaxial pressing at 125 MPa membrane electrode assemblies with 60 μm electrolytes were formed. The Ni electrode had a loading of 3.5 mg/cm^2 and the Pt/C electrode had a Pt loading of 1.05 mg/cm^2. Testing at -0.2 V with humidified hydrogen on both electrodes (0.3 bar water partial pressure) gave a

stable reduction current of 207 mA/cm^2. Measuring under identical conditions with two Pt/C electrodes gave a current density of 558 mA/cm^2. Measuring at steady-state (-0.2 V) showed a stable result over 100 hours.
Secondly tungsten carbide (WC) has been known to be active for the HER since the 70's.[114] Recent studies of its activity with elevated temperature[115,116] have shown increasing activity in phosphoric acid at all measured temperatures from 22 °C to 186 °C. As WC is a refractory ceramic it would be expected to be functional at temperatures where Pt is unusable and increase in activity well into the intermediate temperature range. This makes it an ideal candidate for an alternative HER electrocatalyst in IT electrolysis.

3.4 Conclusions based on the literature

The investigation of the literature lead to a focusing of the scope of the work. It was decided to attempt to create functioning electrolyser cells with $Sn_{0.9}In_{0.1}P_2O_7$, CsH_2PO_4 and niobium and bismuth containing compounds as electrolytes. It was also decided to investigate Mg^{2+} and Al^{3+} doped pyrophosphates in the hopes of these replacing the expensive indium doped material. Pt and IrO_2 electrocatalysts were chosen as benchmarks for cathode and anode electrocatalysts respectively due to their ubiquity in PEM water electrolysis. The alternative electrocatalysts chosen for investigation were WC, Ni and $LaNiO_3$. WC and Ni were to be tested as cathode electrocatalyst where it was the hope that they would prove to be highly active and highly stable. Further it was the hope that a raising of the temperature would give improved performances. Ni was also to be tested as anode electrocatalyst to see if the acidity of the environment was low enough to keep it from dissolving and instead forming an active oxide layer. $LaNiO_3$ would also be tested as anode electrocatalyst to get an idea of the feasibility of the use of mixed oxides in this regard.

PART III

EXPERIMENTAL ASPECTS

CHAPTER 4

Experimental techniques

This chapter will present the techniques used to evaluate experiments. This includes physicochemical techniques and electrochemical methods. The electrochemical methods will be described in detail and the theoretical background will be given when appropriate. The workings of the physicochemical techniques will be considered common knowledge.

4.1 Physicochemical techniques

4.1.1 X-ray powder diffraction

X-ray powder diffraction (XRD) was used for phase determination. This was done using a Huber D670 diffractometer equipped with a CuKα radiation source (λ = 1.54056). The range was 3° to 100° in steps of 0.02° in 2θ. For determination of average crystallite size for a chosen crystal plane the Sherrer equation was used:

$$\mathrm{T} = \frac{\mathrm{C}\lambda}{\mathrm{B}\cos\theta} \tag{4.1}$$

Where T is the average crystallite thickness as measured through the given plane, C is the shape factor and B is the peak width at half maximum. C was assumed to be 0.9 independent of shape making the calculated values valid only as a means of size comparison amongst similar samples and not as actual thicknesses to be compared with arbitrary materials.

4.1.2 Scanning Electron Microscopy and Energy Dispersed Spectroscopy

Scanning electron microscopy (SEM) was done on a Zeiss Evo MA 10 scanning electron microscope. Energy Dispersed Spectroscopy (EDS) was done with a Oxford EDX X-max 80mm^2 detectror.

4.1.3 Fourier transform infrared spectroscopy

FT-IR was done using a PerkinElmer Spectrum Two with a UATR single reflection diamond. Spectra were recorded and treated using PerkinElmer Spectrum version 10.03.07.

4.1.4 ^{31}P Nuclear Magnetic Resonance

All ^{31}P Nuclear magnetic resonance (NMR) measurements were done at Institute of Chemical Engineering, Biotechnology and Environmental Technology, University of

Southern Denmark (SDU).
^{31}P NMR measurements were done on a Varian INOVA spectrometer using a 3.2 HX magic-angle spinning (MAS) NMR probe tuned to ^{1}H and ^{31}P. Measurements were performed at 11.7T corresponding to 202.3 MHz for ^{31}P. The spectra were referenced relative to 85% H_3PO_4 ($\delta(^{31}P)$ = 0 ppm) and tetramethylsilane using a secondary reference of H_2O ($\delta(^{1}H)$ = 4.6 ppm). The ^{31}P MAS NMR spectra were recorded using 12 kHz spinning and a relaxation delay of 400 s with ^{1}H decoupling. The ^{31}P NMR spectra were analysed using the program SpinWorks.

4.2 Electrochemistry

4.2.1 Polarisation

As polarisation curves are an expression for losses in the cell as current is raised they can yield important information about the performance of a cell. For an electrolyser lower is better and a simple comparison of voltage at a given current density, or vice versa, between cells can often give a good indication of which cell performs the best. This is however rather qualitative and says nothing about the performance of the individual components of the cell.
As discussed in Section 2.2.1 a variety of processes add to the overpotential of an electrolyser cell when current is applied. Estimations of the contributions from electrodes and ohmic processes can be separated to better evaluate polarisation data. Rewriting Equation 2.7 and Equation 2.11 shows how:[117]

$$\begin{aligned} E_{cell} &= E_{rev} + \eta_{an} + \eta_{cat} + I \cdot R_{ohm} \\ &= (A + b \cdot \log(I)) + (I \cdot R) \end{aligned} \tag{4.2}$$

Fitting Equation 4.2 to a polarisation curve allows for determination of parameters A, b and R. A includes the reversible cell voltage and the Tafel equation constant (Equation 2.9 in Section 2.2.2), b is the pre-log factor from the Tafel equation and R is the ohmic resistance (R_{ohm}) of the cell. This makes it possible to quantify the contribution of activation and ohmic losses to changes in polarisation curves.

4.2.2 Platinum reference electrode

Polarisation curve fitting does not allow for a splitting of activation over voltage into an anode contribution and a cathode contribution. If this is desired a reference electrode can be introduced. Reference electrodes allows for measurements of potential differences between an electrode of known potential (the reference) and an unknown electrode. This allows for determination of the overpotential contributions of the electrodes in a cell. A very commonly used reference is the Pt/H_2 reference electrode. Such a reference was used in this work to determine the anode and cathode contributions in electrolyser cells.
The reference measurements in this work were done with the platinum wire placed on the cathode side of the electrolyte with a distance from the cathode of at least 3 times the thickness of the electrolyte. Such a placement has in literature[118] been shown to measure the same potential as an electrode placed halfway between the cathode and the anode.

This means that the measured potential will need to be corrected by $\frac{1}{2}$ the electrolyte resistance if a single electrode potential is to be obtained.

4.2.3 Impedance

To supplement polarisation curve evaluation electrical impedance spectroscopy (EIS) was employed. This allowed for determination of electrolyte resistance which in turn could be compared to the estimated ohmic resistance from polarisation. It also allowed for evaluation of electrode degradation over time or temperature.
Impedance can be seen as an extension of the concept of resistance. Where resistance is a circuit elements ability to withstand the flow of direct electrical current impedance is said elements ability to withstand alternating current. Impedance, contrary to resistance, have a phase. This means that apart from the change of a signals magnitude, as per Ohms' law seen for direct current, a change of phase may also be observed. Impedance is also dependant of a signals frequency. The response of an ideal resistor is independent of frequency. This is however not the case for different circuit elements such as inductors or capacitors. This means that by sending a current or voltage signal and varying the frequency, observation of shifts in phase and magnitude can give detailed information about a system.
For a sinusoidal voltage signal, $\mathrm{E} = \mathrm{E}_0 \sin(\omega \mathrm{t})$, the current response is $\mathrm{I} = \mathrm{I}_0 \sin(\omega \mathrm{t} + \phi)$. Impedance is then defined as:

$$\mathrm{Z}(\omega) = \frac{\mathrm{E}(\omega)}{\mathrm{I}(\omega)} = \frac{\mathrm{E}_0 \sin(\omega \mathrm{t})}{\mathrm{I}_0 \sin(\omega \mathrm{t} + \phi)} = \mathrm{Z}_0 \frac{\sin(\omega \mathrm{t})}{\sin(\omega \mathrm{t} + \phi)} \tag{4.3}$$

where E_0 is the amplitude of the voltage, I_0 is the amplitude of the current, Z_0 is the impedance magnitude, ω is the radial frequency and ϕ is the phase shift. All these parameters are functions of frequency. This relation can be rewritten to a complex form:

$$\mathrm{Z}(\omega) = \frac{\mathrm{E}_0 \mathrm{e}^{(\mathrm{i}\omega \mathrm{t})}}{\mathrm{I}_0 \mathrm{e}^{(\mathrm{i}\omega \mathrm{t} - \phi)}} = \mathrm{Z}_0(\cos(\phi) + \mathrm{i} \sin(\phi)) \tag{4.4}$$

where $\mathrm{i} = \sqrt{-1}$. This representation has the advantage that it lets the impedance be split up into a real and an imaginary contribution, both functions of frequency. These contributions are $\mathrm{Z}_{\mathrm{re}} = |\mathrm{Z}| \cos(\phi)$ and $\mathrm{Z}_{\mathrm{im}} = |\mathrm{Z}| \sin(\phi)$ respectively. This allows for ease of representation via the so called Nyquist-plot. Here the real part of the impedance is plotted along the x-axis and the imaginary part along the y-axis. Moving towards higher values on the x-axis corresponds to lower frequency. Any point on the impedance curve can be represented by an impedance vector from the origin. This is illustrated in Figure 4.1. Note that the y-axis is negative.

Processes or circuits will in general show up as semicircles or depressed simicircles in Nyquist plots. These are in general a characteristic of a time constant of a specific phenomenon but may hide more than one phenomena. This will be treated in more depth in Sections 4.2.5 and 4.2.6 .
Of note here is the fact that when the phase shift is zero ($\phi = 0$) then $\mathrm{Z} = \mathrm{Z}_{\mathrm{re}}$ as the imaginary part of the impedance is 0. This is the special case of the ideal resistor and $\mathrm{R} = |\mathrm{Z}| = \mathrm{Z}_{\mathrm{re}}$. It means that at frequencies where a system behaves as an ideal resistor the resistance of the system can be read of the real axis. For an electrochemical cell this is the ohmic resistance of the electrolyte. The impedance where the signal has an imaginary component

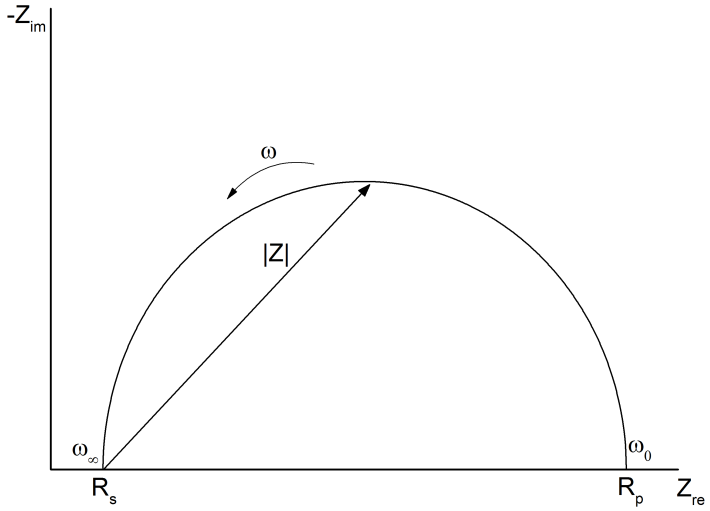

Figure 4.1: An example of a Nyquistplot. The pure resistance is read as the left most intercept with the x-axis. The right most intercept gives the polarisation resistance.

is termed the polarisation impedance. The distance measured along the real axis from the beginning to the end of the polarisation impedance is called the polarisation resistance, R_{pol}.
The measurement of impedance can be done by sending a signal of a fixed amplitude into the system and varying the frequency of said signal. Different processes or elements will show different responses depending on frequency and covering as broad a range of frequency as possible is desirable to get a complete picture. There is a trade off as low frequency means long time for data collection. Frequency is usually varied over 6-8 decades and 10 points of data recorded each decade. In this work spectra will be recorded from 10^5 Hz to 10^{-1} Hz.
An important factor is that an impedance response is only really meaningful if the region it is recorded in is approximately linear. Otherwise the assumption of a sinusoidal response from a sinusoidal signal will break down. To ensure this the amplitude of the signal used must be chosen with care. Again there is a trade off however. If the amplitude is too little the signal to noise ratio will be too small and the recorded data will be of poor quality. It is conventional wisdom to use signals around 10 mV. In this work higher amplitudes have been used due to signal to noise concerns.

4.2.4 Kramers-Kronig Analysis

When using impedance data it is important to validate it as many things may influence and possibly corrupt the data. One possible, and popular, way of assessing the quality of impedance data is by using the Kramers-Kronig (KK) transformations. The general

principle of these transformations are based on causality of impedance data. If the data is of good quality then the imaginary part of the impedance over a full frequency range can be determined from the real part of the impedance with the exception of a possible stray inductance. Likewise the real part of the impedance can be determined from the imaginary impedance with the exception of possible zero or infinity frequency resistances. A more detailed treatment of the mathematics behind this concept can be found in Appendix A.1. These mathematical concepts has the result that by doing transformations on the real and imaginary part of impedance data respectively and comparing them to the measurements the quality of the data may be gauged. Poor quality data will show deviations between measurements and calculations. When looking at residual plots it is generally safe to use data with no more that 1 % deviations.
For a data set to be considered "of good quality" by the KK transformation it must fulfil the following conditions[119,120]

- Causality The measured signal may not depend on anything but the applied signal. No response may be present before the signal is applied. This may break down due to stray inductances, systemic interferences and the like.
- Linearity As mentioned before there must be a linear relation between the applied signal and the received. This may break down if too big a amplitude is used.
- Stability The system may not change during the duration of the entire measurement. If the system is not in equilibrium or the signal induces change this may break down.
- Finiteness A finite response must be received for all frequencies. It includes $\omega \rightarrow 0$ and $\omega \rightarrow \infty$.

This last induces some problems as it requires responses for an impossible large range of frequencies. If highest and lowest frequencies measurements give $Z_{im} = 0$ and $Z_{re} = a$ constant this may be disregarded. If not, an extrapolation of the data is needed. This is also treated in Appendix A.1. It is quite common to get signals due to inductances in the system e.g. at high frequencies. If the rest of the conditions are met KK transformations can be used to correct the impedance data for inductance.
In this work KK validation was done using the program written by Boukamp in 1999.[121] Data with a residual distribution within ± 1 % was considered good data. In some special cases higher percentages were allowed if the rest of the data was of good quality, no patterns were seen in the residuals and the offending part of the data was not used for any interpretation.

4.2.5 Distribution of relaxation times

Another way of evaluating impedance data is looking at the distribution of relaxation times (DRT). DRT is a very useful tool for evaluating systems that are not yet well understood and where a precise equivalent circuit model is not yet available. It can even be used to separate overlapping polarisation processes and requires no prior knowledge of the processes of the system.[122] This gives it a great advantage over e.g. Nyquist representation where semicircles may hide more than one element.
The different polarisation processes in a cell have different time constants (relaxation times). These processes contribute to the total impedance with a fraction of the polarisation impedance at each frequency. It is in theory possible to distinguish different

processes by observing at which characteristic frequencies there is a spike in impedance contribution. This requires a link between the distribution of relaxation times and polarisation impedance observed. This was determined in 1941 by Kirkwood and Fuoss[123] with their convolution equation:

$$Z_{pol}(\omega) = R_{pol} \int_0^\infty \frac{\gamma(\tau)}{1 + i\omega\tau} d\tau, \qquad \int_0^\infty \gamma(\tau) d\tau = 1 \tag{4.5}$$

where $\gamma(\tau)$ is the distribution function, R_{pol} is the polarisation resistance and Z_{pol} is the impedance. It can be seen as a measure of how large a fraction of polarisation resistance is contributed at a given relaxation time. We would like to isolate $\gamma(\tau)$ but this is problematic. The relation requires measurements over the entirety of the impedance spectrum which is not physically possible. This makes it impossible to solve analytically. Even numerically it is problematic as even large samples of data are susceptible to amplification of experimental errors.
These problems can be overcome however if the data obtained is of good quality. Then it may be extrapolated to practically zero and infinite frequency by KK transformation. This gives the possibility of estimating the ohmic resistance (R_s) and the total resistance (R_{tot}). By extension the polarisation resistance (R_p) can be estimated as well as it is equal to R_{tot} - R_s. The extrapolated data can then be Fourier transformed, filtered for amplified experimental errors and by inverse Fourier transformation the distribution of relaxation times can be obtained.[124,125] This deconvoluted function can then be plotted as a function of frequency ($f = 2\pi/\tau$) and the fractions of polarisation can be seen. Discerning peaks at specific frequencies can give an idea of the number of elements in a system. Elements with more than one relaxation time, such as electrode processes, gives a broader distribution than ideal processes. This may cause overlap of relaxation peaks. However a further benefit of this method is that changing reaction parameters such as temperature, gas flow, gas composition and purity of feed can reveal which peaks belong to which kinds of processes and help to further deconvolute the spectrum. Raising temperature, say, would result in an activation of kinetic processes and a shrinking of peaks related to these processes. A comparison of DRT at different temperatures would make this immediately apparent. Thus mapping of processes to frequencies is possible if enough parameters are changed. This can be used to get an idea of how approach fitting of the impedance spectra. Theoretically it is possible to determine resistances related to each process by integration of each peak. However it is not advisable as the fitting is still an approximation. DRT should only be used as a way of evaluating qualitative trends.
In this work DRT was done using the software toolkit RavDav developed at DTU Energy Conversion by Chris Graves.[126]
The concepts detailed here are elaborated in Appendix A.2.

4.2.6 Complex non-linear least-squares fitting

Certain phenomena give rise to a specific kind of impedance response. In the case of electrochemical cells two very commonly seen responses are the capacitor and resistor placed in parallel (RC), and a so-called constant phase element (CPE) and a resistor placed in parallel (RQ). The CPE replaces the ideal capacitor in the case of a phenomenon which does not have a single time constant but a distribution of time constants. The most commonly seen example of this is electrode processes where surface roughness and other

inhomogeneities result in such a distribution. The impedance of the RC and RQ responses can be expressed as:

$$Z_{RC} = \frac{R}{1 + i\omega RC} \qquad Z_{RQ} = \frac{R}{1 + (i\omega)^n RQ} \tag{4.6}$$

where R is a resistance, C is a capacitance, Q is the constant phase proportionality factor and n is the constant phase exponent with values between 0 and 1. Where a RC element is seen in a Nyquist plot as a semi-circle the RQ element is seen as a depressed semi-circle and n can be seen as a value of this depression. It is very important to note that contrary to R and C, Q has no direct physical counter part and is a mathematical tool in the investigation of heterogeneous processes.
These above mentioned elements can be fitted to recorded impedance data by complex non-linear least-squares (CNLS) fitting. If the system investigated is sufficiently well known, e.g. by prior investigation by DRT or similar, a selection of elements may be ascribed to the two different processes in the system.
In this work this approach was used to quantify the resistance contributions from different parts of the system. Fitting was done using the program ZView. A simple equivalent circuit model consisting of R-RQ-RQ was used (Figure 4.2). This model was seen to be in good agreement with not only the data fitted (χ^2 less than 10^{-4} for all fits) but also what was observed in DRT.

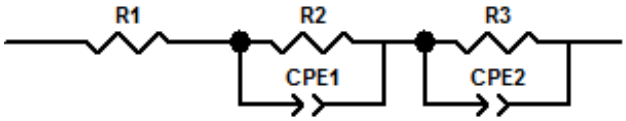

Figure 4.2: The equivalent circuit used for fitting electrolyser cell impedance in this work. A simple R-RQ-RQ circuit was used.

4.2.7 Conductivity

In this work impedance spectroscopy was also used for determination of protonic conductivity (σ) of electrolyte samples. For samples of high conductivity the electrolyte resistance can be determined from the ohmic resistance seen in the impedance spectrum.[46] This method was used for determination of conductivity in this work.

PART IV

EXPERIMENTAL WORK

CHAPTER 5

Fabrication of components

This chapter deals with the fabrication of components used and tested in electrolysis. This includes the synthesis of electrolytes and pressing of these into testable pellets, synthesis or fabrication of electrocatalysts and GDLs and their assembly into functional electrodes. Some thoughts and results on optimisation of these components for electrolysis operation will be part of this chapter as well. This will be in anticipation of the next chapter where the construction and operation of the electrolysis setup will be discussed thus describing the use of the components presented here.
A note on the phraseology used: Here and in the following chapters an assembly of a GDL and an electrocatalyst will be called an electrode. Similarly an assembly of two electrodes, an anode and a cathode, and an electrolyte will be denoted as a cell or an electrolyser cell. When referring to the components into which the electrolyser cell is placed when electrolysis was attempted, the flow plates and end plates, the phrase cell housing will be used. The cell housing and the additional components needed for electrolysis (e.g. evaporators, temperature controller, condensation unit) will be termed the setup. While this phraseology may not entirely line up with other authors conventions this was found to be the least confusing by this author. Hopefully this will eliminate confusion on what the usually rather loosely defined term "cell" actually refers to in this work.

5.1 Synthesis of proton conductors and catalysts

5.1.1 Iridium oxide

The iridium oxide used as anode electrocatalyst was synthesised by a modified Adams fusion synthesis method. The Adams fusion method, first published by Adams and Voorhees[127] in 1922, is a still widely used technique for creating high yield, high purity PtO_2, from a chloride precursor. While PtO_2 is in itself not an active catalyst it is easy to handle and can be reduced in situ to platinum black and thus making it catalytically active. The synthesis has since been modified in various ways to create other metal oxides such as RuO_2, IrO_2 as well as mixed oxides.[99,128]
The technique relies on an ion exchange of Cl^- by NO_3^-, by mixing the chloride precursor with a NO_3^- source in a solvent. This can be done in a range of polar solvents, and originally water was used. Today it is common to use isopropanol. The ion exchanged metal nitrate and by-products are subsequently heat treated to eliminate NO_2 and oxygen:[128]

$$H_2IrCl_6 + 6NaNO_3 \rightarrow NaCl + Ir(NO_3)_4 + 2HNO_3 \quad (5.1)$$

$$Ir(NO_3)_4 \xrightarrow{\Delta} IrO_2 + 4NO_2 + O_2 \quad (5.2)$$

The synthesis is carried out in a furnace due to heat requirements as well as NO_2 and NO evolution. Gas evolution begins around 350 °C,[129] and to ensure full reaction heating to 500 °C is usually employed.[128,130]
The synthesis was in this case done as follows: Dihydrogen hexachloroiridate(IV)hydrate (Alfa Aesar 99% metal base), 3214,87 mg, was weighed in a glove box under argon. The inert atmosphere was a necessity to keep a fixed hydration level and by extension a true measure of the amount of iridium weighed. The $H_2IrCl_6{\cdot}4H_2O$ was brought to complete dissolution in 75 mL isopropanol (Sigma-Aldrich, puriss). After complete dissolution, generally after 3-4 hours under stirring, finely mortared sodium nitrate was added at a molar excess of 100 times the amount of iridium, in this case 56.85 g. The addition was done a little at the time under stirring and when all the $NaNO_3$ was added the mixture was heated to 70 °C still under stirring and evaporated to dryness (6-8 hours). The resulting mixture was mortared, placed in a crucible and moved to a furnace which had been preheated to 500 °C. After heat treatment in 5 hours the furnace was allowed to cool freely. The reaction product was removed from the crucible, a process often requiring hammer and chisel, ground and then washed by centrifugation in demineralised water until addition of silver nitrate to the washing water showed no signs of residual chloride ions. Up to 6 washes were needed for such a large batch. After drying the catalyst was ready. Nominally the yield should be 1.500 g IrO_2 and in reality the yield was in the range of 96-99 %.
Investigation by XRD showed a single crystalline phase compound. Using the Scherrer equation the average crystallite size for the (110) plane was calculated to be 8.3 nm. SEM showed individual particles in the range of a few hundred micron in loose agglomerates. BET revealed a specific surface area of 121 m^2/g.

5.1.2 Tungsten carbide

The following synthesis work was graciously done by PhD Simon Meyer from the Inorganic Chemistry group at the Technical University of Munich, Germany.
Tungsten carbide (WC) samples from two different precursors where synthesised for testing. These precursors were mesoporous WO_3 and W_2N denoted mWO_3 and mW_2N respectively. mWO_3 was made by impregnation of a mesoporous silica template (KIT-6) with ammonium metatungstate. After calcination mesoporous tungsten trioxide was obtained. Further ammonolysis of mWO_3 gave the mW_2N precursor. These precursors where then treated with HF and water 3 times by centrifugation to remove the silica template. They were then carburised in a gas steam of 25% CH_4 in H_2. The resulting tungsten carbide powders were named mWO_3 and mW_2N after their respective precursors. The BET surface areas of the resulting tungsten carbide powders were measured to 6 m^2g^{-1} for mWO_3 and 18 m^2g^{-1} for mW_2N.

5.1.3 CsH_2PO_4

CsH_2PO_4 was prepared by precipitation. 30 g $CsCO_3$ (Sigma-Aldrich, 99.9%) was dissolved in 175 mL water. This was done under heavy stirring for a few hours to promote degassing. Addition of 85 % H_3PO_4 (Sigma-Aldrich, puriss) was carried out under constant pH monitoring until a pH of 4.62 was reached. The CsH_2PO_4 was precipitated by slow addition of methanol and the precipitate was allowed to settle over night. The powder was collected, washed in methanol and dried 2 days at 90 °C before use. XRD showed a pure crystalline power.
As an alternative a SiC whisker reinforced CsH_2PO_4 electrolyte was synthesised by PhD Daniel Risskov Sørensen from the University of Southern Denmark (SDU). 72 g beech wood saw dust was soaked in 180 mL 96 % ethanol. 22 mL HCl (Signa-Aldrich, 37%) was then added together with 40 mL tetraethyl orthosilicate (TEOS, Sigma-Aldrich 99.999%) and the mixture was stirred for 6 hours. The resulting slurry was then allowed to dry overnight and the resulting solid was ground, placed in an alumina crucible and heated to 1500 °C at a ramp of 5 °C/min in a tube furnace under an argon flow of 300 mL/min. It was kept at 1500 °C for 6 hours and allowed to cool to room temperature at 10 °C/min. The resulting mixture was dispersed in 500 mL distilled water in a separation funnel. 5g of aluminium sulphate was added and after shaking the funnel and letting it rest the bottom part of the water phase was transferred to a separation funnel. The process was repeated first with 20 mL toluene and 1 g aluminium sulphate and then 20 mL chloroform and 1 g aluminium sulphate. The process was repeated until the desired purity of SiC whiskers was achieved. The whiskers were then washed, centrifuged and dried at 100 °C overnight. CsH_2PO_4 was the deposited onto the whiskers by dissolution and re-precipitation in water. The material tested in this work had a reinforcement of 5 wt.% SiC whiskers. The resulting product was denoted as CsH_2PO_4-SiC.
Lastly a reinforced electrolyte was made by mixing CsH_2PO_4 and ZrO_2. 33 wt.% ZrO_2 was added to CsH_2PO_4 and the mixture was ground thoroughly in a mortar. This mixture was denoted CsH_2PO_4-ZrO_2.

5.1.4 $Sn_{0.9}In_{0.1}P_2O_7$

Table 5.1: Synthesis details for $Sn_{0.9}In_{0.1}P_2O_7$ samples. Ramp, texture and end temperature referes to the paste formation process. For quenching a no denotes that the furnace was allowed to cool before the sample was removed. A yes means that the crucible was removed from the furnace at 650 °C and left to quench in air.

Sample	Ramp from 90 °C	Texture	End temp.	Quenching
A	Raised in increments of 50 °C dwell 15 min	Hard clay-like	285 °C	No
B	Raised in increments of 50 °C dwell 15 min	Soft clay-like	265 °C	Yes
C	Raised in increments of 50 °C dwell 15 min	Soft clay-like	285 °C	No
D	Direct ramp to 300 °C	Soft paste/hard paste	298,5 °C	No
E	Direct ramp to 280 °C	Soft paste/hard paste	278 °C	No
F	Direct ramp to 280 °C	Soft paste/hard paste	278 °C	No

All samples of $Sn_{0.9}In_{0.1}P_2O_7$ used in this work were synthesised by the previously mentioned oxide synthesis route (Section 3.2.3). A 80 nm SnO_2 precursor (Inframat advanced Materials, 99.9%) was mixes with In_2O_3(Aldrich, 99.99% trace metals basis) and mortared. The powder mixture was dispersed in 25 mL water and mixed with 85 wt% H_3PO_4 (Sigma-Aldrich, puriss) in a phosphorous to metal ration of 2.8. The mixture was placed in a Pyrex cylindrical beaker which was in turn in a cylindrical aluminium heat exchanger. A glass spatula fixed to a motorised stirrer ensured an even and constant stirring of the mixture. A thermocouple was placed in a wall of the aluminium heat exchanger for temperature control. The temperature was first increased from room temperature to 90°C within an hour, by which most of the water was evaporated. The temperature controller was then set to 300°C and the mixture was kept under constant stirring until a viscous paste was obtained. This happened before reacting 300°C and the synthesis had to be monitored constantly so it could be interrupted the moment the paste was formed. The resulting paste was transferred to an alumina crucible and further heated with a lid to 650°C with a temperature ramp of 180°C/h and kept at this temperature for 3 hours. The furnace was allowed to cool before the crucible was removed. The material obtained by the above synthesis procedure was ground and kept in a desiccator.
The oxide synthesis route is hard to control in a reproducible manner. Prior to settling on the above described synthesis route other variations were tried. These are summarised in Table 5.1. The method described above corresponds to the sample denoted (F). Characterisation of these materials will be covered in Chapter 7.

5.1.5 $Sn_{0.95}Al_{0.05}P_2O_7$ and $Sn_{0.9}Mg_{0.1}P_2O_7$

Additional electrolytes were synthesised. $Sn_{0.95}Al_{0.05}P_2O_7$ and $Sn_{0.9}Mg_{0.1}P_2O_7$ were synthesised by a route analogous to the one described above for $Sn_{0.9}In_{0.1}P_2O_7$. In_2O_3 was substituted for $Al(OH)_3$ and $Mg(OH)_2$ in the respective synthesis.

5.1.6 Bismuth phosphate

The following synthesis work was done by PhD Y. J. Huang during his stay at DTU Energy Conversion.[59]
Bi_2O_3 was mixed with 85 % H_3PO_4 (Sigma-Aldrich, puriss) at an initial molar ratio of P/Nb of 1.8. This mixture was then heated to 200 °C under conditions analogous to those described in Section 5.1.4 for $Sn_{0.9}In_{0.1}P_2O_7$. The paste was placed in a crucible and heated to 650 °C for 3 hours. The furnace was allowed to cool down before the sample was removed. The resulting powder was ground with a mortar and pestil and stored in a desiccator. The material was denoted Bi-P.

5.1.7 Niobium phosphate

The following synthesis work was done by PhD Y. J. Huang during his stay at DTU Energy Conversion.
The synthesis was based on the work of Kishor et al.[131] who demonstrated a synthesis route for making nano sized microporous niobium phosphate. The exact structure of this material is undetermined. In our case an extra step was introduced where the microporous

powder was heat treated together with phosphoric acid in order to increase its protonic conductivity.
2 g of $NbCl_5$ was added to water, approximately 40 g, for partial hydrolysis. H_3PO_4 85 wt.% (Sigma-Aldrich, puriss) was added in a molar excess of 2 relative to Nb. Additional 40 g water was added and after stirring for 30 min aqueous ammonia was added until pH 2.60 was reached. The formed precipitate was filtered, washed in demineralised water, was placed in a beaker and 10 g of water was added. 1.10 g hexadecyl amine (Sigma-Aldrich, 98 %) was added and after 30 min of stirring 0.68 g 85% phosphoric acid was added as well. The mixture was stirred for 30 min while monitoring the pH making sure it was under 3.88 and a gel was formed. This was placed in a Teflon lined stainless steel autoclave. Reaction under autogeneous pressure was carried out for 2 days at 65 °C. The resulting product was washed, filtered, dried at 100 °C and calcined at 450 °C for 6 hours. The resulting powder was ground and an excess of phosphoric acid was added before it was heat treated at 650 °C for 3 hours. The resulting product was denoted Nb-P.

5.2 Pellets and reinforcements

The synthesised powders were formed into testable electrolyte pellets by uniaxial pressing. As will be discussed in Chapter 6 the initial cell housing design required electrolyte pellets of 40 mm diameter. For these pellets PBI was used as a binder. The electrolyte was mixed with a 6.1 wt.% PBI in dimethyl acetamide (DMAC) solution (in-house made) to add 6 wt.% PBI. The mixture was mortared thoroughly and the DMAC was evaporated under suction at 150 °C. This mixture was used as a precursor for electrolyte pellets. Pristine electrolyte was mixed with the PBI soaked electrolyte in a ratio of 4:3 and ball milled in a planetary ball mill for 1 min at 300 rpm. The crucible and balls used were lined with tungsten carbide and were heated to 90 °C to minimise the uptake of water by the electrolyte during milling. The resulting powder mixture was transferred to a pressing tool and hot pressed at 80 °C for 2.5 hours with 30 tonne. The die was cooled and pressed for 1 min with 20 tonne to make disassemble easier. These electrolytes were tremendously hard to handle and only one in eight actually made it to testing without breaking during the pressing procedure or the cell assembly. For this reason these sizes of pellets were abandoned and a new cell housing was made.
The new cell housing was designed for 20 mm pellets (Section 6.1.7 and 6.1.8). These were uniaxially pressed at room temperature in a pressing tool using 10 tonne for 5 min. For Nb-P, CsH_2PO_4, CsH_2PO_4-SiC, CsH_2PO_4-ZrO_2 and $Sn_{0.9}In_{0.1}P_2O_7$ no binder was needed. The powders were pressed as synthesised and gave easily handleable pellets. Bi-P however needed a binder to be pressed into a cohesive pellet and 2 wt.% PBI was added by the same procedure as described above.
As a result of shifting to smaller electrolytes the size of the electrodes was reduced to 13 mm in diameter (A = 1.33 cm^2).

5.3 Tantalum coated Gas Diffusion Layers

The GDL on the anode side on an electrolyser needs to be able to handle the very oxidative environment created by polarisation and oxygen formation. It will be in direct contact

with the acidic electrolyte as well. As one of the great advantages of IT electrolysis compared to SOEC is that materials used in PEM electrolysis may be applied it would appear obvious to use titanium felt or sinter as GDL. However, work previously done it our group[132] has shown that titanium has a high corrosion rate in the presence of hot phosphoric acid and polarisation. Samples tested in 85 wt.% H_3PO_4 at 120 °C at potentials up to 1.1 vs. standard hydrogen electrode (SHE) showed a corrosion current of 6.3 mA corresponding to an approximate corrosion rate of 73.3 mm/year. While the surface acidity of the electrolytes, a property notoriously hard to quantify and qualify,[133] used in this work may not in absolute terms be comparable to the acidity of the phosphoric acid they may hold some of its properties. Especially the $Sn_{0.9}In_{0.1}P_2O_7$ which derives its protonic conductivity from an immobilised phosphoric acid phase may at local contact points with a GDL have properties sufficient for detrimental corrosion.
In order to avoid the least chance of corrosion interfering with our electrolysis tests tantalum was chosen as a protector against corrosion. In the previously mentioned study[132] it was seen that tantalum under the same conditions had a corrosion current of $6.3 \cdot 10^{-5}$ mA corresponding to an approximate corrosion rate of $1 \cdot 10^{-3}$ mm/year. Further more its low electric resistivity, 12.2 $\mu\Omega\cdot$ cm at room temperature and $\approx$ 21.8 $\mu\Omega\cdot$ cm at 200 °C[134], ensures good conductivity through the protected component. The quoted resistivity may be a bit misleading as it is not the pure tantalum that is responsible for the actual corrosion stability. This seems to originate from a protective layer of Ta_2O_5 formed on the surface of the metal. An XPS study by Lecuyer and coworkers[135] indicated that the naturally formed oxide layer was 3 nm thick with 1 nm thick suboxide TaO clusters scattered along the interface of the tantalum and the Ta_2O_5. This thin naturally formed oxide layer did not impede heavily on the electronic conductivity. A study by Shimizu et al.[136] investigated the anodic formation of oxide layers in 85 wt.% phosphoric acid. Using a 500 nm thin tantalum film on aluminium a current of 1 mA/cm^2 was applied and an oxide layer began forming. The resulting voltage rose with the thickness of the oxide layer and the experiment was stopped at 60 V. Specimens stopped at this forming voltage showed an outer layer of PO_4^{3-} doped tantalum, 50 nm thick, and a 21 nm thick Ta_2O_5 at the interface between the phosphate layer and the pure tantalum metal. Thus formation of layers much thicker than the naturally occurring 3 nm were promoted by the anodisation. This shows the importance of both the naturally occurring layer and keeping a low voltage to hinder the oxide growth.
The anode GDLs used were made from woven stainless steel felts (SSF) 500 μm thick. One side of the felt was woven with thin fibres (8μm) and the other with thick fibres (12 μm). The side with the thin fibres gave smaller pores thus giving a larger surface area with more contact points to be in contact with the electrolyte. The larger pores on the side with the thicker fibres allowed for easier access of gas into the felt. To create a corrosion resistant GDL tantalum was coated onto the felt by chemical vapour deposition (CVD) . In this technique a solid phase is deposited onto the surface of a substrate from the gas phase. A precursor compound containing the desired metal, in this case $TaCl_5$, is vaporised allowing for the metal ions to reach the substrate surface in a uniform manner and form solid metal. This method gives a highly uniform surface coating with great adhesion to the substrate. It allows the coating to reach nooks and crannies other techniques cannot reach. The layers of metal deposited generally have thicknesses in the order of 2-4 μm. Therefore when dealing with a geometry as sophisticated as a woven felt with varying thread thickness CVD was seen as an ideal match.

Going back to the protective oxide layer on the tantalum surface it should be mentioned that Hansen et al.[29] investigated Ta coated SSF similar to the GDLs just described. Using tantalum foils and said felts to experimentally approximate the conditions at the GDL/flow plate interface and measuring the contact resistance at given clamping pressures it was seen that only a small contact resistance arose at the interface of these materials, e.g. 3 mΩ cm^2 at 2 MPa clamping pressure. These results were better than the target of 10 mΩ set by the DOE for fuel cell GDL/bipolar plate contact resistance to be reached in 2020 (no such target exists for electrolysers). This lead to the conclusion that the naturally formed oxide layer on the tantalum did not impede the electric conductivity significantly.

Table 5.2: The specific conditions, dimensions and results for the coating of tantalum onto two pieces of stainless steel felt initially identical. Both were cut from identical 15 cm by 15 cm sheets of felt. The deposition rate is for a reference sample

Sample	Dimensions	Temperature	Time	Weight gain	Deposition rate
Felt 1	15 cm · 5 cm	825 °C	6 Hours	0.397 g/cm^2	5 μ/hour
Felt 2	15 cm · 7.5 cm	825 °C	2 hours	0.270 g/cm^2	10 μ/hour

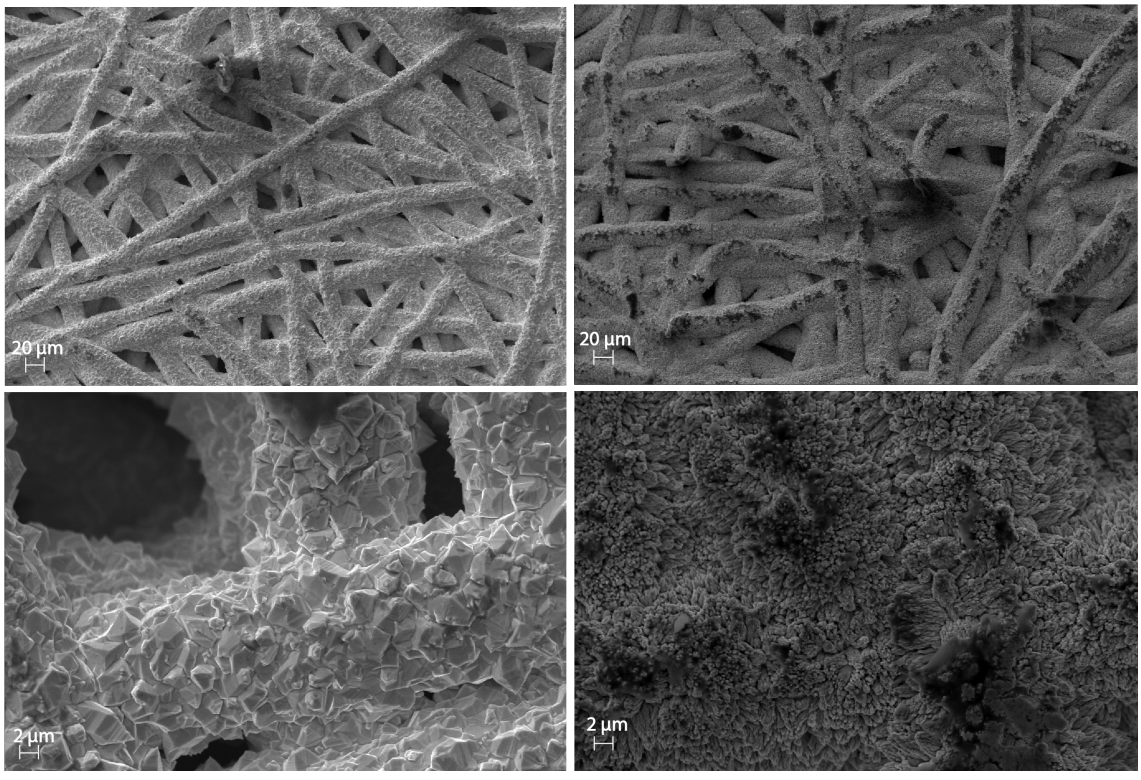

(a) (b)

Figure 5.1: The difference in tantalum coatings of stainless steel felt (a): Felt 1 with a loading of 0.380 g/cm^2 (b): Felt 2, loading of 0.270 g/cm^2.

The amount of tantalum deposited during CVD is highly dependant on reaction temperature as well as the size of the substrate and position of the substrate in the furnace

relative to the gas inlet. As an example of this can be considered the two kinds of Ta coated felt used for anode fabrication in this work. Denoted felt 1 and felt 2 they are shown as SEM images in Figure 5.1 and their data and CVD conditions can be found in Table 5.2. The deposition rate is for a reference sample and is not a measure of the amount actually deposited on the felt.
Prior to tantalum coating the felts were identical and as described above. It is clear that even though the amount of tantalum deposited on felt 1 is larger than the amount on felt 2, 0.380 g/cm^2 compared to 0.270 g/cm^2, felt 2 has a much more closed surface. This indicates a higher degree of coating on the surface of felt 2 where it can be assumed that the gas stream has penetrated deeper into felt 1. The most likely explanation for this is the higher deposition rate for felt 2. If faster growth of the deposited layer is promoted the pores of the surface will close at a higher rate and less tantalum will penetrate into the felt. This will accelerate the deposition on the surface as a smaller surface area is available for deposition. Evaluation of each batch of felt was needed even for samples coated at seemingly similar conditions.
The amount of tantalum and whether it was deposited heavily on the surface or throughout the felt was also found to be of great importance for mechanical reasons. When making anodes pieces of Ta coated stainless steel felt were cut from the coated sheets using a swinging arm press (ATOM spa, SE series) using a die 13 mm in diameter. Whole uncracked felt pieces were needed and it was found that if amount of deposited tantalum was too little, such as 0.240 g/cm^2 for felt type 1 and 0.167 g/cm^2 for felt type 2, the felt pieces would bend rather than being cut from the sheet. On the other hand if too much tantalum was deposited, examples include 0.486 g/cm^2 for felt type 2, the felt was to brittle for the stamping process and the surface of the felt would crack exposing the stainless steel felt fibres. These troubles are in large parts caused by the diminutive size of the pieces being cut. Previous experiences in our group with larger felt pieces[28] did not reveal such problems.

5.4 Catalyst layer spraying

5.4.1 Anode

The majority of the anodes used in this work were based on the above described Ta coated SSF and IrO_2. All electrodes were made by hand spraying a catalyst ink onto the felt using an air brush (Badger no 100LG). The ink consisted of 5 mL ethanol, 12 mg IrO_2 and 12 mg electrolyte or 12 mg IrO_2 and 3 mg electrolyte. The mixture was ultrasonicated for 2 hours before spraying. The ink was sufficient to spray two pieces of felt creating 2 anodes simultaneously. This saved time and made it possible to make identical cells as the anodes were essentially identical.
The Ta coated felt used had a large influence on the finished anode. This is illustrated in Figure 5.2 where anodes made with felt 1 and felt 2 are shown. The electrolyte is $Sn_{0.9}In_{0.1}P_2O_7$ for both anodes and the electrocatalyst is IrO_2. As felt 2 has less tantalum per cm^2 and smaller loading of catalyst and ionomer this must be a result of the more closed surface the CVD of tantalum has created on felt 2. The anode made with felt 2 clearly has blocking of the pores making it impossible for the steam to get the surface of the electrolyte. As the ethanol may have removed some or all of the protonic conduct-

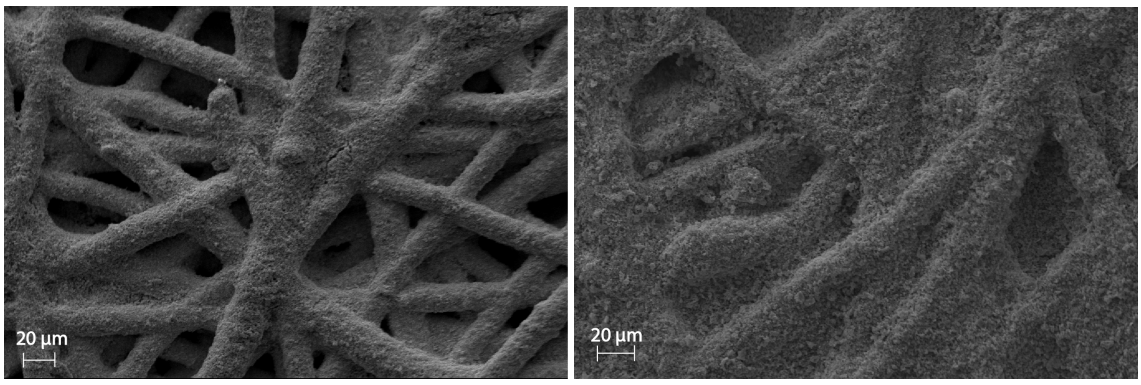

(a) (b)

Figure 5.2: The influence of the amount of tantalum on the surface of the anode GDL on the catalyst layer (a): Felt 1, loading of 3.7 mg/cm^2. (b): Felt 2, loading of 3.0 mg/cm^2.

ing amorphous phase the ionomer in the electrode cannot be relied on for proton transport to the electrolyte and the steam has to reach the electrolyte-electrode interface if we want to be certain of reaction. Furthermore if reaction could only take place in the electrode the protonic transport distance would become quite large the overall effect being a less effective cell. For this reason the ink for anodes made with felt 2 had its contents of $Sn_{0.9}In_{0.1}P_2O_7$ reduced to 3 mg. While optimisation of the electrodes was outside the scope of this project the electrode structure was still monitored to ensure reasonably comparable electrodes were used.
Two alternative anode materials were explored preliminarily. $LaNiO_3$ was made into an ink as described for IrO_2. 21.5 mg $LaNiO_3$ and 2.5 mg $Sn_{0.9}In_{0.1}P_2O_7$ was used. After spraying the total loading of the electrode was 4.8 mg/cm^2. The second alternative material was a 1.1 mm thick Ni foam (American Elements, 110 PPI). This was cut to electrode size and used directly as a combined GDL and electrocatalyst.

5.4.2 Cathode

Two different GDLs were used for cathode electrodes. One was the previously mentioned Ta coated SSF and the other was a Toray paper GDL. The Toray paper was a Teflon treated Toray paper (H120) with a tape-cast microporous carbon layer (Vulcan® XC72R carbon black, PTFE). The most used electrocatalyst layer was platinum black (Sigma-Aldrich, 99.97% trace metals basis, $\leq 20\mu$m), platinum supported on carbon (57 mass% Pt, Johnsson Matthey) and ionomer which was suspended in ethanol and hand-sprayed onto the Toray GDL. The ratios were 6:2:1 for the components respectively. The Toray paper was heated to 70 °C and the ink was carefully sprayed onto the paper to avoid ignition of the carbon and/or ethanol. Loading varied from batch to batch and will be specified at the relevant experiments. The average Pt loading was around 9 mg/cm^2.
For initial experiments only Pt/C was used. Otherwise the procedure was the same. This gave platinum loadings of around 1 mg/cm^2. Relevant loadings will be given at the individual cell results.
For tungsten carbide electrocatalysts, mWO_3 and mW_2N alike, inks of 12 mg WC in

ethanol were made, ultrasonicated and pipetted unto cut pieces of Toray paper of 13 mm diameter heated to 50 °C. This lower temperature was used to limit oxidation of the tungsten carbide.
For Ni foam it was cut and used similarly to what was described for Ni as anode material.

CHAPTER 6

Setup construction and operation

A central part of this work was the design, selection and production of components for the electrolysis setup used. This task built on the experience and materials from work previously done in the group.[28] Unique challenges were met as the system had to accommodate brittle electrolytes and temperatures between 200 °C and 400 °C in addition to the harsh electrolysis conditions. This meant that a range of components had to be developed. Operation and data collection from the setup will also be described in this chapter.
A picture of the system, configured for testing with steam on both electrodes, can be seen in Figure 6.1

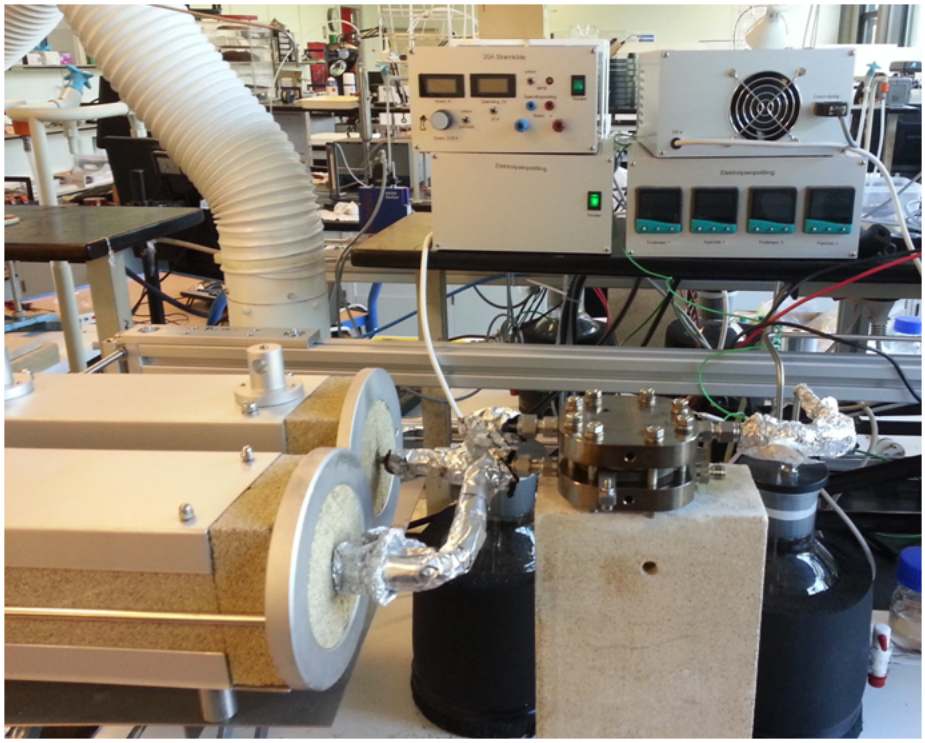

Figure 6.1: Picture of steam electrolysis setup used in this work.

6.1 Construction of the setup

In this section the materials and components used in the setup will be presented. Iterations of components will be discussed as well.

6.1.1 Components

The basic setup was of fairly simple design. It comprised of the following components:

- a VersaSTAT 4 potentiostat running VersaStudio v2.20.4631 (Prinston Applied Research)
- an in-house made data collection box
- an in-house made temperature controller
- two in-house made evaporators
- two in-house made condensation units
- two in-house assembled peristaltic pumps with PVC tubing of 1.42 mm^2 inner diameter (Mikrolab)
- two 250 W heating rods, L = 60 mm, ⌀ = 6.5 mm (SAN Electro Heat)
- one type K thermocouple
- an in-house made electrolyser cell housing consisting of end plates and flow plates

The piping was done with 316L stainless steel pipes (outer diameter = 6 mm, inner diameter = 4mm) and the fittings used were 316L Swagelok® fittings. A schematic drawing of the setup can be seen in Figure 6.2. In the following part the different components will be gone through in detail.

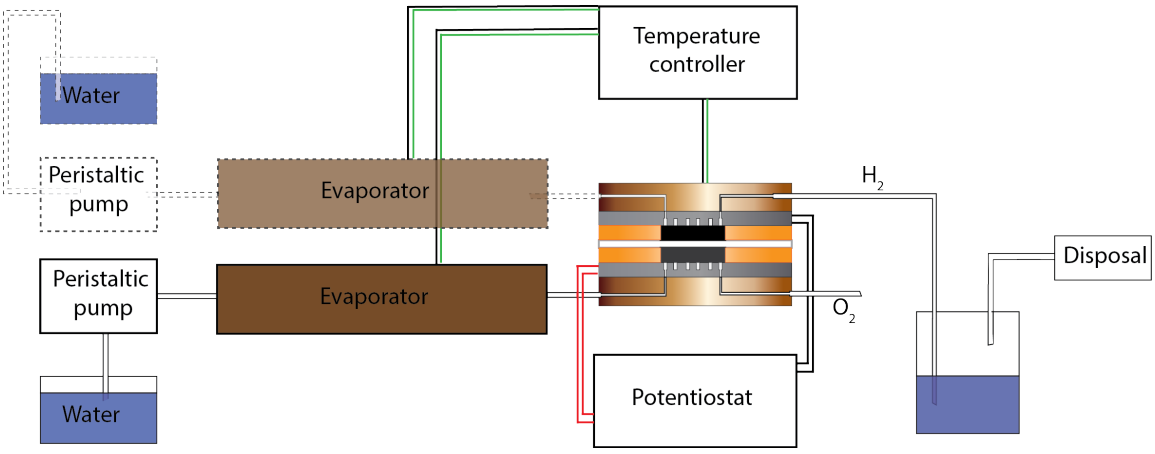

Figure 6.2: Schematic representation of steam electrolysis setup. Dashed lines indicated equipment included only when steam was used on both sides of the setup.

6.1.2 Power supply/Potentiostat

Initially an in-house made power supply was used for the setup. This could provide currents up to 20 A but had the tendency of supplying 20-40 mA more than it was set

to. The current could be set either by using in-house made software which could also control temperature and collect data or manually by turning a nob. As will be discussed further down cells tested were initially 11.6 cm^2 of area. This meant that the oversupply of current was a nuisance but not detrimental in any way as even cells only capable of accommodating current densities of 30 mA/cm^2 were supplied 348 mA in total. At such currents a 20 mA oversupply of current did little to influence the measurement. However when a shift was made to cells of only 1.33 cm^2 (see Section 5.2) this discrepancy made the power supply unusable. As an alternative power supply and data collection device a VersaSTAT 4 potentiostat was chosen. This allowed for experimentation with high precision ($\pm$0.2% of range) at very low current densities. Further the potentiostat had impedance capabilities making it possible to evaluate the cells by EIS, a considerable improvement over the previously used power supply. The potentiostat was used for two point measurements with the working and sense electrodes connected to the anode flow plate and the counter and reference electrodes connected to the cathode flow plate. When a reference electrode was introduced in the cell (see Section 6.1.10) anode to reference measurements were done with the anode as working and sense electrodes, the platinum wire as reference and the cathode as counter. For reference electrode measurements of the cathode it was set as working electrode and sense electrode and the platinum wire and the anode were reference and counter electrodes respectively.
No results of experiments done with 11.6 cm^2 cells will be detailed here as they yielded little to none usable information apart from the fact that were too unwieldy to be practical. The power supply has only been detailed here in the interest of full disclosure.

6.1.3 Data collection box

The data collection box was only used in the initial version of the setup. When the potentiostat was introduced it was dismissed. When used it was connected to the temperature controller, the power supply and a computer. It allowed for temperature, current and voltage to be recorded as a function of time.

6.1.4 Evaporator

The in-house built evaporators were designed by Ph.D. student Anton Vassilev. The design is shown in Figure 6.3. The core of them were a 250 mm long 316L stainless steel pipe ($\varnothing$ = 19 mm). At each end they were fitted with a Swagelok® fitting and a copper gasket. At one end of the pipes a 100 mm piece of pipe, same kind as mentioned in Section 6.1.1, was fixed to allow for connection to the cell housing (see Section 6.1.7). The large pipes were filled with stainless steel balls and stopped with a small piece of 316L stainless steel mesh in each end to prevent the balls from escaping the tube through the hole in the fitting. In one end of the pipe a capillary tube was lead in through the Swagelok® fitting and approximately 100 mm into the pipe. This was done to optimise the evaporator for a continuous supply of steam as this allowed for evaporation of the water before it hit the balls in the tube. The evaporator pipes were wrapped in heating tape. In between the pipe and the heating tape was placed a type K thermocouple. The pipe was dressed in vermiculite for insulation. The end of the pipe connected to the evaporator pipe protruded form the insulation block allowing the evaporator to be connected to the cell housing. The capillary tube was connected to the peristaltic pump via a flexible PVC

tube of inner diameter 1.42 mm^2 (Mikrolab).
The choice of having the capillary tube penetrate some two fifth into the evaporator pipe

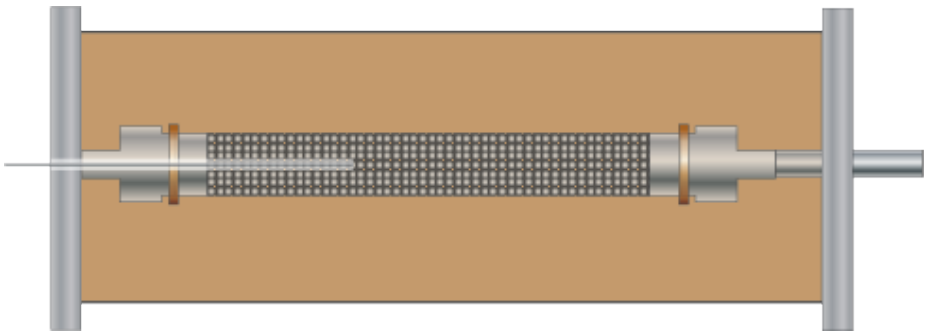

Figure 6.3: Schematic representation of an evaporator. A capillary tube leads water into a pipe filled with stainless steel balls. The pipe is encased in vermiculite for insulation. Heating tape and thermocouple for heating the pipe is not shown.

was seen to be quite effective at low pump speeds and gave a steady supply of steam. It was however seen that the steam supply had its challenges when the evaporator could not be connected directly to the end plates, more on this in Section 6.1.7, as additional pieces of piping allowed for the steam to cool and condense in the pipe. This gave an uneven distribution of steam to the cell housing as it had to penetrate the formed droplets or carry them into the cell housing where they evaporated. As an attempt to alleviate this the additional piping was insulated with HT/Armaflex®. This had some effect but did not remove the problem entirely. How severely it impacted a cell was also seen to be tied to the kind of GDL used, more on this in Section 6.4.

6.1.5 Peristaltic pumps

The peristaltic pumps were assembled in-house. They used a HL149.24.43 geared motor (Micro Motors) and were fitted with a 400A peristaltic pump head (Watson-Marlow). They could supply a stable flow of water down to 0.25 mL/min. This was the default flow rate as it was more than enough to supply the anode with steam continuously at the usual operating current density of 7.5 mA/cm^2. This was seen by calculating the amount of water converted at the given current density using Faraday's law. During polarisation more steam was consumed than was supplied at higher current densities, above $\approx$ 34 mA/cm^2. This was initially not considered a concern as this was generally above what the cells could handle before exceeding 2.0 V. When cells capable of going up to much higher current densities were developed this had to be taken into account. It was noted that if the supply was left at 0.25 mL/min no mass transport limitations were observed during recording of polarisation curves. This was attributed to the polarisation experiments only applying these higher current densities for short periods of time, too short time to deplete the cache of steam in the cell housing and flow plates. Therefore this flow rate was still used for these improved cells. At higher operation current densities higher flow rates were needed. For 150 mA/cm^2 Faraday's law showed the need of a minimum steam supply of 1.12 mL/min and the flow rate was set to 1.5 mL/min to ensure a large enough supply of steam.

6.1.6 Condensation units

The condensation unit was of in-house design and production. The central component was a glass bottle insulated with HT/Armaflex®. Inside the bottle was fitted a cooling spiral and the bottle was half-filled with water. The water circulated in the cooling spiral was kept at 5 °C by a circulation of water cooled to this temperature. The circulated water was cooled when it returned to a reservoir equipped with a cooler (Haake EK12). Thus the water in the flask was kept at 5 °C as well and the outlet from the cathode side of the electrolyser was lead through this water and chilled. The chilled gas was then allowed through a pipe and disposed of.

6.1.7 End plates

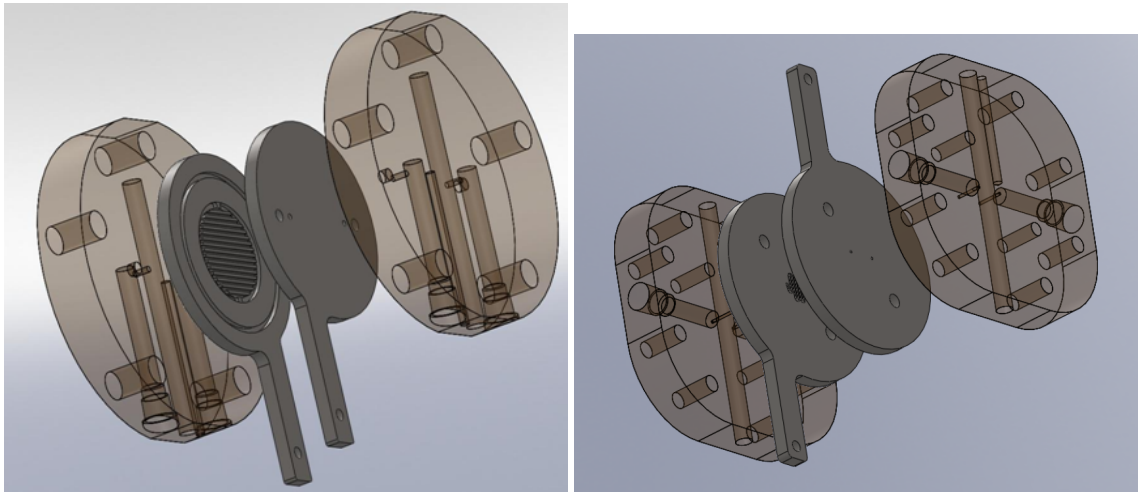

(a) (b)

Figure 6.4: The two types of electrolysis cell housings developed. (a) shows the initial design where cells of active area 11.6 cm^2 could be accommodated. (b) shows the final design made for cell with a 1.33 cm^2 active area.

The cell housing consisted of two components. A pair of end plates and a pair of flow plates.
The end plates needed to withstand thermal cycling from room temperature to 400 °C without deformation. At the same time they needed good thermal conductivity and the material used needed to be easily machinable. This list of demands lead to the choice of an aluminium copper alloy with the nominal composition of CuAl10Fe5Ni5 (JM7-20, Johnson metall). For previous work in the group aluminium had been used but it was deemed too likely to oxidise at the high end of the temperature range.[137] Two distinct generations of end plates were made and used. These were denoted type 1 and type 3. Type 2 was an intermediate type not actually used as it was made too thin. Type 1 and type 3 can be seen in Figure 6.4.
Type 1 was designed to accommodate cells with electrolytes of 40 mm in diameter. As was discussed in Section 5.2 this proved impractical and was abandoned. Apart from impracticality of cell size this design also had some design issues. First of all all four gas

channels (cathode in and out, anode in and out) were on the same side of the cell housing which also was the side where the heating rods and the thermocouple were inserted. The ends connecting the flow plates to the current supply also protruded from here. This gave very little room for connection to these gas channels and an additional problem of no sufficiently plane surface for a Swagelok® fitting and copper gasket, resulting in leaky fittings. This was partly remedied by planing the surface of the end plate where the gas channels were. An additional problem not so easily fixed was a deformation of the end plates caused by the process used for machining them. This resulted in slightly crooked plates and made it in practice impossible to make the cell housing gas tight as gas could escape between flow plates and end plates. The third problem with type 1 was that it was tightened with five 10 mm bolts. Disc springs were inserted in between bolt and end plate and nut and end plate. The uneven number of bolts made it very hard to get an even distribution of force even when the bolts were tightened in a star pattern. The large bolts and springs required a large torque to be fastened, usually 2 N·m but sometimes as high as 4 N·m.
Type 3 attempted to remedy all these issues all the while being designed for flow plates with a smaller flow area. First of all the way the end plates were machined was changed giving completely straight end plates. Secondly the general shape of the plate was changed to a round cornered square. Here the gas inlets and outlets were placed on opposite sides of the end plate and on flat surfaces making it easy to get a gas tight fitting. On one of the two remaining surfaces the channel for the heating rod was drilled and in one of the end plates the channel for the thermocouple was placed. To make the cell housing easier to tighten eight bolts were used ensuring an even distribution of force. These were 6 mm and also supplemented with disc springs. To make assembly of the cell easier holes for steering rods were drilled all the way though the end plates and flow plates. The application of these will be detailed Section 6.2.1. The bolts were tightened to 1 N·m which was found to be enough for a good connection.
One problem seen was with connection of steam to both sides of the cell. When steam was only needed on the anode side of the cell the evaporator could be connected directly to the anode side with no need for additional piping. When steam on the cathode was desired two evaporators were needed and due to the placement of the stationary parts of the setup, such as piping and the condensation flask, they had to be connected to the same side of the cell housing. In this case S-shaped pieces of pipe were needed due to the spacial hindrances. As mentioned in Section 6.1.4 this gave problems with the steam supply. As the evaporators were rather bulky no way of connecting the evaporators without additional piping could be found. Apart from this problem no striking deficiencies were found with this end plate design.

6.1.8 Flow plates

Figure 6.5 shows the flow plates of type 1 and type 3. Flow plate type 1 was made with a 34.5 mm flow pattern. The pattern consisted of parallel channels 1 mm deep and 1 mm wide encircled by a 1.5 mm deep and 2 mm wide channel. The parallel channels were spaced by 1 mm. On opposite sides of the flow channels, as seen along them, an inlet and an outlet hole was drilled. These matched with corresponding holes in the end plates. To make assembly easier two small holes 3.5 mm deep and 4 mm in diameter were made in

Figure 6.5: Two types of tantalum coated stainless steel flow plates. The left is of type 1 and the right is of type 3.

the back of the flow plate again matching identical holes in the end plates. In these holes small ceramic guiding pins were placed to keep the inlets and outlets of flow plates and end plates aligned. This did not however ensure the placement of the anode, cathode and electrolyte between the flow plates.
Shifting to smaller cells meant shifting to smaller flow patterns. Here a simple serpentine pattern was used, 11.5 mm in diameter, 1 mm deep and 1 mm wide. The guiding pin system from type 1 was replaced with a steering rod system where holes were drilled through both end plates and flow plates allowing for stainless steel pins ($\varnothing$ = 5 mm) to keep end plates, flow plates and gaskets in place.
The flow plates intended for use on the anode side were CVD coated with a corrosion resistant layer of tantalum by Tantaline®. This layer was approximately 50 μm thick and was a commercially available coating.

6.1.9 Sealing

Since the goal of this work was to test full cells with both anodes and cathodes a one atmosphere setup would not suffice and sealing was a necessity. Two types of sealing were considered. The first one was sealing of the edges of the cell with a gas tight compound akin to the way usually used for SOFCs.[138] It proved highly problematic to find a compound that could be applied at room temperature but hardened at 200 °C. The second kind was to use electrodes smaller than the electrolyte and use the larger electrolyte in conjunction with gaskets to make a gas tight seal. This method had been used in our group before for polymer membranes[28] and ended up being the chosen method. In the previous work the gaskets had been made of Viton®, a fluoroelastomer (DuPont™), but this was not

suitable for operation at 200 °C or above as it decomposes. The choice fell on Kapton®, a polyimide (DuPont™), as this is stable up to at least 400 °C. A thickness of 0.075 mm was used. The practical application of the gaskets will be discussed in Section 6.2.1.

6.1.10 Reference electrode

For some experiments a platinum reference electrode was used. This was only attempted with cells of type 3. Here a platinum wire was placed on the cathode side of the electrolyte and a small piece of cathode was cut and placed on top of the wire to increase the area of the reference.
A reference placed onto the electrolyte on one side of the cell must be a distance of three times the thickness of the electrolyte away from the electrodes.[139] This ensures that the reference measures a potential corresponding to if it had been placed at the center of the electrolyte. The thickness of the tested electrolytes were in general 600 μm and the reference was always placed at least 2 mm away from the cathode.
As pointed out by Adler and coworkers[139,140] positioning of the cathode and anode can have a large effect on the potential measured by a reference. Misalignment of the two electrodes may lead to the reference measuring an erroneous potential. At misalignments equal to or above the thickness of the electrolyte the effect is substantial. A misalignment of 600 μm could theoretically happen as the thickness of the knife on the cutting tool used for GDLs and gaskets was approximately 600 μm in thickness. A smaller displacement was however much more likely and the displacement difference was assumed to be neglectable due to the relative thickness of the electrolyte.
The above sited works by Adler focus on SOFCs. It has been pointed out by He[141] that there is a significant difference between PEM cells and SOFCs with regards to reference electrodes. However these differences mostly relates to handling of liquids in electrodes and in this regard it has been assumed that the cells presented here are much closer to SOFCs than PEM cells due to their solid electrolyte.

6.2 Operation

With the previously detailed materials and equipment electrolysis experiments were carried out. This section detailed the assembly of the components as well as operation conditions and procedures. Lastly the effects of operation on some of the components in the cells and the setup are discussed.

6.2.1 Assembling

A cell ready for testing in a cell house of type 3 is schematically shown in Figure 6.6. Cells were assembled from the anode and up. Steering rods were placed through the corresponding holes in the end plate and the anode flow plate. Gaskets with holes cut to the size of the electrodes, 13 mm diameter, were then positioned and the anode was placed on top of the flow pattern. The number of gaskets were usually less than what would nominally be expected as this amount resulted in poor contact. Thus for an anode of 500 μm only 6 gaskets of 0.075 mm each were used. This trend of poor contact was seen for the electrolyte and the cathode as well and a similar reduction of the number of gaskets was applied

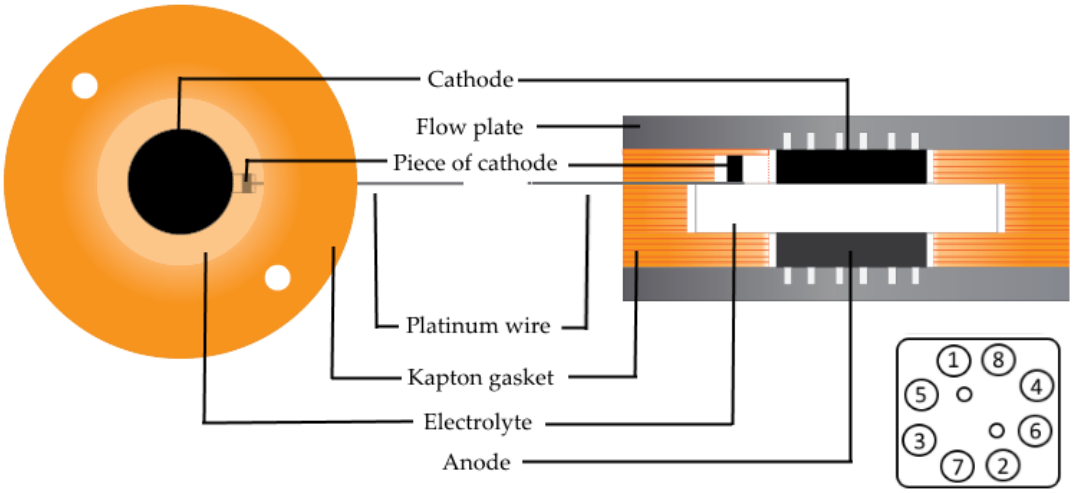

Figure 6.6: Assembly of a cell for cell housing type 3. Here shown for a cell with a reference electrode. Also shown in the order in which the cell is tightened. The figure is not drawn to scale.

for these components.
Gaskets with holes of 20 mm were placed on top of the anode gaskets to accommodate the electrolyte pellet. After placement of the electrolyte gaskets similar to those used for the anode were placed for the cathode. In the case a reference electrode was used the gaskets had a small indent (2 mm by 2.5 mm). Here the platinum wire was slit in and on top of it was placed the small piece of cathode. Care was taken to ensure that there was 2 mm from reference to cathode. On top of the last gasket a small piece of Kapton® tape was placed to seal the reference gas channel. The cathode flow plate was placed on top of the cell assembly. Lastly the cathode end plate was placed. End plates, flow plates and gaskets were all held in place by the steering rods.
Bolts and nuts were then put in place and tightened. This was done with a torque wrench set to 1 N·m. The order in which the bolts were tightened is shown in Figure 6.6. This order was chosen to get as evenly a distribution of force as possible. This tightening procedure was done 3 times before the steering rods were removed. This required some degree of effort as the gaskets were pressed tight around the rods. A parallel pin punch and a hammer frequently had to be used. Even though the electrodes should be held in place by the flow plates the nuts might loosen allowing for the electrodes to move. Therefore care had to be taken. After the rods were removed the cell was tightened again as a way of testing whether the bolts had loosened during the removal of the steering pins.

6.2.2 Startup

First the evaporator(s) were turned on and set to 170 °C. If steam was needed on both electrodes two evaporators were used, otherwise only the anode evaporator was turned on. When the desired number of evaporators had reached the desired temperature heating of the cell housing was initiated. The initial temperature was 100 °C. When the cell

housing reached 100 °C the evaporator pumps were turned on and set to 0.25 mL/min. At the same time the cell housing was set to heat further up to 200 °C. This allowed for the first steam to reach the cell housing as it reached approximately 170 °C. This mitigated condensation and allowed for a very short window of electrolyte dehydration. When the cell housing reached 200 °C the cell was left for one hour before any testing was started.

6.2.3 Test procedure

When a cell had been warmed up electrochemical testing was initiated. First the cell was left at the low current density of 7.5 mA/cm^2 for an hour to see if stabilisation happened. If the cell appeared reasonably stable polarisation measurements were done at 50 mV/s or 20 mV/s. When impedance was being used for evaluation of the cell such measurements were done at frequencies between 10^{-1} Hz and 10^5 Hz at EMF, 1.2V, 1.4V, 1.6V and 1.8V. The amplitude was either 10, 30 or 50 mV depending on the cell. Between measurements the cell was left at low current density (7.5 mA/cm^2) for a number of hours. This number was determined by the nature of the test and will be stated when the individual experiments are discussed in the following chapters.
For reference electrode measurements hydrogen was generally supplied. This was done at 33.5 mL/min (2.01 L/hour).

6.2.4 Shut down

First the steam was turned off and the evaporator disconnected. In the case where the cell housing heated to above 200 °C temperature was set to 200 °C. The heating was left on for 15-20 min. to make sure that flow channels, piping, evaporators and GDLs were free of steam. The evaporators and the cell housing heating was then turned off and the components were allowed to cool.

6.3 Conductivity measurements

The previously described cell housing was re-purposed for conductivity measurements. Pellets of electrolytes were pressed for 5 min at 10 tonne, diameter = 13 mm. Silver paste was painted on both sides of the pellet and it was placed between two flow plates, both of stainless steel. Gaskets separated the two flow plates. The two end plates were connected by tubing and air was lead through both sides of the cell. The flow was set to 100 mL/min and the air stream was lead through a heated water bottle to ensure constant humidification. The humidification was calibrated to 0.15 atm. By two point impedance measurements, from 1 MHz to 1 Hz, the conductivity of the electrolyte was measured at a temperature range from 200 °C to 400 °C.

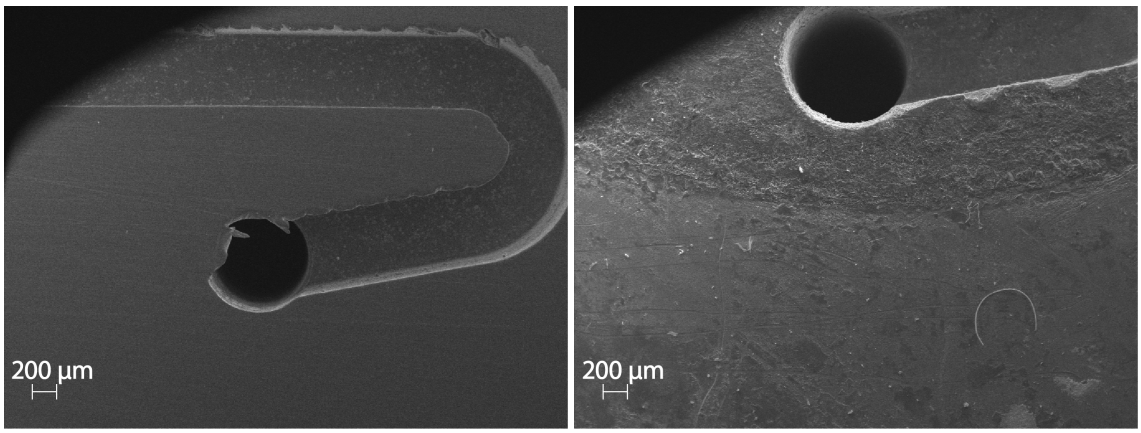

(a) (b)

Figure 6.7: A pristine and a used stainless steel flow plate. (a): the pristine cathode flow plate. (b): a used flow plate bearing marks of use.

6.4 The effect of electrolysis operation on components

As mentioned multiple times the conditions for electrolysis are harsh. It was thus vital to keep an eye on the equipment and materials to make sure that they actually stood up to the conditions as well as expected.
The flow plates were in contact with the electrolysis cell itself and exposed to the same conditions as the GDLs. Therefore evaluation of the state of the flow plates was done after each electrolysis test. Visual inspection was mostly the only thing done but if this revealed discrepancies measurement of resistance of the flow plate was done. SEM was used for a more thorough visual inspection.
The stainless steel cathode flow plates were investigated. Initially a resistance of 0.4-0.5

Table 6.1: The contents of Mo, Ni, Cr and Fe in cathode flow plate in %. Before and after electrolysis use is shown for surface, flow channel and the part of the surface under the electrode.

Flow plate	location	Mo	Ni	Cr	Fe
Before	Surface	2.0	9.2	18.0	70.7
	Flow channel	2.1	11.1	18.1	68.7
After	Surface	2.5	11.2	20.0	66.4
	Electrode area	1.8	11.0	19.9	67.3
	Flow channel	1.7	9.7	21.1	67.5

Ω was measured. This was measured both back to front and through plane of the flow pattern side alike. It was seen that after use of a cathode flow plate for a length of time corresponding to a least one week it became impossible to precisely measure the resistance of the flow plate where it had been in contact with the GDL. Here the resistance as measured with a voltmeter varied erratically and never stabilised.
SEM and EDS were used to investigate the cause of this behaviour. A pristine flow plate and a used flow plate are shown in Figure 6.7. The smooth surface of the pristine flow plate was replaced by a much rougher surface. This was especially true for the part of

the flow plate that had been in contact with the gas diffusion layer. The ratio of elements in the flow plates were calculated from EDS data (Tabel 6.1). No clear trend was seen indicating that no specific elemental oxide is covering the surface of the stainless steel flow plate where it had been in contact with the electrode. A high presence of carbon, oxygen, phosphorous and platinum was seen (not shown). Between each operation the flow plates were rinsed with water in an ultrasonic bath for at least an hour. Thus these elements were not present as lightly adhering detritus but instead a strongly adhering phase. It is likely that corrosion on the cathode had created a rough surface making it possible for a poorly conducting phosphate phase formed from the electrolyte to stick. For illustration Figure 6.8 shows the interface between the part of the flow plate in touch with the electrode (upper) and the part not in contact (lower). While some phosphate was found in the dark blemishes in the lower part it was nothing compared to the rough surface in the upper part. The platinum was found to be present all over the contact area as 10-25 μm large particles. As mentioned in Section 5.4.2 the platinum black used for the cathodes were reported by the supplier to be ≤ 20 μm.

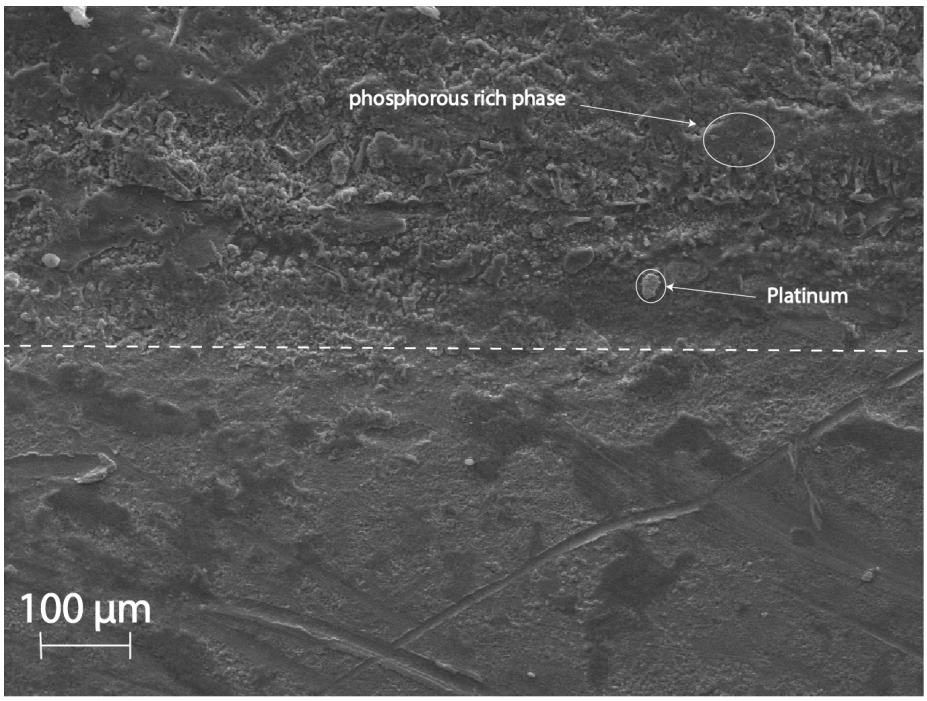

Figure 6.8: A phosphate layer was formed on the part of the cathode flow plate in contact with the electrode (upper part). This is believed to be the reason for the increased ohmic resistance in the flow plate.

The clear corrosion observed lead to a shift to Ta-coated flow plates on the cathode as well as the anode. While the Ta flow plates used on the anode showed the presence of phosphorous on the surface as well (not shown) it was not concentrated around the flow pattern and no apparent etchings were observed. The measured resistance of the flow plate was 0.4-0.5, as with the pristine stainless steel flow plates, at all times. One concern

with the shift to Ta coated flow plates for the cathode was hydrogen embrittlement. The flow plates were investigated carefully after use on the cathode. No raising resistance was seen. It was thus deemed suitable for these relatively short experiments. It may however not be suitable for longer experiments with larger cells. Here hydrogen embrittlement may become a serious factor.

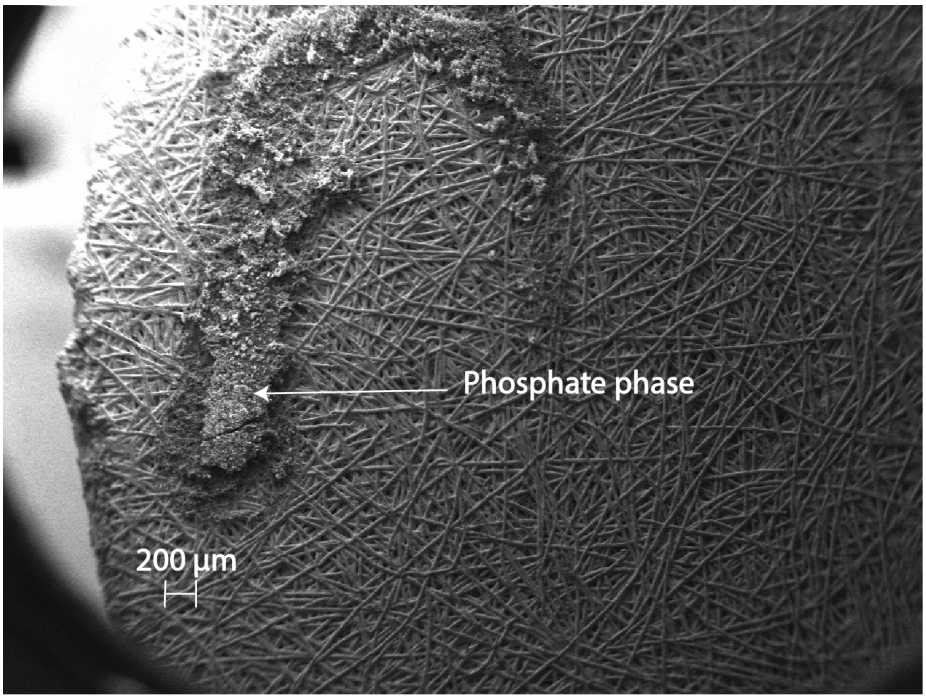

Figure 6.9: Phosphate built-up on the back of an anode due to condensation of water in the cell housing and in the GDL.

Other components showed other modes of failure. The evaporators had to be serviced if the steam flow was observed to become oscillating. It was generally found that steam fluctuations were due to blockage of the capillary tube or the tube connecting the evaporator pipe to the cell housing. The latter was especially a risk when two evaporators were in use and as the spacing pipes made it hard to avoid condensation of water. If the shut down protocol was not observed immediate blocking could happen. Figure 6.9 shows the repercussions of lowering the temperature of the cell housing too soon. Water condensed in the channels and flooded the electrode. The water the flowed back into the piping carrying phosphate from the electrolyte with it. The figure shows the back of an anode of a cell run after this incident. A phosphate rich phase with the shape of the flow channel was seen. This had been pressed into the anode flow plate by steam and been deposited on the anode backside. The steam flow behaved irregularly and the measurements recorded were varying wildly. The evaporator had to be disassembled and cleaned and the flow channels in the cell housing had to be cleaned by drilling.

CHAPTER 7

Pyrophosphates

This Chapter concerns pyrophosphates. Physico-chemical investigations and electrochemical results from testing of electrolyser cells will be covered and discussed in the following. This Chapter will in large parts be devoted to the material denoted $Sn_{0.9}In_{0.1}P_2O_7$. As will be discussed in Section 7.1.4 this composition is nominal not actual and should not be taken as such.

7.1 Physico-chemical Analysis of Electrolytes

Physico-chemical characterisation was used to evaluate produced electrolytes before cell testing. This allowed for a measure of prediction of the conductive properties and performance of the electrolyte. Evaluated characteristics include chemical composition, morphology, amorphous species and by extension ionic conductivity.

7.1.1 FT-IR spectroscopy

FT-IR spectroscopy was used to evaluate electrolyte materials after synthesis but before electrochemical testing. This allowed for an evaluation of a given synthesis path without the need of electrochemical testing.
As mentioned in Section 3.2.4 Xu et al.[79] established a correlation between conductivity of $Sn_{0.9}In_{0.1}P_2O_7$ and the size of the broad band (2500 cm^{-1} to 3600 cm^{-1}) found in FT-IR spectra. This band is believe to stem from an O-H vibration,[142] more specifically PO-H stretches.[143] If it did not stem from a PO-H vibration it would have to stem from a HO-H vibration. This is unlikely however as the materials have been heat treated at 650 °C. Thus the IR signal is due to phosphoric acid[79] either in a mobile form or a form with restricted mobility. This relation between the IR band and the conductivity was used for a qualitative comparison of samples from different batches.
Master students Troels Lie-Andersen and Erik Pristed Jensen synthesised a $Sn_{0.9}In_{0.1}P_2O_7$ sample, here denoted as (CA3), showed promising characteristics. It was attempted to emulate this material. The synthesis pathways followed in this attempt are given in Table 5.1 in Section 5.1.4. A comparison of the FT-IR spectra for said batches can be found in Figure 7.1.
It was seen that the synthesis procedure influenced the O-H stretching band drastically. Direct ramping and lower ramp temperature gave a more pronounced response. Thus the phosphoric acid species responsible for the signal was present in a larger quantity. A phase with restricted mobility was desired as this would be harder to remove and give a more stable electrolyte. The mobility of the phase cannot be determined by FT-IR. The

question of the mobility of the phase will be revisited in the discussion of ^{31}P-NMR in Section 7.1.2.

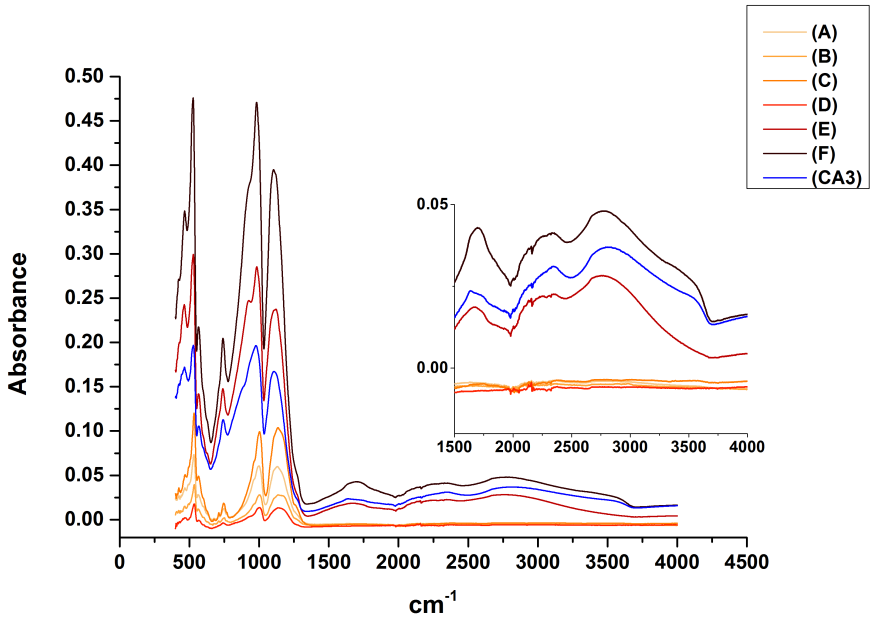

Figure 7.1: FT-IR spectra of the synthesised $Sn_{0.9}In_{0.1}P_2O_7$ compounds. The presence of a broad O-H band between 1400 cm^{-1} and 3600 cm^{-1} was highly dependant on the synthesis procedure. The synthesis conditions are detained in Table 5.1 in Section 5.1.4.

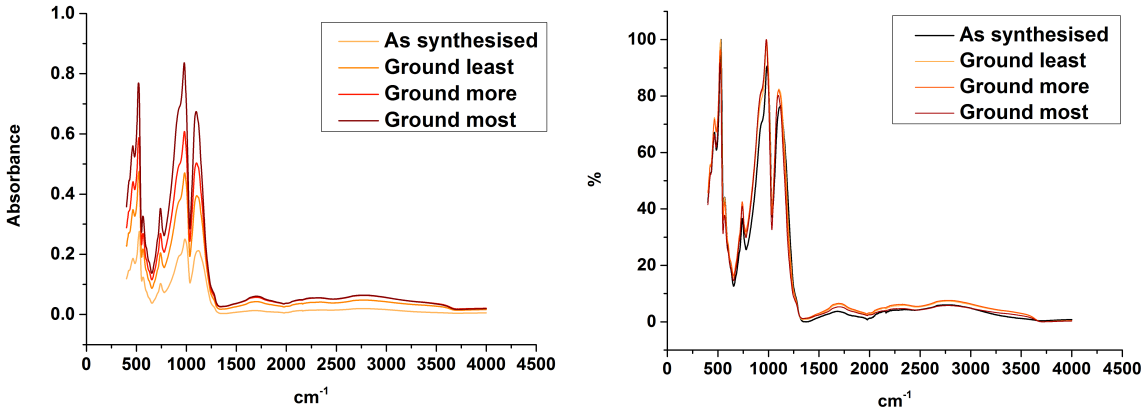

Figure 7.2: Comparison of FT-IR spectra for a single material (sample F) after progressive amounts of grinding. (a) Shows the data presented as collected and (b) shows the data normalised to the highest peak.

The phosphate peaks located at 530 cm^{-1}, 970 cm^{-1} and 1100 cm^{-1} were affected by the synthesis route as well. This effect was most likely a particle size effect. The FT-IR

response is dependant on the surface area of a material actually in contact with sampling surface and a variation in particle size between samples may change this factor. This effect was investigated by grinding a sample progressively more and more. It was seen (Figure 7.2(a)) that grinding of the material has a pronounced effect on the FT-IR spectrum. Deagglomeration of the as synthesised or lightly ground particles gave a larger O-H bond. There was no net gain from the grinding, as can be seen on Figure 7.2(b). The effect seen in Figure 7.2(a) is one of smaller particles, more particle surface in contact with the diamond of the IR spectrometer and ease of data collection. This does not mean that this is not a real and important effect. This increased surface area gives increased access to the amorphous phase of the material which in turn raises the effective conductivity. This does mean that care must be taken when comparing samples. All samples had to be finely ground to eliminate discrepancies caused by degree of agglomeration of the as synthesised material.

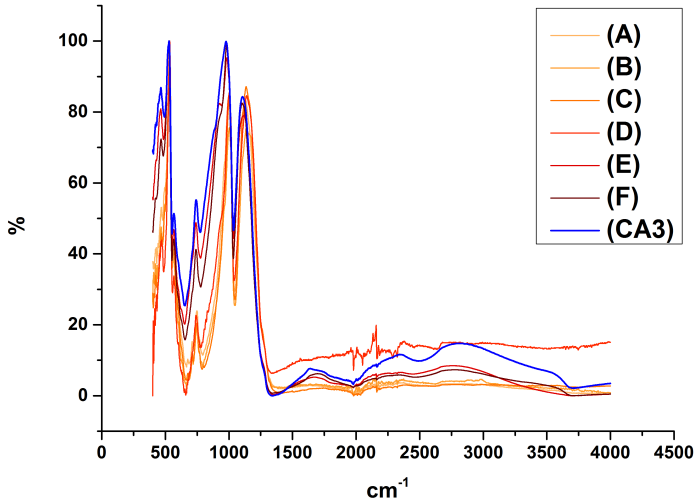

Figure 7.3: Normalised FT-IR spectra of the synthesised compounds. This allows for more direct comparison and it is seen that samples E and F should have the best conductivity.

Doing the same normalisation for all samples synthesised gave a more correct comparison of the synthesised materials (Figure 7.3). $Sn_{0.9}In_{0.1}P_2O_7$ sample (D) showed a strange O-H band. This was believed to be a magnification of the background and not an actual O-H band. Therefore sample (D) was not considered in the following. None of the synthesised materials showed as strong a signal as (CA3). Apart from sample (CA3) samples (E) and (F) showed the largest relative O-H bands. These materials were both synthesised with a direct ramp of temperature set to reach 280 °C and both were stopped at 278 °C. The materials tested electrochemically in this work were either (CA3) or materials synthesised by same route as samples (E) and (F).

Figure 7.4 shows a comparison of the additional $Sn_{0.9}In_{0.1}P_2O_7$ samples (G) and (H). These were used for cell tests when batch (F) was depleted. The IR response of batch (G) was much closer to the level of batch (F) than batch (H). This latter batch showed a broad enough O-H band to be expected to work as a electrolyte but it must be expected that batch (G) is much better. The data is normalised to the highest peak making comparison

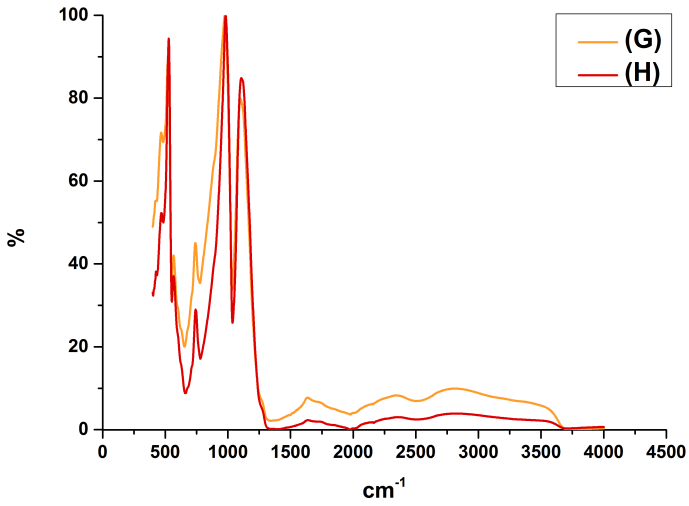

Figure 7.4: Comparison of the additional batches (G) and (H) normalised to highest peak

Table 7.1: Sample temperature and time for $Sn_{0.9}In_{0.1}P_2O_7$ synthesis

	Sample number				
Temperature	**1**	**2**	**3**	**4**	**5**
230 °C	20 h	20h 40 min	24 h 40 min	25 h 40 min	-
270 °C	10 min	20 min	30 min	1 h	1 h 30 min
300 °C	5 min	10 min	15 min	30 min	1 h

more directly possible.

A more systematised investigation of the effect of slurry forming temperature on the $Sn_{0.9}In_{0.1}P_2O_7$ synthesis product was carried out. Samples were prepared by the synthesis procedure described in Section 5.1.4 with the exception of a variation over the slurry forming temperature. When the desired temperature was reached the mixture was left at that temperature and samples were taken at specified intervals. These intervals are listed in Table 7.1. The extracted samples were then heat treated at 650 °C as per usual. Samples before and after this final step were evaluated by IR spectroscopy.

For all samples not yet heat treated in the furnace a broad band was seen from 1500 cm^{-1} to 3800 cm^{-1} indicating the presence of O-H groups or adsorbed H-O-H (additional spectra are supplied in Appendix A.3). In this case the signal comes from phosphoric acid not incorporated into the structure of the pyrophosphate. This band was even seen for samples left for more than a day at 230 °C. A difference arose between the samples after high temperature heat treatment. Here the samples collected at 230 °C and 300 °C showed no or little sign of this band, as seen in Figure 7.5. This result was independent of slurry formation time. Samples pre treated at 270 °C did however show this band strongly. The sample in Figure 7.5 was left to dwell at 270 °C for 10 min. The PO-H band was strongly seen for all dwelling times. A lessening of the band was seen for 1 h 30 min (not shown). In practice this is inconsequential as it appears that 270 °C allows for a synthesis that is not reliant on sudden termination, a vast improvement over the previously used method. A sample batch may be heated to 270 °C and allowed to dwell for a number of minutes

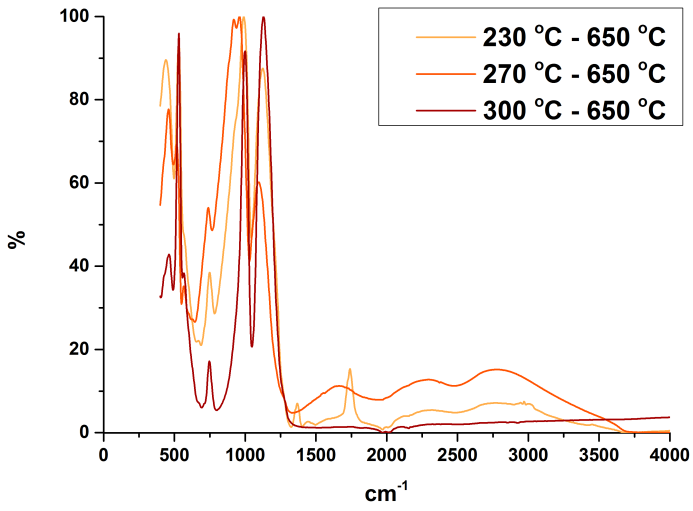

Figure 7.5: The effect of slurry formation temperature of $Sn_{0.9}In_{0.1}P_2O_7$. The broad IR band from 1500 cm^{-1} to 3800 cm^{-1} is most prominent at 270 °C indicating a more conductive material. The data is normalised to the highest peak.

after the ramping temperature has been reached without loss of the desired properties. This would allow for a uniformity between batches not previously seen and a more direct comparison between measurements for $Sn_{0.9}In_{0.1}P_2O_7$ made by different authors.
These results came too late to be acted on. Conductivity measurements and a cell test of this material would be desirable to verify that the material has the expected conductivity and stability. Should this be the case it would be sensible to make this new synthesis the standard for ease of comparison.

7.1.2 ^{31}P NMR of $Sn_{0.9}In_{0.1}P_2O_7$

The following measurement was done by Daniel Risskov Sørensen from SDU. The measurements were done in the framework of the MEDLYS project.
Solid state ^{31}P NMR was found to be very useful in the evaluation of synthesised samples when coupled with FT-IR. The solid state ^{31}P NMR made it possible to distinguish between mobile H_3PO_4 and a phase of restricted mobility. This is illustrated in Figure 7.6 for a sample showing a large O-H band (sample F). The signal at δ (^{31}P) = -38 ppm has been seen to stem from the metal pyrophosphate.[79] At δ (^{31}P) = 0 ppm a broad signal was seen. The placement of the signal corresponds to phosphoric acid.[144] Mobile orthophosphoric acid should give a very sharp peek.[145] The broadness of the peek shown here indicates an orthophosphate phase of restricted mobility.[79] This phase would be expected to be stable as it is condensed. This condensation of the phase would explain why this phase would not be removed by simple washing in water at room temperature.[75]
The immobilisation of the phosphoric acid answered the question of why these materials could function at temperatures above the boiling point of phosphoric acid (158 °C). If the phosphoric acid phase present in the samples had been a mobile phase it would evaporate fast at operation temperatures of 200 °C and above. The pyrophosphate samples were thus

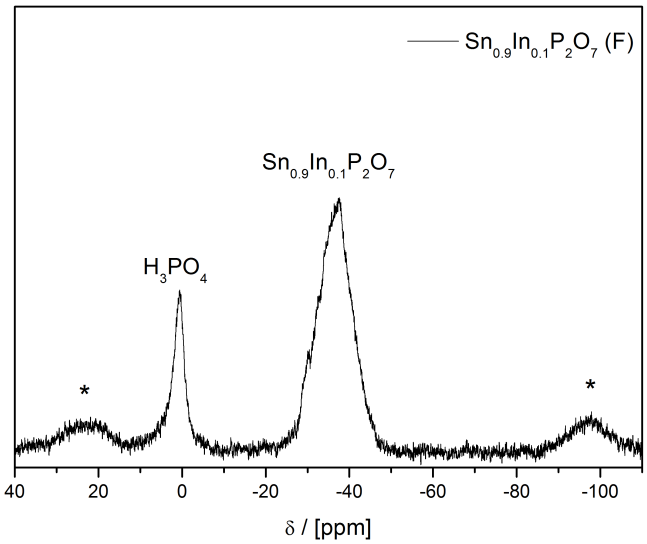

Figure 7.6: P^{31} NMR spectrum of $Sn_{0.9}In_{0.1}P_2O_7$. The response at 0 ppm stems from an phosphoric acid phase of restricted mobility.

seen to be more than a matrix for phosphoric acid. Phosphoric acid in such a matrix would still be mobile enough to evaporate at these elevated temperatures.
Stopping the first heat treatment step in the synthesis at the point where the viscous paste was formed thus created conditions that allowed for the formation of this condensed phosphoric acid phase after the second heat treatment. This condensed phase was mobile enough to allow for proton conduction but not so mobile that it was lost quickly during operation, as will be discussed further below.

7.1.3 SEM

The morphology of the synthesised materials was visualised using SEM imaging. A sample heated to 285 °C in increments of 50 °C is depicted in Figure 7.7(a) (sample (A)). The structure of this material was found to be flaky with a wide range of size of the individual flakes. No phases were seen in between the agglomerated particles. In contrast, samples heated directly to a given temperature and stopped when a viscous slurry was formed showed smaller particles with a smaller range of sizes (Figure 7.7(b)) (sample (E)). A phase of darker color in between the particles glued the sample together. The sample was interpreted as having had less time for crystal growth giving smaller particles. The dark phase was explained as the amorphous phase not only being present in grain boundaries but being so plentiful as to form agglomerates with the crystalline particles. This bountiful amorphous phase corresponded well with the IR, NMR and conductivity results (see Section 7.2). It was concluded the large presence of this phase was the reason for the difference of the two samples as seen in IR.

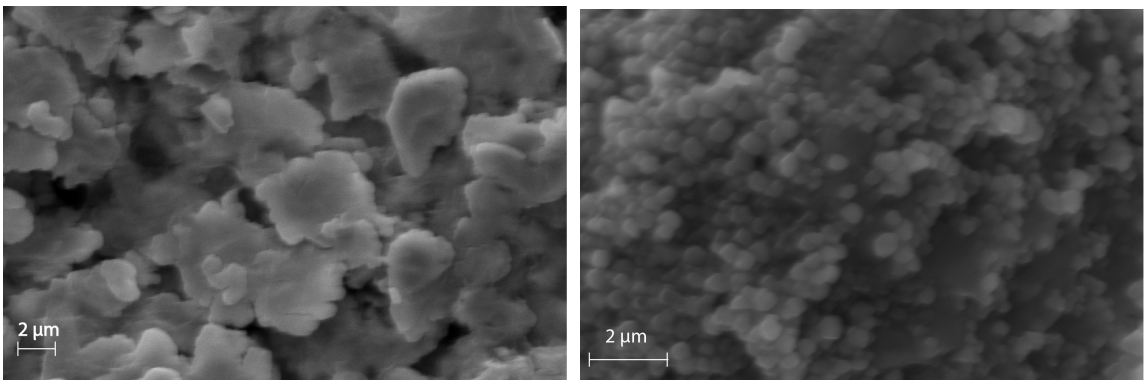

(a) (b)

Figure 7.7: The difference in morphology of $Sn_{0.9}In_{0.1}P_2O_7$ depending on preparation method. (a) shows a sample heated to 285 °C in increments of 50 °C with its resulting flaky structure. (b) shows the rounder particles resulting from a direct ramp to 280 °C and the amorphous phase in between these particles.

7.1.4 Inductively coupled plasma mass spectrometry

Table 7.2: The different dissolution attempts for ICP-MS

Treatment #	reagent	Temperature (°C)	Pressure (Bar)
1	HCl	145	ambient
2	HCl + HNO_3 (aqua regis)	60	ambient
3	HCl + HNO_3 + HF	140	40
4	HCl (37 %) + HF (40 %)	80	ambient
5	HCl + HNO_3 (1:1)	60	ambient
6	HCl (37 %) + HF (40 %) + $Zn_{(s)}$	80	ambient
7	$LiBO_3$	800	ambient

As mentioned in the beginning of this chapter the material investigated was nominally of the composition $Sn_{0.9}In_{0.1}P_2O_7$ (see Section 5.1.4) and it has throughout this work be denominated as such. This may not be the full truth however.
In an attempt to verify the structure inductively coupled plasma mass spectrometry (ICP-MS) was applied. ICP-MS was to be done on an as synthesised sample of $Sn_{0.9}In_{0.1}P_2O_7$ with large FT-IR O-H bonds as well as a boiled sample. The boiling should remove the amorphous phase present in the sample. The difference in atomic abundance between the two samples should give an answer as to how much indium was incorporated into the structure of the material and how much was in the amorphous phase. Unfortunately the sample turned out to be impossible to prepare for ICP-MS. Dissolution in a medium is a necessity for the analysis. A $Sn_{0.9}In_{0.1}P_2O_7$ sample was attempted dissolved in a variety of reagents and under a variety of conditions (see Table 7.2). Nothing worked. This was quite remarkable. Thus the actual composition of the synthesised product was not determined. In keeping with common practice seen in the literature the material was named based on the nominal composition even though this may not be correct.

7.2 Conductivity of pyrophosphates

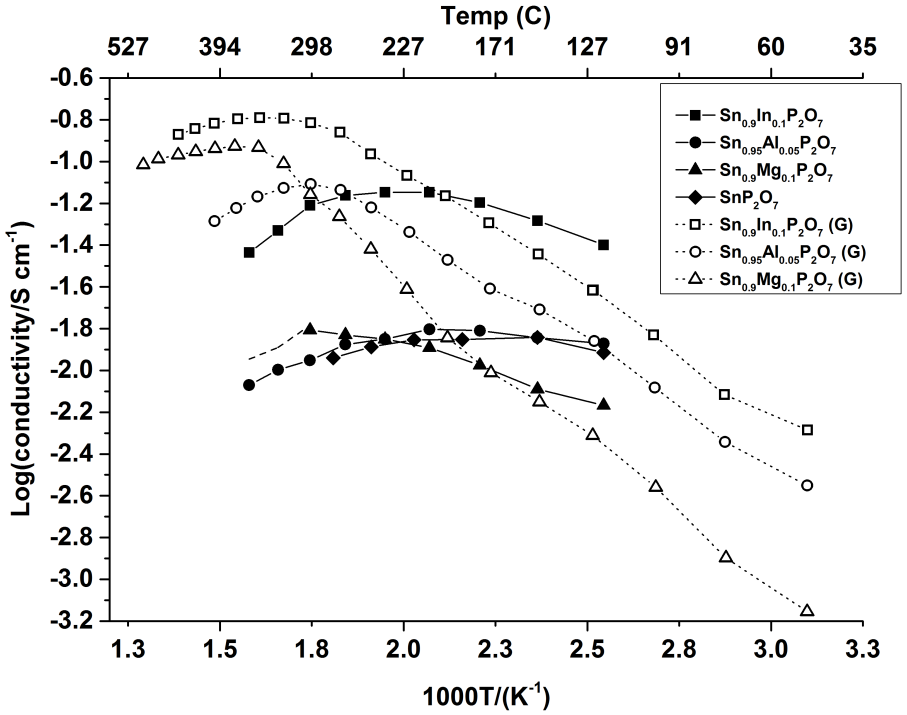

Figure 7.8: Comparrison of conductivty of In^{3+}, Al^{3+} and Mg^{2+} doped SnP_2O_7. Results marked (G) are redrawn from Genzaki et al.[82] In house results were obtained with p_{H_2O}=0.155 atm and results marked (G) at p_{H_2O}=0.0075 atm

Conductivity was measured for samples of SnP_2O_7, $Sn_{0.9}In_{0.1}P_2O_7$, $Sn_{0.95}Al_{0.05}P_2O_7$ and $Sn_{0.9}Mg_{0.1}P_2O_7$. These compositions were chosen as they have been reported to have the highest conductivities.[82,88] The Mg^{2+} and Al^{3+} doped materials were of special interest as they should be less acidic and cheaper compared to the In^{3+} doped material but still show high conductivity. The conductivity measurements presented here were obtained in the manner described in Section 6.3.

Figure 7.8 shows the results of these measurements as well as the results reported by Genzaki and coworkers.[82] The indium doped material shows the highest conductivity in both studies. At 210 °C a conductivity of $7.29 \cdot 10^{-2}$ S·cm^{-1} was measured. At low temperatures $Sn_{0.95}Al_{0.05}P_2O_7$ showed higher conductivity than $Sn_{0.9}Mg_{0.1}P_2O_7$ but both studies showed the latter surpassing the former at higher temperature. Contrary to our measurements Genzaki's results did not have a conductivity maximum centred at 210 °C. This maximum has been reported in multiple studies[65,75] and it was puzzling that it was shifted as high as 380 °C.

In Figure 7.8 $Sn_{0.9}Mg_{0.1}P_2O_7$ appeared to have no conductivity maximum. This was a result of the measurement being stopped at 300 °C. Additional measurements (shown as a dashed line) determined that the conductivity decreased after 300 °C.

Comparing to pure SnP_2O_7 almost no conductivity seemed to be gained by the doping with Al^{3+} and Mg^{2+}. The exception was in the case of $Sn_{0.9}Mg_{0.1}P_2O_7$ above 250 °C. Here

the material showed a slightly elevated conductivity. Compared to the indium doped pyrophosphate no gain was seen at all. If a gain is to be obtained it must be in the form of a reduced surface acidity allowing for the use of materials sensitive to the acidity. This reduced surface acidity of the grains is however not likely to make a marked difference. If the electrolyte is to be conductive it must retain a conducting amorphous orthophosphoric phase which would loose none of its acidity. This corrosive phase would have to be in contact with the sensitive materials and nothing would be gained.

7.2.1 Thermal cycling of $Sn_{0.9}In_{0.1}P_2O_7$

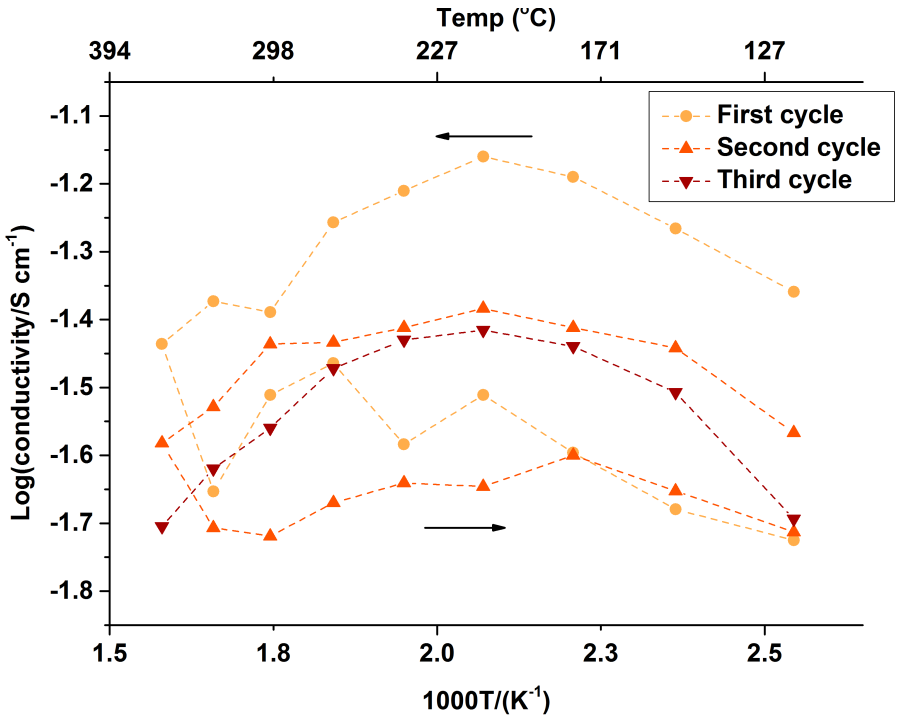

Figure 7.9: The effect on thermal cycling on the conductivity of $Sn_{0.9}In_{0.1}P_2O_7$. Conductivity was measured at p_{H_2O}=0.15 atm.

To evaluate the thermal stability of $Sn_{0.9}In_{0.1}P_2O_7$ a thermal cycling experiment was carried out. Three cycles of conductivity measurements from 120 °C to 360 °C were conducted (Figure 7.9). The third cycle was measured for rising temperature only. Between the first and second cycle the cell was rested for 30 minutes and between the second and third cycle the cell was rested for 5 minutes.
Higher conductivities were seen for ascending temperatures than for descending temperatures. The conductivity decreased from cycle to cycle with a large drop from the first to the second cycle and a smaller from the second to the third. This could indicate a stabilisation of the conductivity. More cycles would be needed for verification of this speculation. From first to second cycle some of the lost conductivity was regained. No such regeneration was seen from the second to the third cycle.

A loss of conductivity is seen over time and temperature. The amorphous phosphoric acid

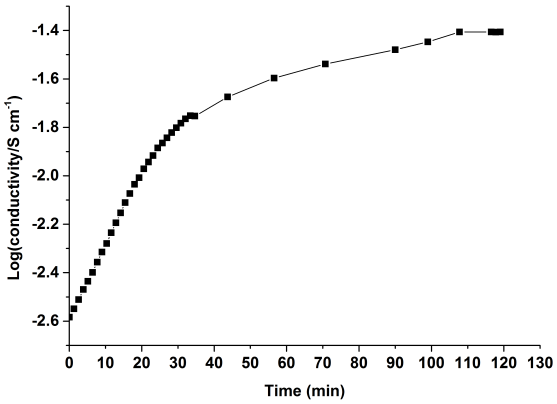

Figure 7.10: Effect of humidification (p_{H_2O}=0.15 atm) on a sample thermally cycled in unhumidified air. Temperature was 120 °C.

phase may be dehydrating forming polymerised phosphoric acid species thus limiting the conductivity. Thermal cycling in unhumidified air (not shown) gives a larger loss of conductivity than seen for humidified air. Allowed to rest at 120 °C and p_{H_2O}=0.15 atm for 120 min such a sample regained all of the lost conductivity, as seen in Figure 7.10. This support the notion of a (partially) reversible polymerisation of the amorphous species. It also explains why a regeneration of conductivity was seen between the first two cycles where the cell was left for 30 min but not seen between the last two where the cell was left for 5 min. It is not sure that the rehydrated phosphoric acid species was in the same less mobile form as before polymerisation and it may have become more volatile as a result. Experiments previously done in our group showed that simply adding H_3PO_4 to $Sn_{0.9}In_{0.1}P_2O_7$ and heat treating it at 650 °C gave a thermally much more unstable product. Initial conductivity was high but it lost conductivity fast. The same may have been true for the rehydrated samples. This may ultimately be the reason for the conductivity loss over each cycle. The polymerisation may end up being irreversible or so slowly regenerating that it makes no practical difference.
The relationship between conductivity, time and temperature will be returned to in Section 9.1.

7.3 Electrolysis with $Sn_{0.9}In_{0.1}P_2O_7$

Electrochemical experiments were done with $Sn_{0.9}In_{0.1}P_2O_7$ as electrolyte. The materials tested were either (CA3) or materials synthesised by the same method as material (F). The general characteristics of the cells can be found in Table 7.3. The specific characteristics of the cells will be presented in the relevant sections. When it is stated that 1 Ta coated flow plate is used it is for the anode side. In such cases an uncoated stainless steel flow plate was used for the cathode side.

Table 7.3: Components and loadings of $Sn_{0.9}In_{0.1}P_2O_7$ electrolyser cells. E., A. and C. denotes electrolyte, anode and cathode respectively.

Cell #	E. batch	E. mass	E. thickness	A. loading	A. felt type	C. loading
SnInP-2xS	CA3	0.5052 g	0.65 mm	2.86 mg/cm ^{2}	1	7.11 mg/cm^2
SnInP-1xS	CA3	0.5055 g	0.60 mm	4.22 mg/cm ^{2}	1	11.46 mg/cm^2
SnInP-Imp	F	0.5166 g	0.65 mm	3.75 mg/cm ^{2}	1	11.46 mg/cm^2
SnInP-Ref	J	0.5052 g	0.64 mm	2.33 mg/cm ^{2}	2	8.86 mg/cm^2
SnInP-HC	F	0.7191 g	0.90 mm	3.23 mg/cm ^{2}	1	11.46 mg/cm^2
SnInP-Temp1	CA3	0.5297 g	0.60 mm	4.75 mg/cm ^{2}	1	7.11 mg/cm^2
SnInP-Temp2	G	0.5169 g	0.64 mm	2.41 mg/cm ^{2}	2	8.86 mg/cm^2

7.3.1 Steam on both electrodes

Table 7.4: Conditions for testing of a $Sn_{0.9}In_{0.1}P_2O_7$ cell with steam on both electrodes.

Cell #	Flowplates	Steam	temperature	Impedance
SnInP-2xS	1 Ta coated	2x steam	200 °C	no

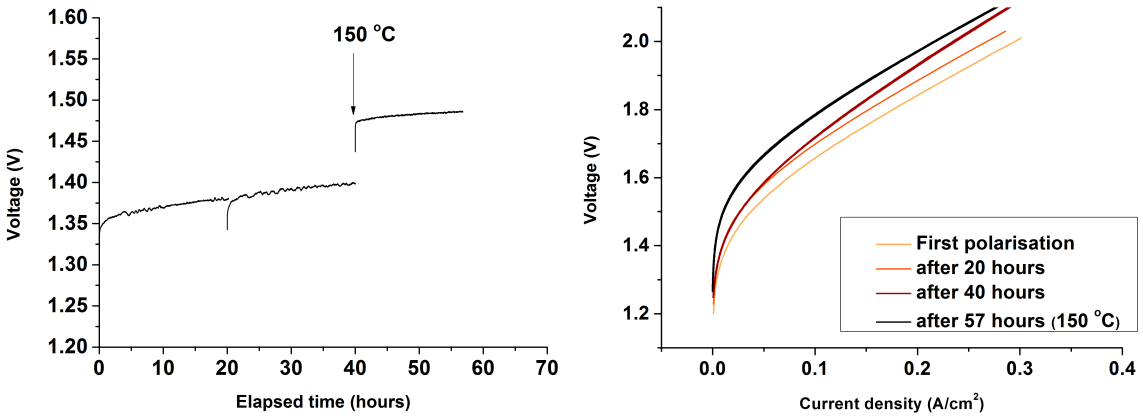

(a) (b)

Figure 7.11: (a) Voltage as a function of time at 7.5 mA/cm^2 and (b) polarisation curves for an electrolyser cell with a $Sn_{0.9}In_{0.1}P_2O_7$ electrolyte and steam on both electrodes (cell SnInP-2xS). Recorded at 200 °C with a lowering to 150 °C after 40 hours.

A cell was tested with $Sn_{0.9}In_{0.1}P_2O_7$ using the (CA3) batch of electrolyte. The cell is denoted SnInP-2xS. Steam was supplied to both electrodes under the assumption that dehydration might be detrimental to the cell. The general performance of the cell at a small current density (7.5 mA/cm^2) can be seen in Figure 7.11(a). The cell was tested for a total of 57 hours, 40 of these at 200 °C and the last 17 at 150 °.
Polarisation curves were done at 0, 20, 40 and 57 hours (Figure 7.11(b)). At first polarisation a current density of 241 mA/cm^2 was reached at 1.9 V. The cell was still operational after 57 hours.
The average degradation for the first 20 hours and second 20 hours were 1.2 mV/h and 0.9 mV/h respectively (Table 7.5). After 40 hours the temperature was lowered to 150 °C.

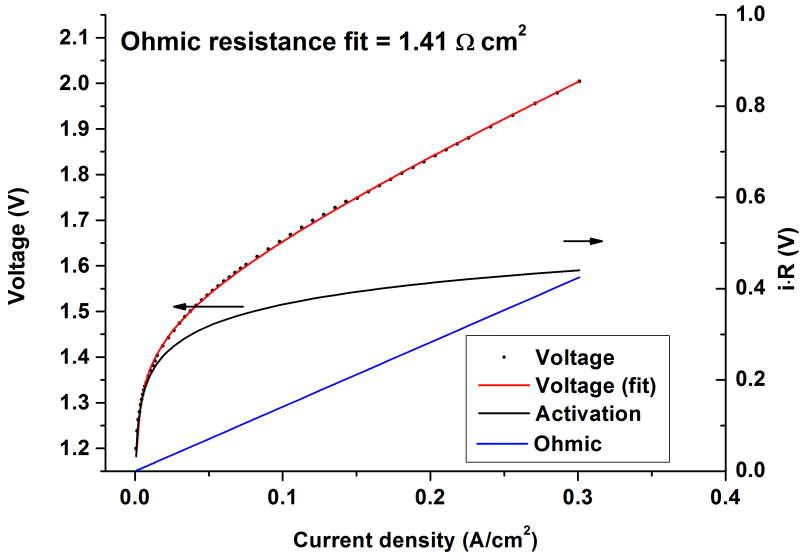

Figure 7.12: Example of a fit of a polarisation curve (cell SnInP-2xS).

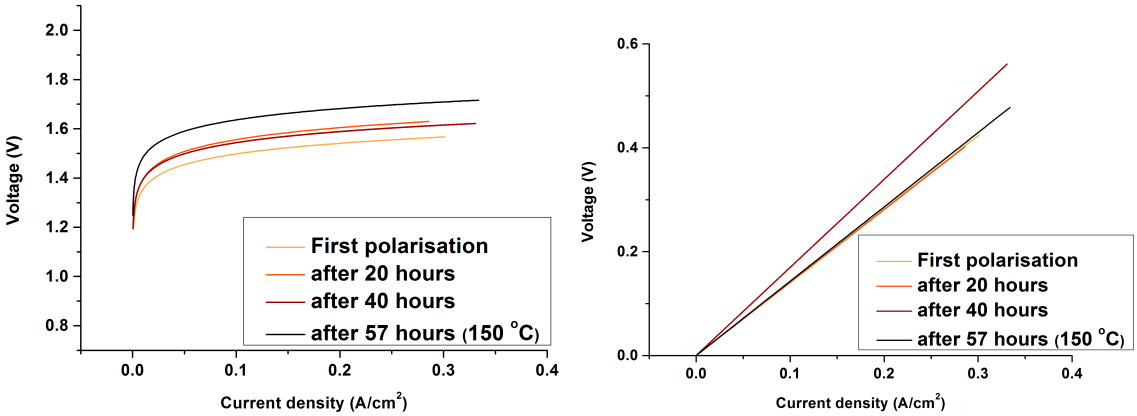

(a) (b)

Figure 7.13: Activation (a) and ohmic (b) contribution to the polarisation curves of an electrolyser cell with steam on two electrodes and a $Sn_{0.9}In_{0.1}P_2O_7$ electrolyte (cell SnInP-2xS).

This was done to see whether or not a temperature of 200 °C was a necessity for operation. As expected the performance of the cell suffered from the lowering of the temperature (Figure 7.11(a)). However, the average voltage loss over time fell to 0.5 mV/h. This indicated a thermal acceleration of the degradation of one or more of the components in the cell.

Figure 7.11(b) shows the recorded polarisation curves. Degradation over time was observed as with Figure 7.11(a). To better evaluate the polarisation curves the fitting routine described in Section 4.2.1 was used. An example of such a fit is displayed in Figure 7.12.

Table 7.5: Resistance and conductivity estimated from polarisation curves for $Sn_{0.9}In_{0.1}P_2O_7$ cells SnInP-2xS and SnInP-1xS.

Cell #	Time	R_s ($\Omega \cdot$ cm^2)	σ (S $\cdot$ cm^{-1})	Voltage loss (mV/hour)
SnInP-2xS	0 hours	1.41 ± 0.021	$4.6{\cdot}10^{-2}$ S·cm^{-1}	–
	20 hours	1.41 ± 0.015	$4.6{\cdot}10^{-2}$ S·cm^{-1}	1.2
	40 hours	1.67 ± 0.016	$3.9{\cdot}10^{-2}$ S·cm^{-1}	0.9
	57 hours (150 °C)	1.43 ± 0.009	$4.5{\cdot}10^{-2}$ S·cm^{-1}	0.5
SnInP-1xS	1.3 hours	1.47 ± 0.009	$4.1{\cdot}10^{-2}$ S·cm^{-1}	–
	3 hours	1.56 ± 0.014	$3.8{\cdot}10^{-2}$ S·cm^{-1}	–
	24 hours	1.74 ± 0.016	$3.4{\cdot}10^{-2}$ S·cm^{-1}	0.7
	48 hours	1.81 ± 0.014	$3.3{\cdot}10^{-2}$ S·cm^{-1}	0.3

Figure 7.13(a) and 7.13(b) shown the activation parts and ohmic parts of the polarisation curves respectively. The first 20 hours were the most detrimental to the electrode processes. At all current densities a higher voltage response was seen after 20 hours. In contrast to this there seemed to be next to no change in the ohmic resistance of the cell. It is therefore likely that the potential loss seen in the first 20 hours is due to electrodes and their processes. After 40 hours next to no additional activation loss was seen. On the other hand the ohmic contribution was seen to change markedly. After this measurement a leak at the cathode fitting was discovered and tightened. After an additional 17 hours at the lower temperature of 150 °C the ohmic resistance was back at the levels seen after 20 hours. This indicated that the 50 °C lowering of the temperature had little effect on the conductivity of the electrolyte and that the higher ohmic resistance seen after 40 hours was due to the leak. As steam was supplied to the cathode an overpressure could have built up giving a pressure gradient over the electrolyte. This gradient could have caused a greater degree of crossover, lowering the voltage. When the leak caused the cathode side to obtain a pressure closer to ambient pressure this effect on the potential was lost. In that sense the measurement at 40 hours could be considered closer to the actual performance of the cell than the other measurements.

The ohmic resistances calculated from the fits are shown in Table 7.5. The standard error of the fits were within $\pm$ 1.5 % which was considered excellent. The ohmic resistances for 0, 20 and 57 hours were all within the standard error of the fit. Thus there seem to be little degradation of the electrolyte. Table 7.5 also shows conductivity values calculated from the ohmic resistance with the assumption that the electrolyte is the only source of ohmic resistance. No standard error is given for these as the calculated confidence interval from the fits are not trivially recalculated to make sense for σ. These conductivities were seen to be lower than the previously measured $7.29{\cdot}10^{-2}$ S·cm^{-1}. As the electrolyte was seen to be stable over time this lower conductivity must be the result of contact resistance or a similar ohmic loss.

7.3.2 Steam on anode side only

A cell with steam on only the anode was investigated in order to evaluate the effect of steam.

The assembled cell was, apart from the steam conditions, identical to cell SnInP-2xS. It was tested for 48 hours. As for the previous cell a general loss of performance was seen with time (Figure 7.14(a)). Average degradation at 7.5 mA/cm^2 was for the first 20 hours

Table 7.6: Conditions for testing of a $Sn_{0.9}In_{0.1}P_2O_7$ cell with steam on the anode only (cell SnInP-1xS).

Cell #	Flowplates	Steam	temperature	Impedance
SnInP-1xS	1 Ta coated	steam on anode	200 °C	no

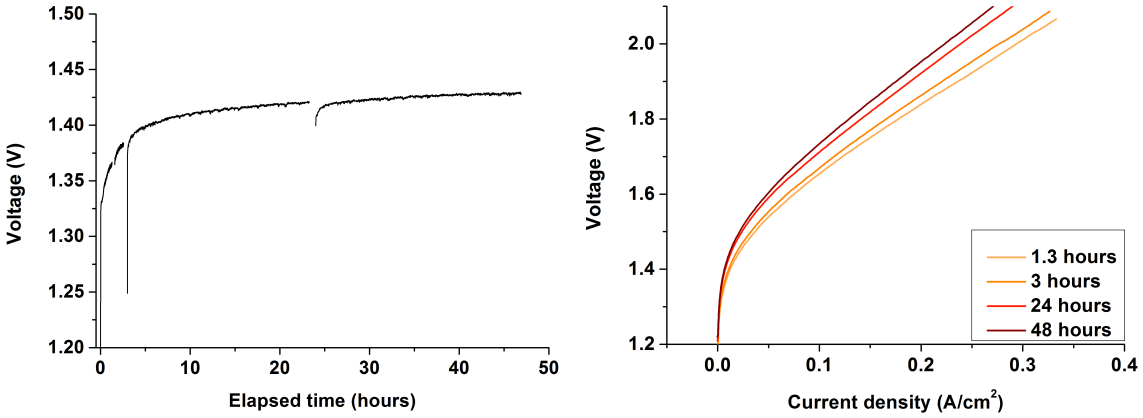

(a) (b)

Figure 7.14: (a) Voltage as a function of time at 7.5 mA/cm^2 and (b) polarisation curves for an electrolyser cell with a $Sn_{0.9}In_{0.1}P_2O_7$ electrolyte and steam on the anode only (cell SnInP-1xS).

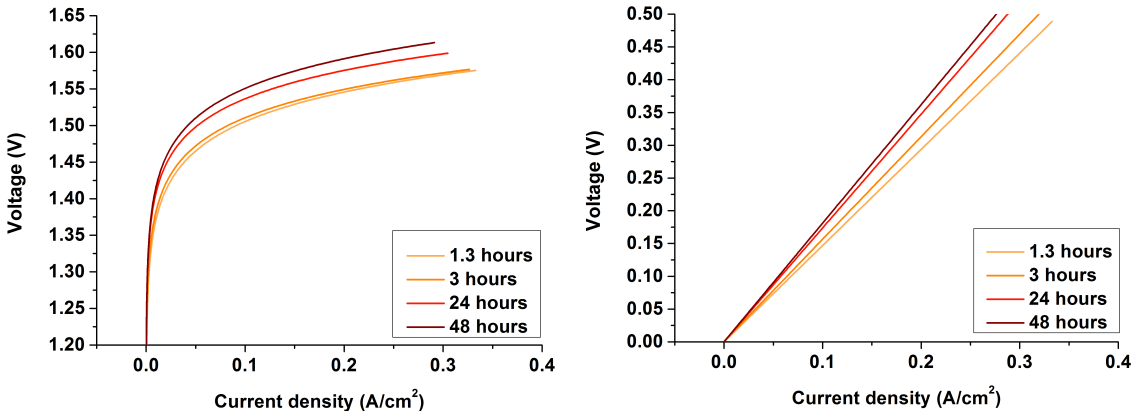

(a) (b)

Figure 7.15: Activation (a) and ohmic (b) contribution to the polarisation curves of an electrolyser cell with steam on anode only and a $Sn_{0.9}In_{0.1}P_2O_7$ electrolyte (cell SnInP-1xS).

= 0.7 mV/h and for the second 23 hours = 0.3 mV/h.
The polarisation data for this cell was treated the same way as for the previous cell. Initially a current density of 242 mA/cm^2 was achieved at 1.9 V. The activation contribution (Figure 7.15(a)) matched the long term data (Figure 7.14(a)) as a continuous degradation was seen with less loss from 24 hours to 48 hours than from 3 hours to 24 hours. The same trend held true for the ohmic contribution (Figure 7.15(b)).

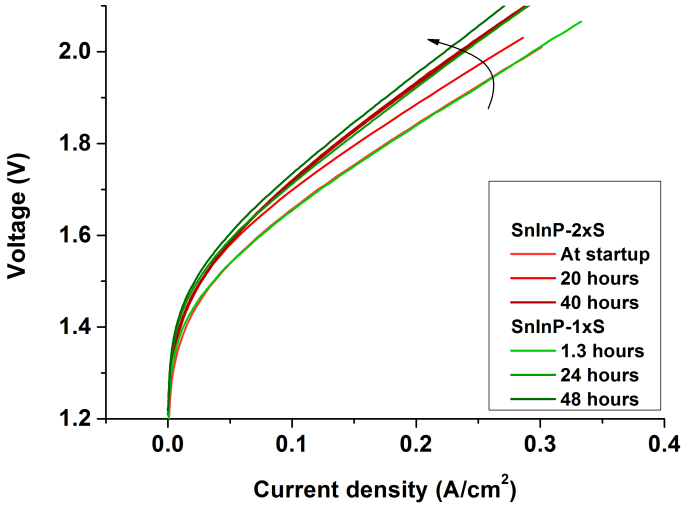

Figure 7.16: Comparison of polarisation experiments for electrolysers with (cell SnInP-2xS) and without (cell SnInP-1xS) steam on the cathode respectively.

A continuous change in resistance was seen over time (see Table 7.5). Comparing with cell SnInP-2xS (Figure 7.16) it was seen that the "abnormal" measurement for cell SnInP-2xS was in good correspondence with how this cell progressed. This appeared reasonable as this measurement had the same conditions as the SnInP-1xS cell, as no pressure difference was present.
As an ohmic loss over time was seen for the SnInP-1xS cell and no ohmic loss over time was seen for the SnInP-2xS cell it would be sensible to continue the work with steam on both electrodes. However, uncertainty of the precise nature of the ohmic contribution was present. This might not be purely electrolyte resistance as ohmic contributions from the electrode, such as contact resistance, could be responsible for the increased resistance. It was also suspected that the pressure difference between the electrodes might influence the measurements in this two atmosphere setup. Therefore it was decided to investigate further without steam on the cathode to get a better idea of the electrodes contribution to the ohmic resistance.

7.3.3 $Sn_{0.9}In_{0.1}P_2O_7$ with impedance measurements

In the following (R_s) will denote the ohmic resistance as estimated from polarisation curves, (R_e) will denote the electrolyte resistance as estimated from impedance results, (R_{p_1}) will denote polarisation resistance related to high frequency electrode processes and (R_{p_2}) polarisation resistance related to low frequency electrode processes.

Table 7.7: Test conditions of a $Sn_{0.9}In_{0.1}P_2O_7$ electrolyser cell with impedance spectroscopy evaluation.

Cell #	Flowplates	Steam	Temperature	Impedance	Amplitude
SnInP-Imp	1 Ta coated	steam on anode	200 °C	yes	50 mV

Table 7.8: Test intervals for a $Sn_{0.9}In_{0.1}P_2O_7$ electrolyser cell with impedance spectroscopy evaluation (cell SnInP-Imp).

	Day 1	**Day 2**	**Day 3-5**
Time tested	22 hours 50 min	24 hours 26 min	63 hours 3 min
Time between measurements	2 h 21 min.	2 h 25 min.	4 h 20 min.

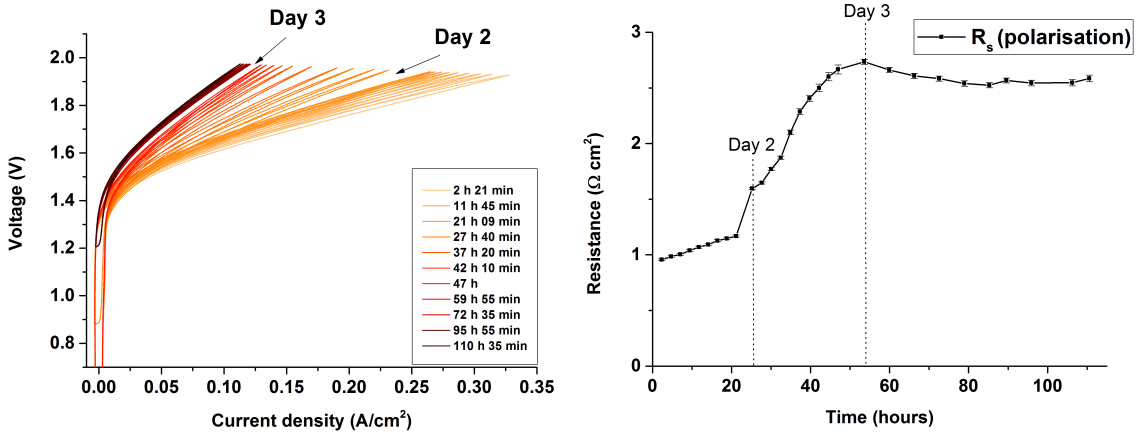

(a) (b)

Figure 7.17: (a) progression of polarisation results over time and (b) estimated ohmic resistance (R_s) from these polarisations for a $Sn_{0.9}In_{0.1}P_2O_7$ electrolyser cell with impedance spectroscopy evaluation (cell SnInP-Imp).

I order to qualify the overpotential contribution of the electrolyte and the electrodes respectively cell SnInP-Imp was tested with both polarisation curve evaluation and impedance spectroscopy. The cell was tested for 113 hours in total and its test conditions and measurement times can be seen in Table 7.7 and 7.8 respectively. After the first day of testing the cell was left at 200 °C with steam on the anode but no applied current. This was done to evaluate the effect of polarisation on the degradation of the cell in comparison to the effect of heat and steam. No such pause was taken between day 2 to day 3.
Figure 7.17(a) shows the recorded polarisation curves collected over 5 days of testing. The initial performance of the cell was 313 mA/cm^2 at 1.9 V and 200 °C. A progressively lower performance was seen over time until almost stabilisation at a very low performance, $\approx$ 90 mA/cm^2, after approximately 85 hours of testing. It was also seen that after the interlude with no applied current the cell performed worse and had a faster loss of performance. Thus voltage was clearly not the only detrimental factor. The combination of heat and steam over time was enough to affect the performance of the cell markedly. Inspection of the polarisation curves showed a rather drastic change in slope of the linear part of the curves after the hiatus indicating a change in ohmic resistance. This was backed up by Figure 7.17(b) where estimated ohmic resistance from polarisation fits were plotted as a function of time. A clear jump in R_s was seen from the end of day 1 to beginning of day 2. A faster loss of ohmic resistance during day 2 compared to day 1 was also seen from both graphs. At the end of day 2 and beginning of day 3 the ohmic resistance reached a maximum, dropped a bit and then stabilised to within standard error of the fits. Thus R_s

nearly tripled before levelling out giving the impression of a quickly degrading electrolyte.

To evaluate the quality of the impedance data Kramers-Kronig transformation (KK) was

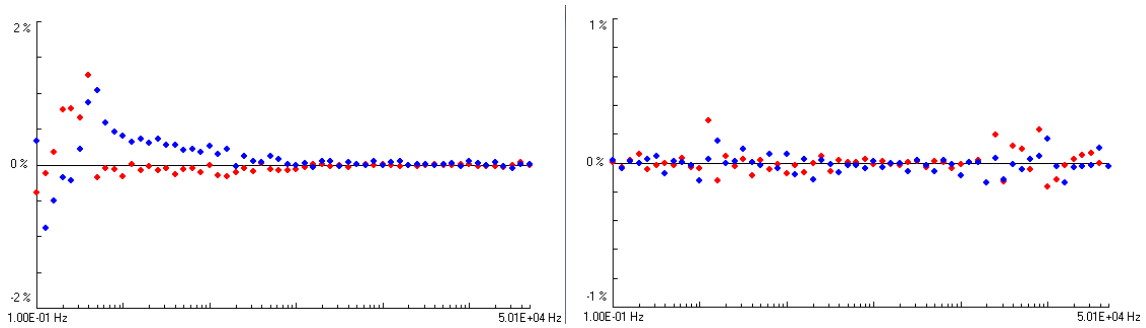

(a) (b)

Figure 7.18: Kramers-Kronig validation of impedance data for cell SnInP-Imp. Data obtained at 1.6V polarisation are shown for (a) day 1 and (b) day3 (cell SnInP-Imp)

done on a representative portion of the data (about 20 %). It was found that at the data had a somewhat high residual percentage ($\approx$ 2 %) at low frequencies. This was seen less over time especially for impedance collected at high polarisation (1.6V or 1.8V). Figures 7.18(a) and 7.18(b) shows the KK residuals for the first measurement at 1.6V for day 1 and 3 respectively. Care was taken when interpreting the data at the low frequency region. It should be noted at even at this relatively high amplitude (50 mV) no systemic problems were detected in the KK-validation at high frequencies. For some cells slightly higher residuals were seen at high frequencies but they were still below 0.5 % and without any periodical structure.

Figure 7.19(a) shows the progression of the impedance recorded at 1.6V. The impedance seen in Figure 7.19(a) supported the general conclusions from the polarisation curves. Between day one and day two there was a jump in R_s towards higher values. The two depressed semi circles grew at different paces but ended up stable and roughly equal in size. The ohmic resistance also stabilised at the beginning of day three.

The data from the impedance measurements were used to do a distribution of relaxation times (DRT) plot. Figure 7.19(b) exemplifies this for impedance measurements recorded at 1.6V. This plot corresponded well with the previously presented data. The low frequency element grew slowly during day one but after a day and a half without polarisation it began to grow faster. This supported the idea that polarisation was not the only factor in the degradation of the cell and time, steam and temperature definitely had a role in the performance loss. During day three to five the peak almost stabilised. For the high frequency element similar trends were seen except for days three to five. Here the peak shrank until a stable point was reached. This makes sense when comparing to the changes seen in the Nyquist plot. It should be noted that even though two low frequency peaks were seen for early measurements the rightmost peak was a fitting artefact. It originated from the fitting polynomial and was disregarded.

The high frequency element is most likely a collection of charge transfer processes from the two electrodes and it would be expected to change little over time. This was unfortunately not the case and indicates electrode degradation on one or both electrodes. It would be ex-

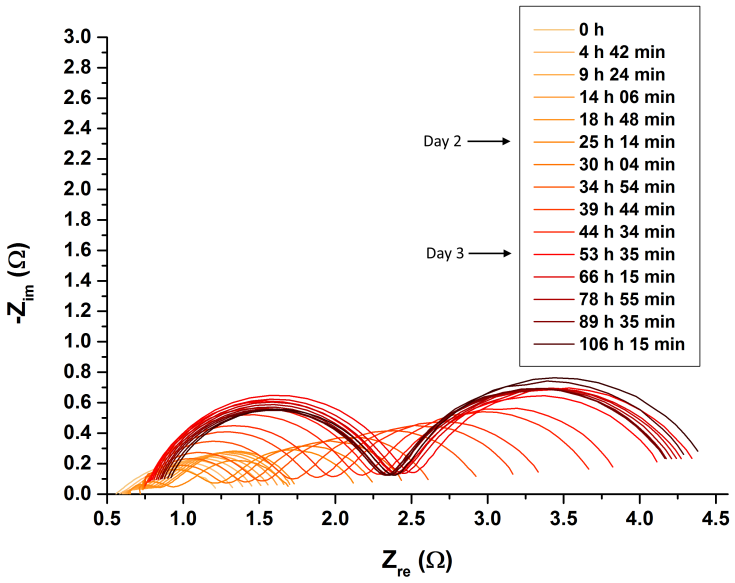

(a)

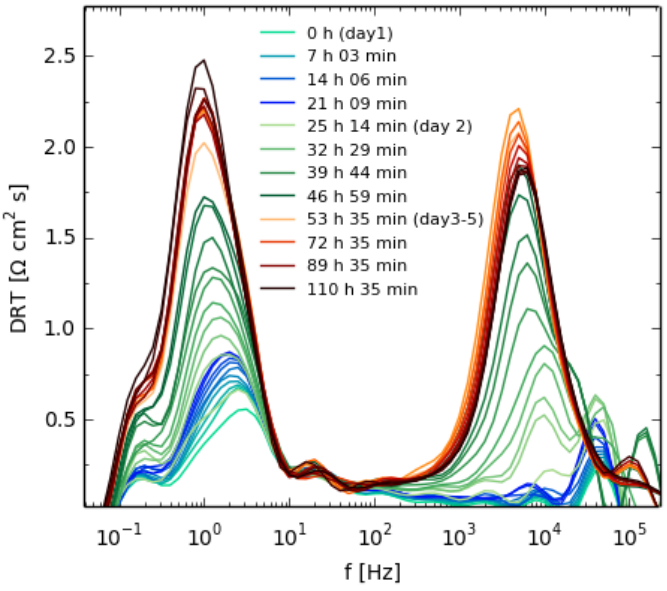

(b)

Figure 7.19: Nyquist plot (a) and DRT evaluation (b) of impedance data recorded at 1.6V. Ohmic resistance and resistance of two elements are seen to increase over time (SnInP-Imp).

pected that the anode dominates this arc as the OER is the most demanding reaction. This is not a given however and the high frequency response should not be directly equated to the anode. The faster cathode process may show up in this region if degradation begins to increase the polarisation resistance in the electrode. The low frequency at only a few Hz may be related to gas transfer in the GDL and flow plates and gas conversion in the

electrode structure. In the work of Jespersen and coworkers[146] on PEM fuel cells such features were seen at such frequencies. It may also be directly related to the sluggish oxygen evolution reaction and is certainly linked to the anode side of the cell.When current density was increased the response decreased for the low frequency impedance response. As it would be expected that the OER on the anode would be the process most directly affected by an increase in current this further points to the low frequency arc stemming mostly from the anode.

CNLS fitting was employed to estimate the electrolyte resistance (R_e), the high frequency

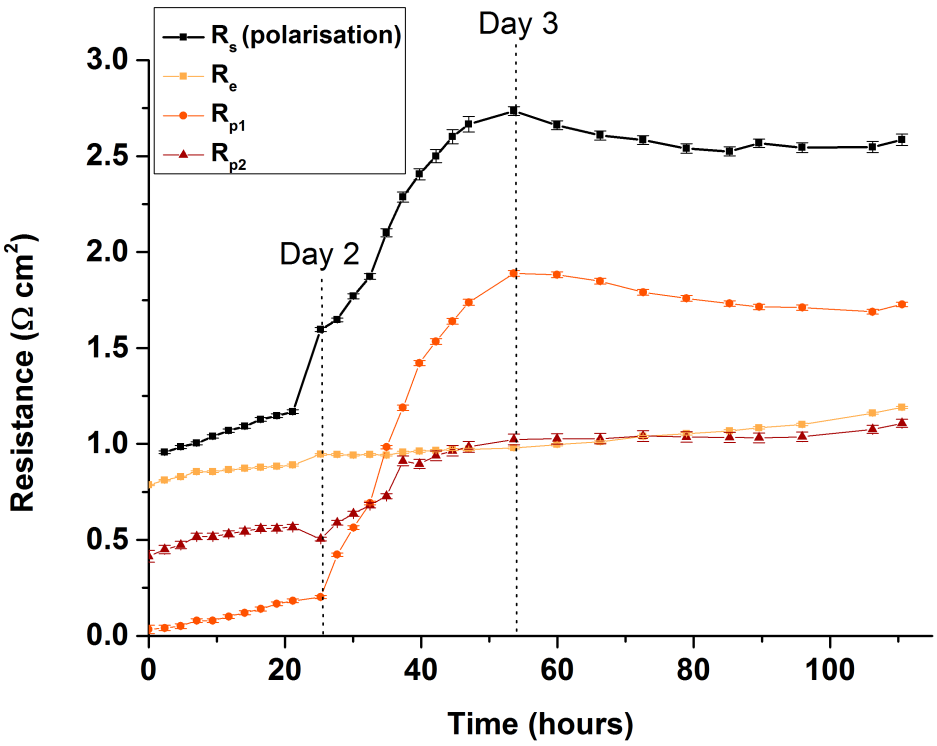

Figure 7.20: Electrolyte and polarisation resistance estimated from impedance, recorded at 1.8 V, by CNLS fitting as well as ohmic resistance estimated from polarisation curves as a function of time (cell SnInP-Imp).

polarisation resistance (R_{p_1}) and the low frequency polarisation resistance (R_{p_2}). At low or no voltage (1.2V and OCV) no actual electrolysis was happening. This made it practically impossible to estimate the polarisation resistances from the spectra recorded at these voltages. It was attempted to estimate R_e from the data at OCV and 1.2V. While it is possible to do so the results varied widely in an unsystematic way. These estimations were disregarded. For data recorded at a potential of 1.4V and above it was possible to fit the spectra. Figure 7.20 shows the resulting resistances calculated CNLS fit for 1.8V. It was seen that after the cell had been left without current for 1.5 days the electrode degradation picked up until it stopped during day 3. This was true for both elements but R_{p_1} clearly increases the most. At the first day 2 measurement R_{p_2} dropped a bit compared to before

the hiatus but increase form there. It stabilised before R_{p_1} did. R_e increased at a steady pace throughout the entire measurement range. A small jump was seen from day 1 to day 2. It should be noted that R_e from the fits at 1.8 V, 1.6 V and 1.4 V all are within the standard error of fit of each other and are thus not affected by polarisation. This fits with what was expected of the electrolyte resistance.
R_s from the polarisation curves was also included in Figure 7.20 to allow for a comparison with R_{p_1}. The two follow a similar pattern especially from day two and onward. The same systematic trends were seen for impedance data recorded at 1.6V and 1.4V. This result could mean two things. Either the ohmic resistances estimated by the polarisation includes an ohmic resistance from the electrodes and is not a true measure of the electrolyte resistance or the polarisation resistance estimated from the impedance actually includes a part of the electrolyte resistance. If the latter was true then all big changes in electrolyte resistance would be seen in the estimated polarisation resistance. This is not the case as for the first measurement in day 2 R_s jumps to a much higher value while R_{p_1} does not jump until the measurement 8 hours later. It is thus more likely that the polarisation curve fit does not manage to split the contributions up entirely correctly and R_s should not automatically be equated to the electrolyte resistance R_e. So while the electrolyte certainly degraded with time degradation in the electrodes made the electrolyte degradation seem worse than it was.
As the degradation of the electrodes clearly picked up during day 2 it seemed likely that one of the electrodes had in some way been destabilised during the gap between day 1 and day 2 and renewed polarisation of the cell accelerated a degradation of a vulnerable electrode. Visual inspection of the flow plates after the experiment revealed a cathode adhering strongly to the stainless steel flow plate. The carbon GDL was pressed into the flow channels as well. This degradation of the GDL could be the reason for the increase in one or both of the electrode elements from the fittings. As R_{p_1}, which is related to fast electrode processes, showed the largest degradation this indicates a connection between the cathode and R_{p_1}. The anode was seen to be pressed into the electrolyte. This could have lead to harder access for the steam to the IrO_2. Other possible reasons for anode degradation include IrO_2 being lost from the Ta coated SS or particle sintering.
Recalculation of the ohmic resistance estimated from impedance to conductivity gives values starting as high as $6.6{\cdot}10^{-2}$ S·cm^{-1} and with a minimum of $4.2{\cdot}10^{-2}$ S·cm^{-1}. The conductivity measured at 210 °C was $7.3{\cdot}10^{-2}$ S·cm^{-1}. Thus the conductivity estimated by the impedance is close to that previously measured and the difference may partly be caused by the difference in measurement temperature. As the electrolyte conductivity estimated from the cell test is so close to the measured conductivity it can be assumed that a thinner electrolyte would be very beneficial for the cell.

7.3.4 $Sn_{0.9}In_{0.1}P_2O_7$ with reference measurements

Table 7.9: Test conditions for a $Sn_{0.9}In_{0.1}P_2O_7$ electrolyser cell with reference electrode.

Cell #	Flowplates	Steam	temperature	Impedance	Amplitude	Reference
SnInP-Ref	1 Ta coated	steam on anode	200 °C	yes	10 mV	Pt/H_2

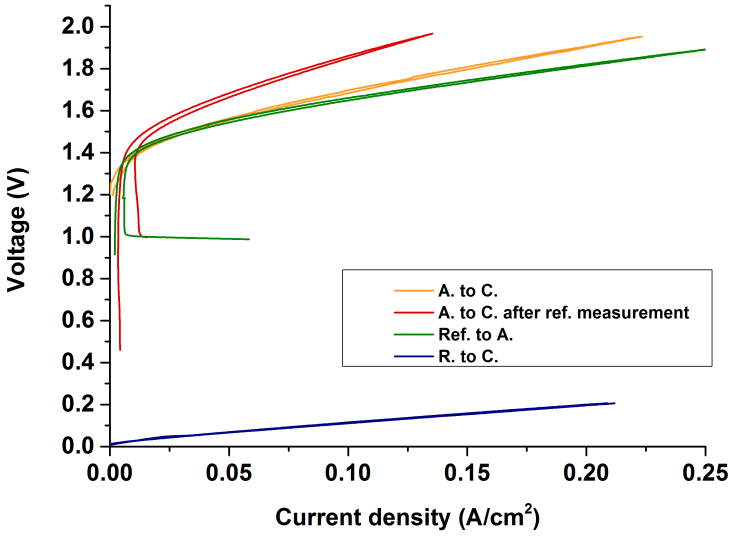

(a)

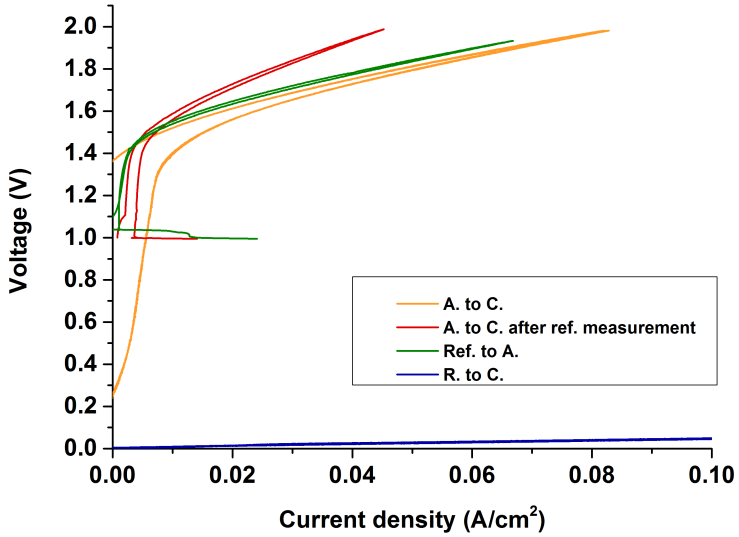

(b)

Figure 7.21: Reference electrode measurements at the beginning (a) and end (b) of 18 hours of testing. A., C. and Ref. denotes anode, cathode and reference respectively (cell SnInP-Ref). The reference electrode measurements seem to degrade the cell.

As impedance does not (necessarily) allow for a direct separation of the overpotential contributions from the two electrodes reference electrodes must be used for this task. In an attempt to distinguish the two electrodes in a $Sn_{0.9}In_{0.1}P_2O_7$ cell similar to cell SnInP-Imp from each other a platinum wire reference electrode was introduced (see Section 4.2.2). Figure 7.21(a) and Figure 7.21(b) depicts the efforts of reference electrode measurement for cell SnInP-Ref. Polarisation curves were done before and after the reference measurements and all measurements were done with a H_2 flow of 2.01 L/hour on the cathode. Between the two measurements the cell was tested for 18 hours with polarisation and impedance

measurements every 4 hours and 30 minutes. The results have not been corrected for electrolyte resistance contribution.
It was seen that in both cases the polarisation curves are not the same before and after the reference electrode measurements. For the second reference electrode measurement (Figure 7.21(b)) the reference to anode measurement was even higher than polarisation curve. While it was clear that some part of the reference measurement process was harmful to the cell the exact reason for the detriment was unclear. Between the two reference measurements polarisation curves were recorded 4 times. A comparatively small degradation was observed over these polarisations indicating that it was not the mere act of polarising the cell that causes this large degradation. It should be mentioned that the uncorrected cathode overpotential contribution was measured as 111 mV at 100 mA/cm^2 at first measurement and 49 mV at 100 mA/cm^2 at the second. It also seems unlikely for the cathode to increase in performance over time.

Figure 7.22 shows the estimated ohmic and polarisation resistances from impedance

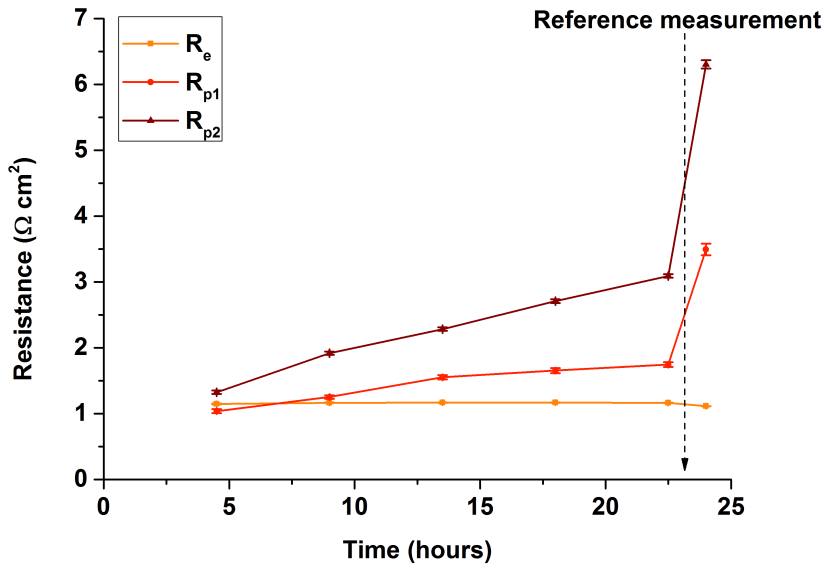

Figure 7.22: Electrolyte and polarisation resistance estimated from impedance by CNLS fitting as well as ohmic resistance estimated from polarisation curves as a function of time (cell SnInP-Ref).

CNLS fitting. All standard errors for the resistances were below 2 %. The ohmic resistance measured from impedance does not increase, on the contrary it decreases a bit. The polarisation resistances were seen to increase over time with a sharp spike after the second reference electrode measurement showing its detrimental effect on the electrodes.
Similar reference electrode measurements suffered from worse loss of performance after reference measurements. Fluctuations in the steam supply was also found to interfere drastically with the measured overpotentials. For these reasons the reference electrode was abandoned. While the rewards of having a functional reference electrode were compelling it was found that too much time would be required to get to that point. Apart

from a single experiment with WC as cathode electrocatalyst, see Section 9.2.1, no further attempts were made.

7.3.5 The effects of temperature

Table 7.10: Test conditions for $Sn_{0.9}In_{0.1}P_2O_7$ electrolyser cells with variation of temperature.

Cell #	Flowplates	Steam	temperature	Incriment	Impedance	Amplitude
SnInP-Temp1	1 Ta coated	steam on anode	200 - 240 °C	20 °C	no	–
SnInP-Temp2	2 Ta coated	steam on anode	200 - 250 °C	10 °C	yes	10 mV

As it had been established that atleast the electrode(s) and possibly also the electrolyte was not entirely stable over time it was decided to investigate the effect of temperature. Two experiments were done: one solely with polarisation evaluation and one with impedance evaluation as well. For the first experiment the temperature was raised in increments of 20 °C and for the second in increments of 10 °C.
Figure 7.23(a) shows the polarisation curves recorded for cell SnInP-Temp1. Two measurements were done at each temperature. One after the cell had adjusted to the temperature and one an hour after the first. An initial gain in performance was seen from raising the temperature. However, after an hour much of that gain was lost and ultimately there was a net loss with time. This degradation was faster at higher temperatures. Comparing with Figure 7.23(b) activation contribution as expected decreases with increased temperature. Again, after one hour some of the initial gain was lost and again at an accelerated pace with increasing temperature. The same trend was seen for the ohmic contribution (not shown here). This could indicate either the previously mentioned problem with the way the polarisation curves were fitted or an actual electrolyte degradation.
To illuminate this a second experiment was done and evaluated with impedance as well as polarisation (cell SnInP-Temp2). At each temperature the cell was left at 7.5 mA/cm^2 for 1 hour before polarisation and impedance was recorded. The starting temperature was 200 °C and the temperature was raised in intervals of 10 °C until 250 °C was reached. This temperature was chosen as end temperature for safety reasons as the cathodes used had a small amount of Teflon binder in them. PTFE has been reported to have a melting and decomposition onset as low as 280 °C[147] and even though the amounts of decomposition products evolved at this temperature should be below what is harmful to humans it was decided to keep below 250 °C at all times. Figure 7.24(a) shows the polarisation curves obtained over the temperature range. Only very slight changes in the polarisation curves were observed. A slight activation of the electrode processes with increased temperature was seen. A small increase in the ohmic resistance was also seen over time. The activation contribution of the polarisation curve decreased (Figure 7.24(b)). This was to be expected as the prominent electrode processes should be thermally activated.

The impedance results gave apparently conflicting results. When the voltage was raised the low frequency response decreased while the high frequency response remained unchanged (Figure 7.25(b)). This was entirely to be expected as mentioned in Section 7.3.3. When temperature was raised and a small voltage was applied (not shown) the low frequency element activated while the high frequency element deactivated. This corresponds to what was seen in Figure 7.24(b). When the polarisation was 1.6V or more

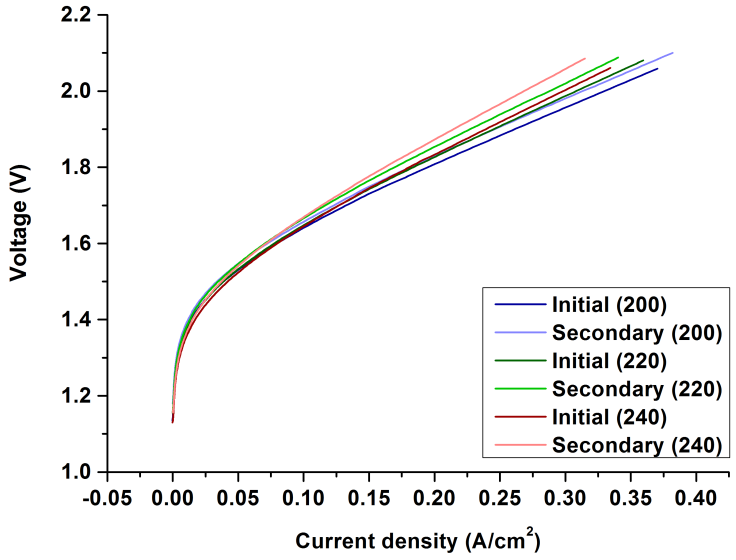

(a)

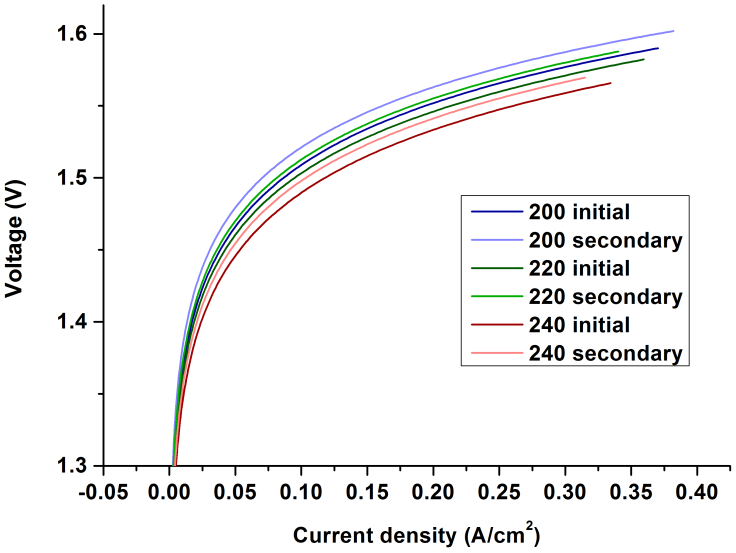

(b)

Figure 7.23: (a) polarisation curves and (b) activation contribution to the polarisation for a $Sn_{0.9}In_{0.1}P_2O_7$ electrolyser cell with variation of temperature (cell SnInP-Temp1)

both processes deactivated, as seen in Figure 7.25(a). First of all this means that the part of the electrode responsible for the high frequency process degrades over time. That the low frequency arc behaves differently depending on polarisation could mean it includes more than one element. This would have to be elements so close in time constants that they were not separated by DRT. As the impedance was recorded with a low amplitude, 10 mV, this may also have been a signal-to-noise issue.
It would be expected that the high frequency element would be activated with

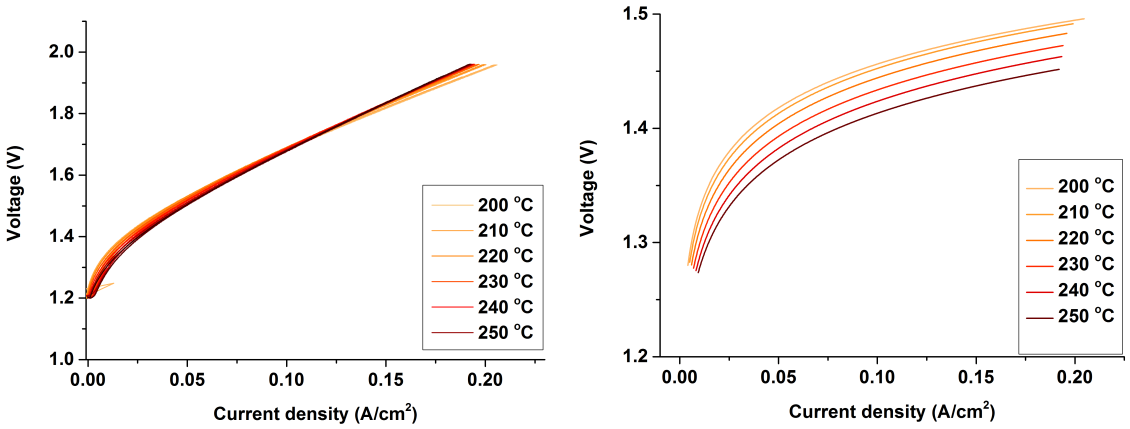

Figure 7.24: The effect of temperature for cell SnInP-Temp2 as seen in (a) Polarisation curves and (b) activation contribution. The activation overpotential decreases with increasing temperature as would be expected due to kinetic activation.

temperature as high frequency processes in this regime usually are related to fast electrode processes (e.g. charge transfer and ionic conduction). That the opposite was the case was a sign of degradation. Possible degradation mechanisms are e.g. platinum sintering and degradation of PTFE or the carbon support in the cathode. The degradation slows down over time/temperature which indicates that it was related to the PTFE binder or the catalysts in the electrodes as they in regards to degradation are limited resources where carbon cloth and support are not. As the platinum particles were already rather large, $\leq$ 20 μm, sintering was found to be unlikely. Thus PTFE was deemed the most likely culprit.

The resistance estimated from CNLS fitting of impedance data recorded at 1.8 V and 1.4 V are shown in Figure 7.26(a) and 7.26(b) respectively. These underlined the previous notions. The 1.8 V data showed a slight decrease in resistance for the electrolyte followed by a slight increase. 1.4 V showed only increase but the size of the standard errors of the 200 and 210 °C data points means that an initial decrease would be within the confidence interval and thus a decrease could not be ruled out. R_{p_1} increased in both instances and R_{p_2} increased at 1.8 V but decreases at 1.4 V. All resistances were tested for Arrhenius behaviour (not shown) standard errors were large (25 % to 100 %) and plots showed parabola curving of the data points.

As $Sn_{0.9}In_{0.1}P_2O_7$ has been seen to lose conductivity above 200-210 °C an initial decrease in R_e followed by an increase would be expected. While the changes in conductivity with temperature are noticeable they are not monumental. The difference between highest and lowest resistance was 2.7 %. While degradation might have been happening in the electrolyte longer term exposure to elevated temperature would be necessary to establish this with certainty.

R_{p_1} increases with temperature and degradation of the fast electrode process is evident. This again leads back to the possibly instability of the cathode.

In conclusion, at low applied voltage the slow electrode processes, R_{p_2}, showed activation with temperature. This was to be expect as the kinetics of the electrodes should improve

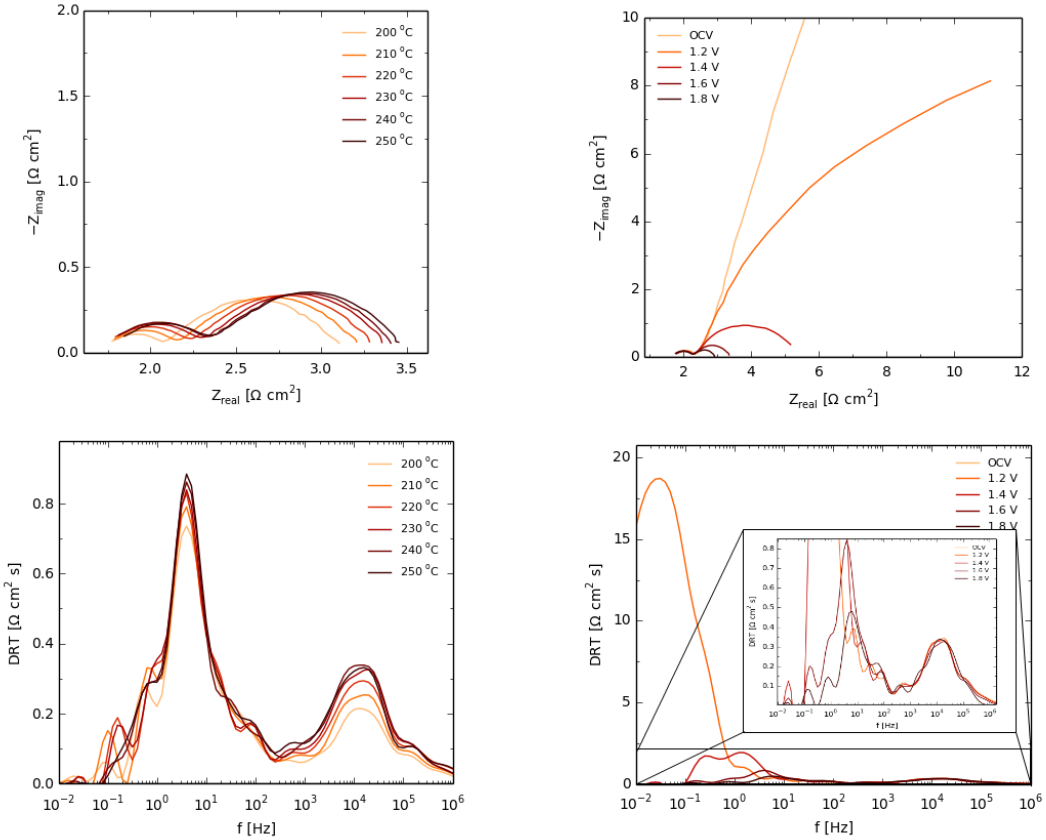

(a) (b)

Figure 7.25: The variation of impedance with temperature and polarisation (cell SnInP-Temp2) as seen in Nyquist plots and DRT. (a) shows data recorded over temperate at 1.6 V and (b) shows data recorded over polarisation at 230 °C.

with temperature. At higher applied voltage however all electrode processes showed signs of deactivation indicating degradation of both fast and slow electrode processes.

7.3.6 Higher operating current density

Table 7.11: $Sn_{0.9}In_{0.1}P_2O_7$ cell with higher current density.

Cell #	Flowplates	Steam	temperature	Impedance	Amplitude
SnInP-HC	1 Ta coated	steam on anode	200 °C	yes	50 mV

The effect of polarisation on the electrolyser cells was investigated. Instead of the low default operation current density a current density of 150 mA/cm^2 was chosen for a cell tested for 24 hours. This cell was compared with the first day of the testing of cell SnInP-Imp.
The polarisation curves for the two cells are shown in Figure 7.27(b). Cell SnInP-HC seemed to degrade faster than cell SnInP-Imp. The two cells were not directly comparable

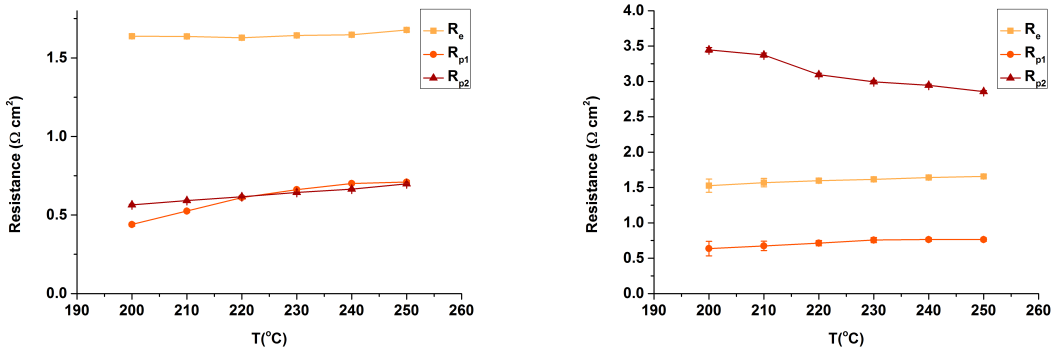

(a) (b)

Figure 7.26: R_e, R_{p_1} and R_{p_2} as a function of temperature (cell SnInP-Temp2). The resistance were estimated by CNLS fitting of impedance data recorded at (a) 1.8 V and (b) 1.4 V.

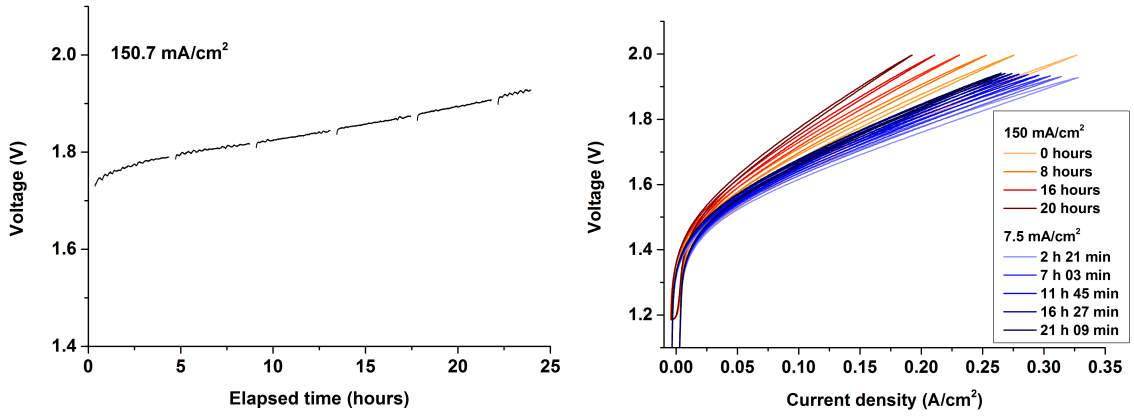

(a) (b)

Figure 7.27: The effect of 150 mA/cm^2 current density on a $Sn_{0.9}In_{0.1}P_2O_7$ cell (cell SnInP-HC). A clearly rising potential over time is seen in (a) and (b) shows a faster degradation as seen by polarisation curves than a cell operated at 7.5 mA/cm^2.

however as cell SnInP-HC has an electrolyte thickness of 0.90 mm and cell SnInP-Imp is only 0.65 mm thick.
Voltage loss every four hours at 150 mA/cm^2 was recorded as being: 10.9 mV/h, 5.7mV/h, 6.1 mV/h, 6.6 mV/h and 7.3 mV/h. As this is not directly comparable to values for other current densities impedance results were used.

For a more direct comparison σ_e, R_{p_1} and R_{p_2} were estimated by CNLS fitting. σ_e is the electrolyte conductivity. The results obtained for 1.8 V were compared to cell SnInP-Imp in Figure 7.28. The electrolyte conductivity showed a slightly more stable electrolyte for cell SnInP-HC. The overall stability of both electrolytes lead to the conclusion that higher current density did not promote electrolyte degradation.
R_{p_1} saw a much higher increase for cell SnInP-HC than for the cell operated at low current density. Over the cause of 20 hours the resistance increases sevenfold. R_{p_1} for

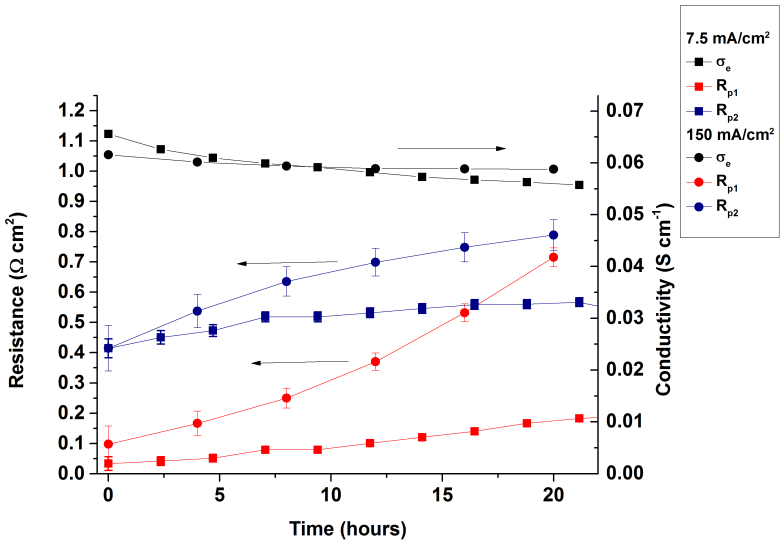

Figure 7.28: Electrolyte conductivity and polarisation resistance estimated from impedance by CNLS fitting recorded at 1.8 V for cell SnInP-Imp and cell SnInP-HC. Cell SnInP-Imp shows less degradation over time for both electrode elements. Cell SnInP-HC a slightly more stable electrolyte.

cell SnInP-Imp starts lower and increases fivefold over the same time scale. Values for R_{p_2} were initially identical for the two cells, but increased faster for cell SnInP-HC. Both cells increased most initially. Both electrode elements were thus seen to be vulnerable to polarisation over time. The high frequency element was evidently very sensitive with a dramatic increase in resistance and a total resistance after 20 hours rivalling that of the low frequency element.
As with cell SnInP-Imp visual inspection of the flow plates revealed a highly damaged cathode GDL. It is reasonable to believe that the high current density could have accelerated the degradation of the GDL. As R_{p_1} is related to the fast electrode processes a heavy degradation of the cathode would affect R_{p_1}.

7.4 Summary of results for pyrophosphates

The synthesis of $Sn_{0.9}In_{0.1}P_2O_7$ was seen to be profoundly affected by temperature. A constant ramp temperature was seen to give better results than stepwise ramping. While the electrochemically tested materials in this Chapter were made with a ramping temperature of 280 °C it was seen that 270 °C would likely give a more easily reproducible result.
Electrolysis was carried out using Pt-black as cathode electrocatalysts and IrO_2 as anode electrolyte. The highest current density achieved at a voltage comparable across the difference cells was 313 mA/cm^2 at 1.9V. The electrolysis cells worked with steam on both electrodes as well as steam only on the anode. There may be a gain in stability of the electrolyte if steam is supplied to both electrodes.
Impedance results suggested a stable electrolyte at 200 °C. This would seem to be in

contrast to the results of ohmic resistances estimated from polarisation results. However a link between the polarisation resistance estimated from impedance measurements and the ohmic resistance from the fits was seen. It was deemed likely that part of the polarisation resistance had been included in the ohmic resistance estimated from the fit.
One or possibly both electrodes were not stable with time. As the conducted reference electrode measurements were of too poor quality to give anything conclusive it is still uncertain which of the electrodes are degrading the most and at what time scale. The following possible degradation reasons have been suggested: platinum particles on the cathode may sinter, the carbon microporous layer on the cathode may erode, the PTFE in the cathode may soften and lead to collapse of the electrode structure and increased contact resistance, IrO_2 may be lost from the Ta coated SSF or particles may sinter and the electrolyte may be pressed into the electrode structure covering the active particles.
A loss of electrolyte performance was seen with temperature. Initial activation of the electrodes seemed to compete with degradation. The electrode elements related to charge transfer were deactivated with temperature while low frequency processes were seen to be both activated and deactivated. The deactivation was most likely degradation and not an actual deactivation of the processes. The electrode degradation may increase with temperature though this is not entirely conclusive.
Operation at increased current density accelerated degradation of the cell. The electrolyte was not affected but both the high frequency and the low frequency element were affected. R_{p_1} increased the most and as the cathode was highly damaged after testing it was concluded that this was the cause of the increase of the resistance at high frequency.
Many parameters of the electrodes could be optimised. First of all the stability issues seen require attention. A thorough study of the stability of IrO_2 at temperatures above 200 °C would be of great interest.
The electrolyte conductivity estimated from cell tests were found to be very close to the measured conductivity. An estimation at 200 °C shoved an initial conductivity of $6.6{\cdot}10^{-2}$ S·cm^{-1}, slightly lower than the conductivity at 210 °C $7.3{\cdot}10^{-2}$ S·cm^{-1}. A great improvement of performance would be expected from a thinner electrolyte.

CHAPTER 8

Other phosphates

To get a broader picture three other electrolytes were tested electrochemically. One of them, CsH_2PO_4, was tested in the form of stabilised composites as well as its pure form.

8.1 Bismuth and niobium cells

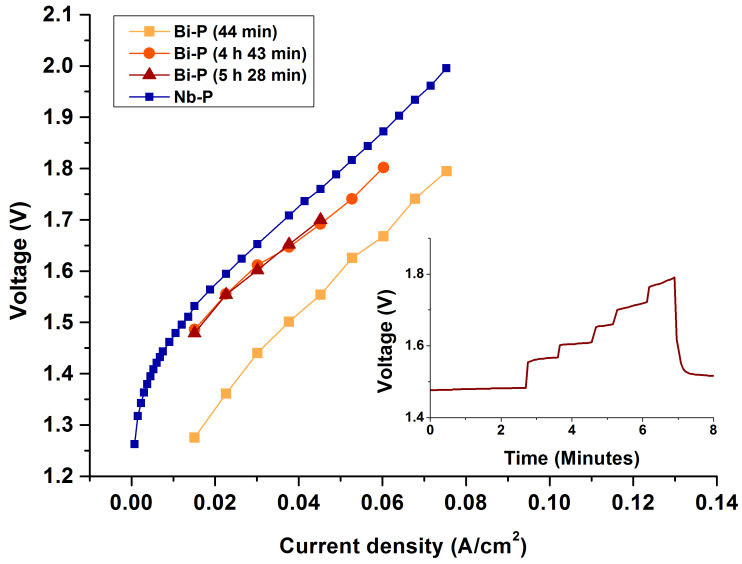

Figure 8.1: Polarisation curves for bismuth and niobium based cells. The insert illustrates the instability of the polarisation as exemplified for Bi-P after 5 hours and 28 min.

Possible phosphate electrolyte materials based on bismuth and niobium were tested. The materials were synthesised as described in Section 5.1.6 and Section 5.1.7 respectively. The bismuth phosphate (Bi-P) was by XRD (not shown) identified as a mixture of monoclinic $Bi_2P_4O_{13}$ and $BiPO_4$. The phosphoric acid treated niobium phosphate sample (Nb-P) was found to be monoclinic $Nb_5P_7O_{30}$ (not shown). The latter sample was possible to press into a pellet without the addition of a binder but the former had to have the addition of 2 wt.% PBI. Otherwise the pressed pellet would crumble or break before they could be transferred to the cell housing.

Table 8.1: Components and loadings of Bi-P and Nb-P electrolyser cells. E., A. and C. denotes electrolyte, anode and cathode respectively.

Cell #	Electrolyte	A. GDL	C. GDL	A. loading	C. loading	Thickness
BiP	Bi-P/PBI (2%)	Ta SSF	C paper	2.41 mg/cm^2	0.594 mg/cm^2	0.92 mm
NbP	Nb-P	Ta SSF	C paper	2.34 mg/cm^2	15.56 mg/cm^2	0.61 mm

Prior to cell testing conductivity measurements were done for the two materials by PhD Y. J. Huang (results not shown). Both samples were found to have conductivities above $1{\cdot}10^{-2}$ S·cm^{-1} at 200 °C in air and as such satisfy the conductivity demands for an electrolyte.
Measurements for Bi-P were done with a purely Pt/C cathode and with an in-house built power supply (see Section 6.1.2). Measurements for Nb-P were done with a Pt black cathode and a potentiostat.
The most promising results for each of the two materials are shown in Figure 8.1. The

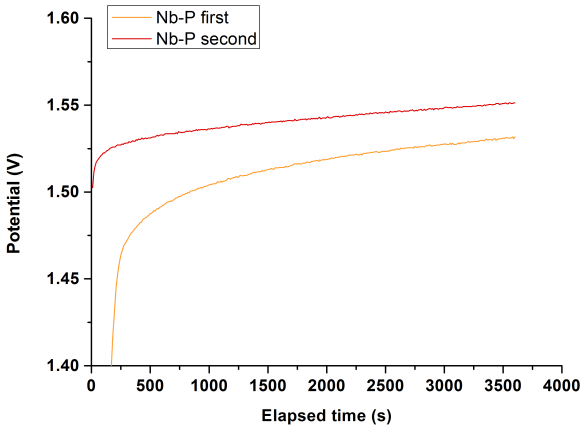

Figure 8.2: Short tests with Nb-P as electrolyte at 7.5 mA/cm^2. The voltage never stabilised.

parameters for these cells are detailed in Table 8.1. The best polarisation results were seen from the Bi-P cell where 75 mA/cm^2 were measured at 1.8 V. For cell NbP 1.95 V had to be reached before this current density was achieved. This was even though the Nb-P sample had 2/3 the thickness of the Bi-P electrolyte and nearly 30 times the platinum loading on the cathode.
The cell BiP was not stable during testing, and after a handful of hours the lack of stability was even noticeable during the measurement of polarisation curves. At this point it was decided that it made no sense to do further polarisation curve measurements as the voltage would not stabilise for the chosen current density. The instability of the cell may be related to the binder used. It has previously been illustrated that PBI has thermohydrolytic stability problems especially in oxidative environments.[28,148] Since the electrolyte powder was impossible to press without a binder it was decided that it was not to be investigated further as more promising alternatives existed.
Nb-P showed better stability during polarisation. It was however not satisfyingly stable

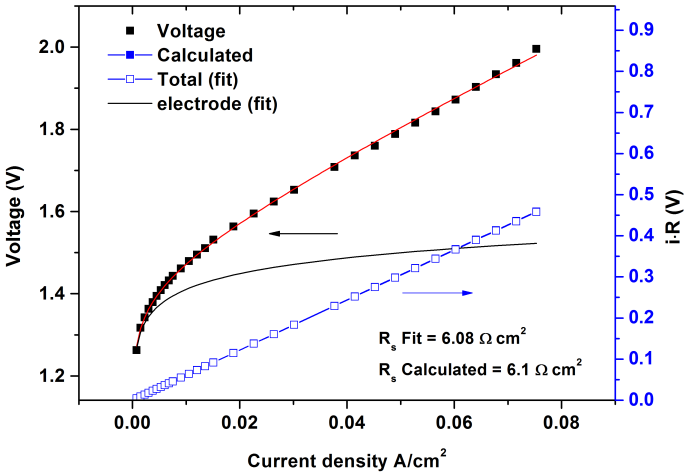

Figure 8.3: Polarisation fit for a Nb-P cell. Estimated values of R_s from the fit and conductivity data respectively are shown.

over time as can be seen in Figure 8.2. This data was recorded at 7.5 mA/cm^2 with just one minute in between the first and the second chronopotentiometric measurement. The voltage loss over time was calculated to 27.3 V/hour for the first hour and 18.7 V/hour for the second hour. This was between 25 and 90 times as high as what was seen for $Sn_{0.9}In_{0.1}P_2O_7$ in Section 7.3.2
The application of a potentiostat for polarisation of cell NbP gave the possibility of doing a polarisation curve fit. The results can be seen in Figure 8.3. From this fit the ohmic resistance of the cell was calculated which could in turn be recalculated to a conductivity (R_s = 6,08 $\Omega \cdot cm^2$ -> $1 \cdot 10^{-2}$ S $\cdot$ cm^{-1}). This was of the same magnitude as the measured value of conductivity (not shown). This means that the most pertinent focus apart from the stability issues would be to reduce the thickness of the cell. Unfortunately this also means that the electrolytes conductivity is limiting for the development of cells with this material. This coupled with the poor stability of the material led to the conclusion that it would not be worth the effort to continue the cell tests with this material.

8.2 CsH_2PO_4

As CsH_2PO_4 has been the most prominent IT fuel cell electrolyte the past 10 years it was attractive to test it as an electrolyte in IT electrolysis. The experiments carried out with CsH_2PO_4 based electrolytes are detailed in Table 8.2 and Table 8.3. The baseline for cell operation was a pure CsH_2PO_4 electrolyte tested at 250 °C. The super protonic transition of CsH_2PO_4 at 229 °C is a necessity for operation and the temperature of 250 °C was chosen to make sure any possible temperature gradient through the cell was inconsequential.
The initial cells were tested with steam on the anode only. The setup was later modified to allow for steam on both electrodes to hamper the dehydration of the electrolyte.
The presented results were done with Pt/C as electrocatalyst and Toray paper as GDL

for the cathode except for the cells CDP-TaSSF and CDP-Pt-b. Results obtained by others in our group showed the Pt/C electrocatalyst to have insufficient activity for these preliminary measurements. Therefore cell CDP-Pt-b was done with Pt-black in stead. For cell CDP-TaSSF the cathode was made using a piece of tantalum coated stainless steel felt (Ta SSF) as GDL. Here the ink used for electrocatalyst spraying was made with a 50/50 wt.% mix of electrolyte and electrocatalyst.
IrO_2 was used as anode electrocatalyst for all cells presented here. In the anode ink the electrolyte/electrocatalyst ratio was 50/50 wt.%. This ratio was assumed constant when calculating catalyst loading after anode spraying.

Table 8.2: Components and loadings for cells with CsH_2PO_4as electrolyte. A. denotes anode and C. denotes cathode. Support is electrolyte support

Cell #	Support	A. GDL	C. GDL	A. loading	C. loading
CDP1	None	Ta SSF (1)	C paper	0,90 mg/cm^2	1,11 mg/cm^2
CDP-ZO	ZrO_2, 33 wt.%	Ta SSF (1)	C paper	1,09 mg/cm^2	1,11 mg/cm^2
CDP-SiC1	SiC, 50 wt.%	Ta SSF (1)	C paper	1,43 mg/cm^2	1,11 mg/cm^2
CDP-SiC2	SiC, 50 wt.%	Ta SSF (1)	C paper	1,39 mg/cm^2	1,11 mg/cm^2
CDP-Temp	None	Ta SSF (1)	C paper	1,20 mg/cm^2	1,11 mg/cm^2
CDP-TaSSF	None	Ta SSF (1)	Ta SSF (1)	1,32 mg/cm^2	0,98 mg/cm^2
CDP-Pt-b	None	Ta SSF (2)	C paper	2,03 mg/cm^2	6,78 mg/cm^2

Table 8.3: Operating conditions and electrolyte data for CsH_2PO_4 cells. E. denotes electrolyte.

Cell #	Temp.	Steam	E. mass	E. thickness
CDP1	250 °C	Anode	0.6714 g	0.68 mm
CDP-ZO a	250 °C	Anode	0.5323 g	0.60 mm
b		both		
CDP-SiC1	250 °C	Both	0.3412 g	0.44 mm
CDP-SiC2	250 °C	Both	0.5306 g	0.56 mm
CDP-Temp	239 °C	Both	0.5011 g	0.58 mm
CDP-TaSSF	239 °C	Both	0.6234 g	0.71 mm
CDP-Pt-b	250 °C	Both	0.6027 g	0.70 mm

8.2.1 Pure CsH_2PO_4 with steam on the anode only

An example of an electrolyser cell with a pure CsH_2PO_4 electrolyte tested at 250 °C can be seen in Figure 8.4. After the start-up procedure a constant current was applied to the cell and the voltage response quickly shot to over 2.0 V even at the very low current density of 7.5 mA/cm^2. Even at 2.0 V no signs of a horizontal plateau was seen. One possible explanation for this could be failure for the electrolyte to reach the super protonic state. This seemed unlikely at a cell housing temperature of 250 °C. It was considered more likely that the lack of steam on the cathode allowed for dehydration on the cathode side of the electrolyte thus forming dehydration products. This would lead to loss of proton conductivity in the interface between the electrolyte and the cathode due to an insulating layer of dehydration products. This cell behaviour was seen for multiple cells.
It was concluded that the pure CsH_2PO_4 was too unstable. To investigate whether

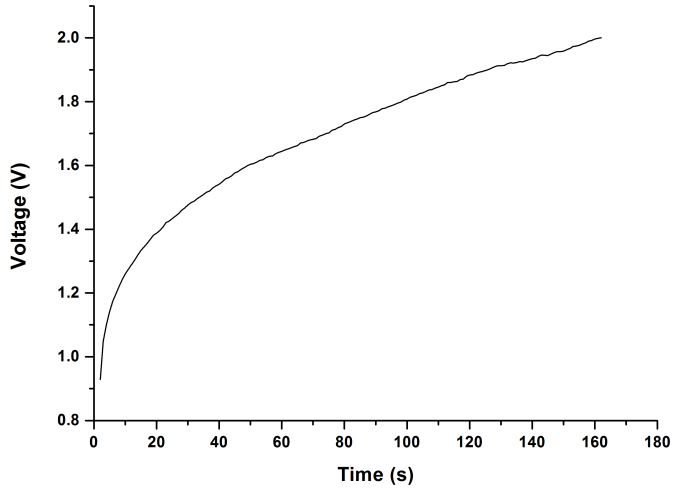

Figure 8.4: Pure CsH_2PO_4 full electrolyser cell. At low current density (I = 7.5 mA/cm^2) no stable potential was achieved (cell CDP1).

dehydration or mechanical instabilities were responsible stabilisation of the electrolyte and/or addition of steam to the cathode would be needed.

8.2.2 Stabilised composites of CsH_2PO_4 and the effect of steam

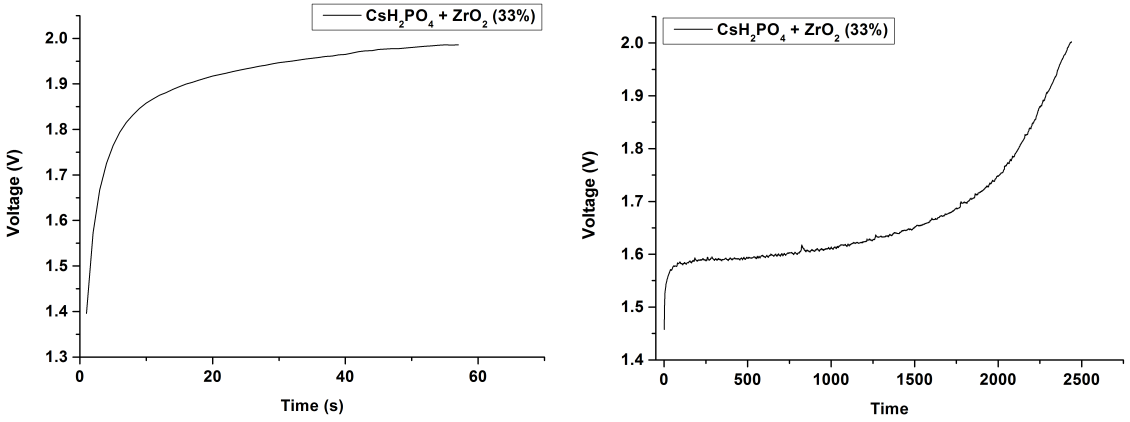

(a) (b)

Figure 8.5: CsH_2PO_4 + ZrO_2 (3:1) cell with steam on (a) the anode and (b) the anode and the cathode. Tested at 250 °C and 7.5 mA/cm^2 (cell CDP-ZO).

Stabilisation of the CsH_2PO_4 was attempted. Two types of stabilised electrolytes were tested. The first was added 33 wt.% ZrO_2. The second was stabilised with 50 wt.% SiC fibres by co-precipitation (see Section 5.1.3).
The initial test was done with the ZrO_2 stabilised sample and only steam on the anode (cell CDP-ZO). The result of this test can be seen in Figure 8.5(a). This stabilised sample showed

behaviour similar to pure CsH_2PO_4. On this time scale of tens of seconds it was impossible to compare the two cells meaningfully. Should it be attempted anyway it would be noted that the stabilised cell reached 1.95 V faster than pure CsH_2PO_4 but it showed greater signs of stabilisation.
The same cell was tested with steam added to the cathode side of the cell. Figure 8.5(b) showed a large gain both in stability and performance. The gain in performance was believed to be due to the regenerative nature of the dehydration of CsH_2PO_4 at high water partial pressures.[149] While the improvement was clear it was not long lasting. It was uncertain what caused this failure as no dehydration products should be able to form. After disassembly the cell housing no mechanical failures could be seen.

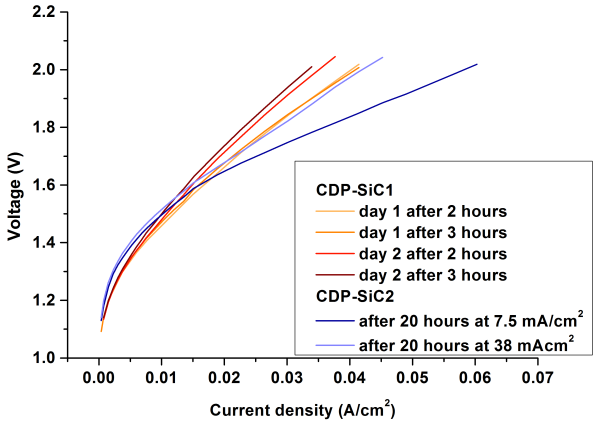

Figure 8.6: Polarisation curves SiC stabilised CsH_2PO_4 (1:1) electrolyser cell. Results from cells CDP-SiC1 and CDP-SiC2 are shown.

Two SiC stabilised CsH_2PO_4 (50 wt.%/50 wt.%) cells were tested. Cells CDP-SiC1 and CDP-SiC2, see Table 8.2. Cell CDP-SiC1 was held at 7.5 mA/cm^2 for 2 hours, a polarisation curve was measured, it was left at 7.5 mA/cm^2 for one hour and polarisation was done again. The cell was then turned off and the experiment was repeated the following day. Cell CDP-SiC2 was held at 7.5 mA/cm^2 for 20 hours, a polarisation curve was measured and the process was repeated with the current density raised to 38 mA/cm^2. All experiments were done with steam on both electrodes. The resulting polarisation curves are depicted in Figure 8.6.
The addition of SiC had a clear effect. These cells showed a much more stable performance than what was seen for the pure and the ZrO_2 stabilised CsH_2PO_4. Cell CDP-SiC1 showed a degradation of 5.1 mV/hour at 7.5 mA/cm^2 during the initial two hours and cell CDP-SiC2 showed an average voltage loss of 0.7 mV/hour during initial 20 hours at 7.5 mA/cm^2. Cell CDP-SiC1 showed little performance loss between polarisations. It was however more pronounced after the cell was shut down and started up again. Cell CDP-SiC2 showed high stability at 7.5 mA/cm^2 with a overall better performance after 20 hours than cell CDP-SiC1 had after two. At 38 mA/cm^2 the loss was higher, estimated at 6.2 mV/hour. This value was comparable to the results seen for cell CDP-SiC1 at 7.5

Table 8.4: Resistance and conductivity estimated from polarisation curves for CsH_2PO_4/SiC cells.

Cell #	Time	R_s ($\Omega \cdot$ cm^2)	σ (S $\cdot$ cm^{-1})
CDP-SiC1	2 hours	14.30	$3.1 \cdot 10^{-3}$
	3 hours	13.89	$3.2 \cdot 10^{-3}$
	2 hours (day 2)	17.05	$2.6 \cdot 10^{-3}$
	3 hours (day 2)	17.67	$2.5 \cdot 10^{-3}$
CDP-SiC2	20 hours (7.5 mA/cm^2)	6.87	$8.1 \cdot 10^{-3}$
	40 hours (38 mA/cm^2)	11.45	$4.9 \cdot 10^{-3}$

mA/cm^2. The reason for this difference in stability between the cells is uncertain. The only notable difference between the two cells was the thinner electrolyte of cell CDP-SiC1. That cell CDP-SiC2 needed a higher current density to degrade at the same pace as CDP-SiC1 is hardly explained by the difference in thickness of the electrolytes.
The current densities achieved for the two cells were rather low. Cell CDP-SiC2 showed the best performance with 60 mA/cm^2 at 2.0V. This was still far below what was achieved for $Sn_{0.9}In_{0.1}P_2O_7$ (313 mA/cm^2 at 1.9 V). Table 8.4 shows the estimated ohmic resistance from the polarisation curves along with the estimated values for proton conductivity under the assumption that the electrolyte is the only contributor to the ohmic resistance. A high resistance was seen for cell CDP-SiC1 throughout with a jump after shut down/start-up. Cell CDP-SiC2 showed a conductivity close to $8.1 \cdot 10^{-3}$S$\cdot$cm^{-1} initially. This was encouraging as this was relatively close to the conductivity of pure CsH_2PO_4 at ideal conditions ($1.8 \cdot 10^{-2}$S$\cdot$cm^{-1} at 233 °C[46]). As the ohmic part of the polarisation fit may include more than just the electrolyte the CsH_2PO_4 could still be working as intended and the fault for the poor performance may lie with the electrodes. To investigate whether the limited amount of platinum present on the cathode was partly responsible it was attempted to test a SiC stabilised cell with Pt black. The experiment did not work however and no more time could be devoted to this pursuit.

8.2.3 Variation of temperature

It was speculated that the temperature of 250 °C softened the electrolyte to a point where it could deactivate the electrode surfaces by filling up the surface porosity. Therefore an experiment with an initial temperature of 239 °C was done (CDP-Temp). Testing ended when the cell voltage exceeded 2.0 V, some times a bit more. Testing was then recommenced at a higher temperature. The additional experiments were done at 250, 260 and 270 °C. The initial temperature of 239 °C was used for testing two times before the temperature was raised to 250 °C.

Figure 8.7 shows the resulting time vs. voltage curves. Compared to cell CDP1 improvements were seen. However compared to cell CDP-ZO with steam on the cathode this cell with pure CsH_2PO_4 left something to be desired. The cell was tested for a maximum of 10 minutes never stabilising. Raising the temperature lead to no improvements and as a general trend the following measurement continued where the preceding left off. We are hesitant to draw any conclusions based on this cell but what can be inferred is that lowering the temperature is not enough to stabilise a cell with pure CsH_2PO_4. It is possible that lowering the temperature 239 °C can be beneficial for cells already somewhat stable.

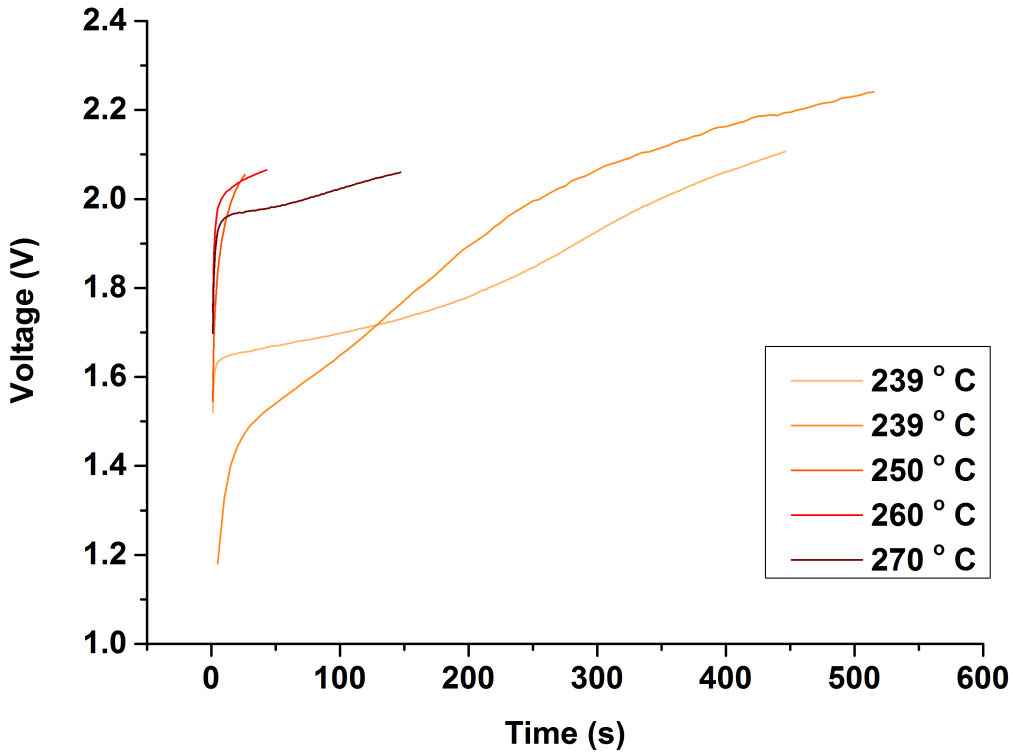

Figure 8.7: Cell testing initiated at a variety temperatures. Current density = 7.5 mA/cm^2 (cell CDP-Temp).

As the literature predicts that the electrolyte should have no problems under these conditions it is suspected that one or more of the electrodes are to blame for the fast degradation. As the cathode had PTFE in the microporous layer the softening of this could be the reason for the failure.

8.2.4 Alternative cathode GDL

The cathode microporous layer included PTFE as a binder. The softening of this could be one of the reasons for the fast failure of the cells. To illuminate the role of the cathode GDL in electrode degradation of pure CsH_2PO_4 cells the carbon GDL was replaced by a Ta-coated SSF GDL. No support was used and Pt/C was applied onto the felt by spraying an EtOH based ink. The cell was tested at 239 °C as a small stability increase had been seen at this temperature. The results are found in Figure 8.8(a) and Figure 8.8(b).

The resulting cell (cell CDP-TaSSF) was much more stable than what had previously been seen for pure CsH_2PO_4. Before polarisation the cell lost approximately 9.0 mV/hour. After polarisation the cell lost 5.6 mV/hour. Even though that was a clear improvement the polarisation clearly had a detrimental effect on the cell. The voltage at 7.5 mA/cm^2 increased markedly after polarisation. The polarisation curves themselves shows the detriment to the cell (Figure 8.8(b)). Even though, this was the best performance seen for a cell with pure CsH_2PO_4. It was tested for almost a full day before it was shut down (Figure 8.8(a)). Even though it was not on par with the SiC stabilised cells the effect of

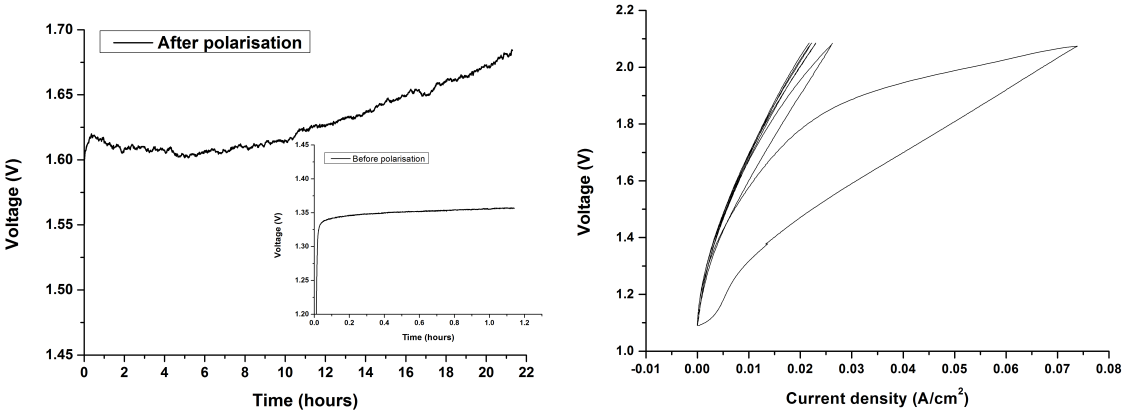

(a) (b)

Figure 8.8: CsH_2PO_4 electrolyser cell a Ta coated stainless steel felt cathode GDL (CDP-TaSSF). (a) Performance before polarisation was comparable to $Sn_{0.9}In_{0.1}P_2O_7$ (insert). Lower performance was seen after polarisation but the stability was highly increased compared to previous cells. (b) polarisation was seen to be detrimental to the cell. Scan rate = 5mV/s.

the change of GDL was not to be mistaken. The most likely reason for the increase in stability was the lack of PTFE in the electrode structure. If the Ta-coated SSF is to be used some kind of support layer would be needed and a different binder should be used. Both cloth, micro-porous layer and electrocatalyst contains large amounts of carbon. This may be unstable as well. For continued development the effect of the high temperature on the carbon species in traditional cathodes should be investigated.

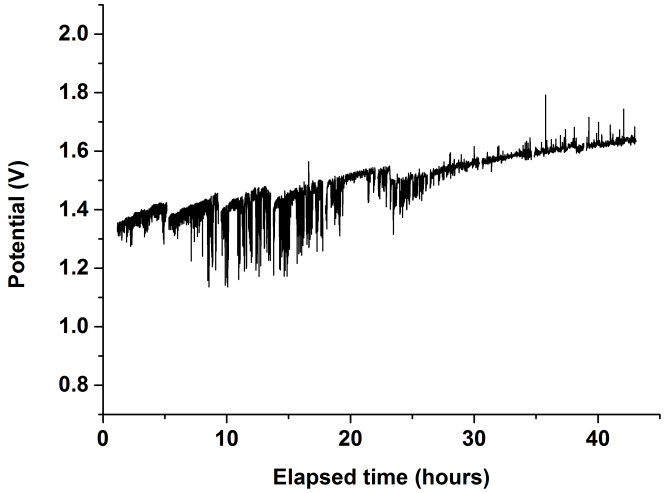

Figure 8.9: The stability of the pure CsH_2PO_4 cell with Pt-black for cathode electrocatalyst (cell CDP-Pt-b). Current density = 7.5 mA/cm^2.

8.2.5 Pt-black as cathode electrocatalyst

Since it was conjectured that Pt/C was a bad match for the electrolysis conditions a cell was made with pure Pt-black for the cathode electrocatalyst on a carbon GDL. The cell, named CDP-Pt-b, was tested with steam on both electrodes.
During testing it was noticed that oscillations in the steam supply on the anode affected the measured potential (Figure 8.9). Spikes (up and down) were observed in the potential not previously seen in cell experiments. To allow for connection of two evaporators additional piping was needed. These pipes did not have heating elements and relied on insulation to keep the steam from condensing. The insulation could not ensure an even temperature distribution along the entire length of the pipe resulting in an uneven steam flow. This may in turn have affected the anode. While this was not observed for previous experiments with steam on both electrodes this electrolysis cell had a anode GLD of felt type 2 (Section 5.4.1). The more closed surface of the GDL may have resulted in a filling of the surface porosity when the anode was sprayed. This would have given an insufficient access of steam to the electrolyte-electrode interface. This could have left the cell vulnerable to the steam fluctuations as starvation/flooding would follow the oscillations.
Comparing with the results seen in Figure 8.8(a) the Pt-black cell showed a lower potential after polarisation. The voltage loss was 7.47 mV/hour for the 42 hour long test. The Pt-black electrode was not affected by polarisation the same way as cell CDP-TaSSF.
Polarisation curves were recorded every 4 hours. They can be seen in Figure 8.10(a).

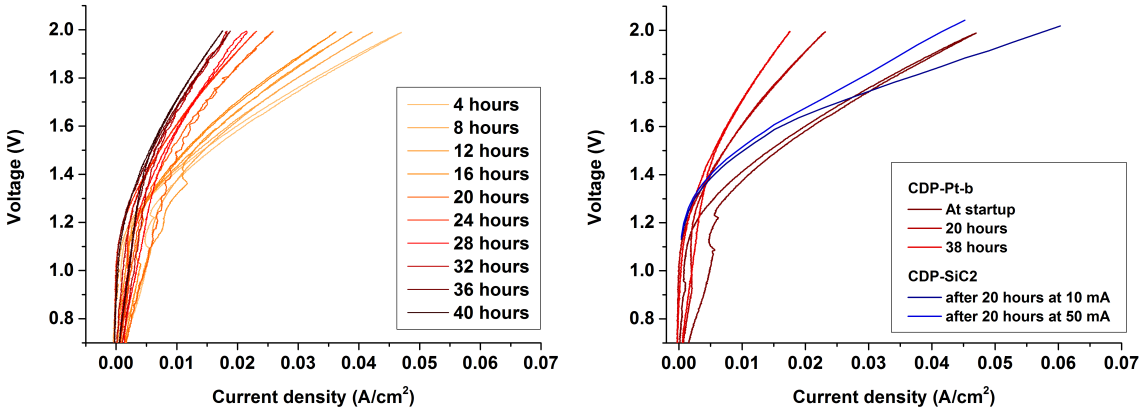

(a) (b)

Figure 8.10: Polarisation curves recorded for a CsH_2PO_4 electrolyser cell with a Pt-black cathode electrocatalyst (cell CDP-Pt-b). (a) performance is lost over time. (b) a SiC stabilised electrolyte gave a more stable performance than the pure CsH_2PO_4 Pt-black cell.

Comparison with the cells with a SiC stabilised electrolyte (Figure 8.10(b)) showed that while the Pt-black cathode cell performs better in the activation regime the part of the polarisation curve associated with the ohmic part of the cell was outperformed by the SiC stabilised cell. There was also a larger degree of degradation for the Pt-black cell over time.
Too many factors influenced the experiment to make solid conclusions. The anode

might have alternately been starved and flooded by steam fluctuations, the electrocatalyst particles might have been lost during operation, the carbon cloth might have been deteriorating and the electrolyte might have been degrading with time.

8.3 Summery of results for other phosphates

A mixture of monoclinic $Bi_2P_4O_{13}$, $BiPO_4$ and 2 wt.% PBI (Bi-P) was tested as electrolyte. A phosphoric acid treated monoclinic $Nb_5P_7O_{30}$ sample (Nb-P) was tested as well. Both materials showed a reasonable but not impressive conductivity of $1{\cdot}10^{-2}S{\cdot}cm^{-1}$. Neither were however stable during electrolysis. They degraded fast over a few hours and the Bi-P sample was not even stable during polarisation. The stability issues together with the somewhat low conductivity disqualified the materials from further testing.
CsH_2PO_4 was tested with and without steam on the cathode. Steam on both electrodes was found to be a necessity for stable measurements. To stabilise the electrolyte addition of ZrO_2 (33 wt.%) and of SiC fibres (50 wt.%) was explored. ZrO_2 gave a more stable electrolyte but a poorer performance. The gain was found to be too little for further exploration. The SiC fibres gave a higher degree of stabilisation as well as performance. The highest current density measured was 60 mA/cm^2 at 2.0 V. This was far from the performances seen for $Sn_{0.9}In_{0.1}P_2O_7$. The conductivity was initially estimated to be $8.1{\cdot}10^{-3}S{\cdot}cm^{-1}$ which is close to the conductivity reported in the literature, $1.8{\cdot}10^{-2}S{\cdot}cm^{-1}$. Thus the cells failure over time could be related to the electrodes rather than the electrolyte.
For pure CsH_2PO_4 it was seen that exchanging the default cathode felt, a carbon micro-porous layer with a PTFE binder on carbon paper, with a tantalum coated stainless steel felt gave higher stability over time. This was interpreted as a result of the absence of PTFE in the electrode as softening of PTFE at temperatures of 250 °C would lead to higher contact resistance and possible collapse of the micro-porous layer.
Pt black was attempted tested as cathode electrocatalyst with CsH_2PO_4. The results obtained from the experiment indicated a flooding/starvation of the anode with oscillating steam. While this had nothing to do with the cathode it made interpretation of the results difficult. A comparison with previous results for SiC-CsH_2PO_4 with Pt/C electrocatalyst indicated a better electrode performance but worse stability. In an attempt to get results that would be easier to interpret it was attempted to test a cell with SiC-CsH_2PO_4 and a Pt-black cathode electrocatalyst. This was unsuccessful.
A thorough reworking of the electrodes would appear to be needed to make electrolysis with CsH_2PO_4 possible. A different GDL would be necessary.

CHAPTER 9

Electrocatalysts and electrodes

9.1 Platinum as electrocatalyst

The results of Chapter 7 and Chapter 8 lead to speculation on whether the carbon supported platinum electrodes with a PTFE binder was stable for the HER at temperature of 200 °C and above. To investigate this a $Pt|Sn_{0.9}In_{0.1}P_2O_7|Pt$ hydrogen pump experiment was done. The symmetric cell was assembled with a Toray paper Pt-black on microporous carbon electrode on both sides. The loading of platinum was 8.86 mg/cm^2. Humidified hydrogen (0.050 atm) was fed to the cell on one end plate and looped to the other side of the cell. The flow rate was 50 mL/min. The electrolyte was 0.6025 g $Sn_{0.9}In_{0.1}P_2O_7$ (batch (G)) and had a thickness of 0.65 mm. Impedance was measured at 0 mV, 50 mV, 100 mV and 200 mV with an amplitude of 20 mV. Polarisation curves were done at 5 mV/s from -200 mV to 200 mV in groups of 3. Between each group of polarisation and impedance measurements chronoamperometry was done at 100 mV for 8 hours. The initial temperature of the cell was 200 °C. After 123 hours and 15 min the temperature was raised to 250 °C.

DRT was done as a preliminary evaluation (not shown). A prominent inductance contribution ($\approx$ 3.5 $10^{-5}\Omega\cdot$s) at high frequencies had to be corrected for. Two elements were seen at 28.4 kHz and 1.56 Hz respectively. Resistance for these time constants were seen to increase over time. To quantify the changes R_e, R_{p_1} (high frequency) and R_{p_2} (low frequency) were estimated by CNLS fitting. Here the inductance was included as part of the fit instead of corrected by KK. Measurements done at 0 mV were impossible to fit with sufficient confidence and were not included. The resistance plots for 200 mV polarisation bias are shown in Figure 9.1. The values for 100 mV and 50 mV showed similar trends and similar values. Fits of the data after the temperature was raised gave much larger errors of fit (shown as error bars) than what was seen at 200 °C. Despite this the trend of the data could still be followed and the data from the fits have been included.

The data at 200 °C for R_e falls in two segments. Up to 82 h 30 min a stable ohmic resistance around 5.15 Ωcm^2 was seen with variations almost falling within the uncertainty of the fits (>1 %). The same stability was seen for 90 h 45 min and up except the values are shifted down to around 4.85 Ωcm^2. In general these ohmic resistances are high compared to what has been shown previously. One possible explanation of this behaviour could be the relative high age of the electrolyte batch when this experiment was done. The batch was 6 months old and could have taken up some amount of water. This could have made the phosphoric phase more mobile and allowed for some of the protonic conductivity to be lost as the water was pressed out of the powder during pellet pressing. This would in turn mean a generally higher instability of the electrolyte. R_{p_1} and R_{p_2} show a sharp increase from beginning to 41 hour 15 min. Both tripled in this time frame. A continued

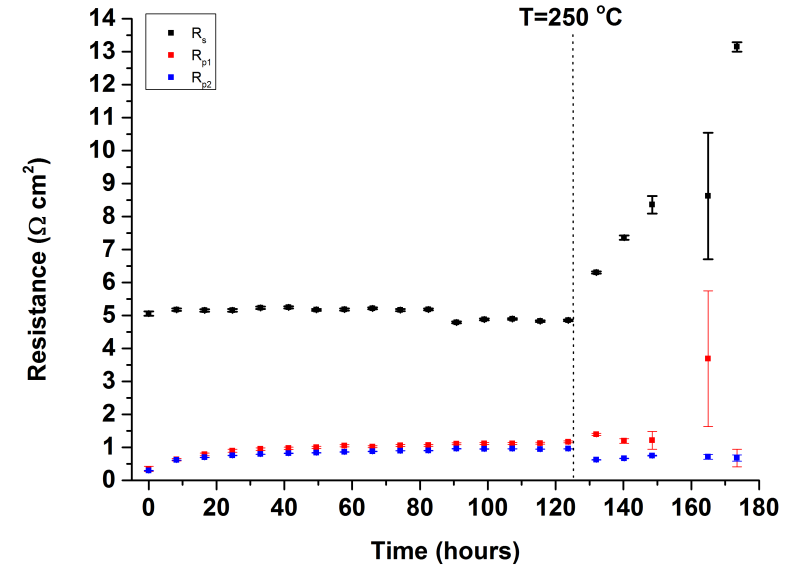

(a)

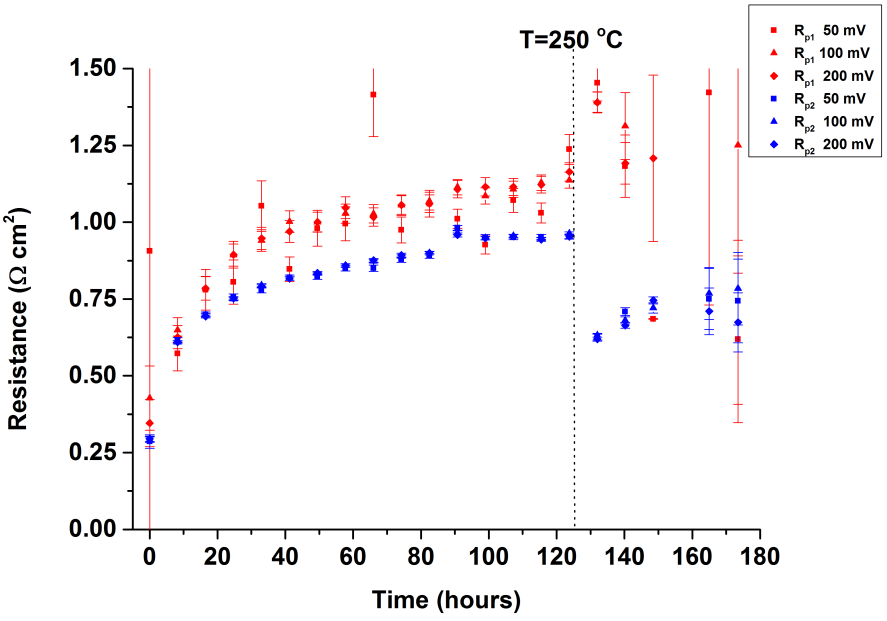

(b)

Figure 9.1: R_e, R_{p_1} and R_{p_2} over time in a Pt|$Sn_{0.9}In_{0.1}P_2O_7$|Pt cell. Hydrogen on both sides, p_{H_2O}=0.05 atm. Here shown for 200 mV polarisation. (a) shows the entire range and (b) is zoomed for better presentation of the polarisation resistances.

loss was seen over time for both processes. While the loss lessened it was clear that the electrodes were not stable. As mentioned this could be a result of both loss of platinum and degradation of the carbon structure either due to softening of PTFE or loss of carbon in the microporous layer. More experiments would be needed to qualify this.
R_{p_2} decreases with the elevated temperature indicating an activation. This would likely be related to an activation of the OER reaction on the anode. R_{p_1} gets very high error values for the fit making it very hard to find a trend apart from increasing errors. Such guesses would be too speculative.
After raising the temperature to 250 °C it was clear that the ohmic resistance increased and continued to do so. The rate of increase appeared to be linear. The instability at this high temperature may result from the previously mentioned age of the sample. If water uptake had happened the phosphoric acid could be much more mobile than in an as synthesised sample. It is however likely that the electrolyte in itself was not stable at elevated temperature as some of the previous experiments have pointed to. The previously reported lowering of conductivity above 200-210 °C[82] could be due to slow degradation and what was seen here could be an accelerated degradation of this sort. This would fit well with the previously seen increases in electrolyte resistance at higher temperature. The stability at 200 °C is noteworthy. Even though it exhibited a high electrolyte resistance it was still entirely stable at 200 °C over 120 hours. Work done by others in our group[150] have shown $Sn_{0.9}In_{0.1}P_2O_7$ to be stable over thermal cycling up to 280 °C. These experiments were done at p_{H_2O}=0.15 atm compared to the p_{H_2O}=0.05 atm used in this work. Thus the reason for the instability seen at 250 °C was likely due to a too low water partial pressure. This is encouraging as $Sn_{0.9}In_{0.1}P_2O_7$ may yet be found to function above 200 °C for longer periods of time. Long term testing at higher water partial pressure as well as higher temperature would be needed to verify this.

9.2 Alternative Catalyst materials

A selection of alternative electrode materials were tested with a tin indium pyrophosphate electrolyte. Two types of tungsten carbide, each from a different synthesis route, were used as cathode electrocatalyst. For the anode $LaNiO_3$ powder and Ni foam was tried. The foam was used as combined electrocatalyst and GDL while the $LaNiO_3$ was applied to a Ta coated stainless steel felt of the type normally used for anodes. The Ni foam was also tried as cathode electrocatalyst.

Table 9.1: Components and loadings of $Sn_{0.9}In_{0.1}P_2O_7$ cells with alternative electrode materials

Cell #	E. batch	E. mass	E. thickness	A. Mat.	C. Mat.	A. loading	C. loading
SnInP-WC1	SnP-(J)	0.6014 g	0.57 mm	IrO_2	WC (mWO_3)	2.33 mg/cm ^{2}	10.25 mg/cm^2
SnInP-WC2	SnP-(G)	0.6109 g	0.62 mm	IrO_2	WC (mW2N)	1.70 mg/cm ^{2}	7.61 mg/cm^2
SnInP-Ni-an	SnP-(I)	0.6011 g	0.60 mm	Ni	Pt-black	–	8.86 mg/cm^2
SnInP-Ni-cat	SnP-(H)	0.6027 g	0.69 mm	IrO_2	Ni	2.26 mg/cm ^{2}	–
SnInP-LNO	SnP-(G)	0.6602 g	0.69 mm	$LaNiO_3$	Pt-black	4.82 mg/cm ^{2}	8.86 mg/cm^2

9.2.1 Tungsten Carbide as cathode electrocatalyst

Two types of WC electrocatalysts were tested. Cell SnInP-WC1 used WC(mWO_3). This cell was tested with hydrogen on the cathode from start to finish (Table 9.2) in order to keep oxide formation on the electrocatalyst to a minimum. The surface oxidation of WC would be expected to especially be a problem during start up where no hydrogen is produced on the cathode.

The WC(mWO_3) cell (cell SnInP-WC1) was found to be functional(Figure 9.2). The cell

Table 9.2: Components and loadings of $Sn_{0.9}In_{0.1}P_2O_7$ cells with WC cathodes.

Cell #	Flowplates	Steam	temperature	Impedance	Amplitude	H_2 flow
SnInP-WC1	2 Ta coated	Steam on anode	200 °C	yes	10 mV	2.01 L/hour
SnInP-WC2	2 Ta coated	Steam on anode	200 °C	yes	30 mV	–

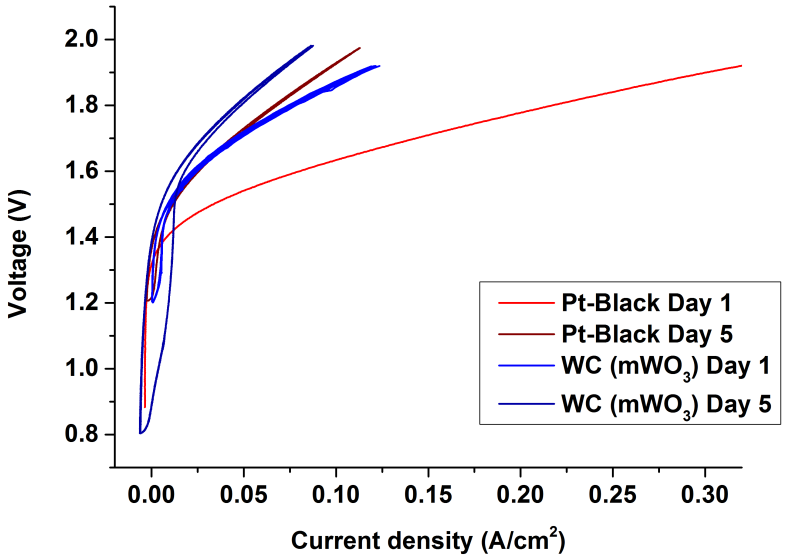

Figure 9.2: Polarisation curves for a WC(mWO_3) electrocatalyst cell (cell SnInP-WC1) at beginning of testing and after 5 day. A Pt black cell is included for reference. Higher stability but lower performance was seen for the WC(mWO_3) cell.

was tested for 5 days. The cell showed a quite reasonable stability but somewhat low performance, in the range of what was seen for CsH_2PO_4, Nb-P and Bi-P cells rather than what had previously been seen for cells with a $Sn_{0.9}In_{0.1}P_2O_7$. The highest initial current density was 129 mA/cm^2 at 1.9V. The low performance might originate from a low active surface area of the WC, incorrect loading, oxidation of the electrocatalyst surface or the electrocatalytic activity of the material itself. Apart from the latter possibility all of the above are improvable.

Figure 9.2 shows a comparison of polarisation curves at day one and after five days of operation for this cell and for cell SnInP-Imp. The Pt-black cathode cell clearly

degraded much more from start to finish compared to the WC. This bodes well for the WC electrocatalyst as stability over time may well be more important than raw electrocatalytic activity in the long run. The low cost of WC also makes it viable to increase the loading of electrocatalyst to alleviate the effect of a lower catalytic activity at 200 °C.
The comparison between the two electrocatalysts indicates that the performance loss in the Pt electrode is related to the Pt electrocatalyst itself. While there may well be some stability issues with the carbon cloth GDL, especially the PTFE binder in the micro-porous layer, this cannot explain the difference in performance loss in the two cells as the same GDL is used. One reason for the loss in the Pt cell may be agglomeration/ripening of Pt particles. As the Pt particles are, as previously mentioned, fairly large this is improbable. It is more likely that they adheres too loosely to the carbon structure and are transported from the cathode by the gas flow.

Reference electrode experiments were done for this cell. The results for day 1 and day 5 can be seen in Figure 9.3(a) and Figure 9.3(b) respectively. These appear much more stable than the ones seen for cell SnInP-Ref (see Section 7.3.4). The polarisation after 5 days seemed to do some damage to the cell. From these it was clear that the majority of the change observed in the cell over 5 days stemmed from the cathode. This was not necessarily a deactivation of the electrocatalyst and might as mentioned be related to the micro-porous layer in the cathode.
The second WC sample tested was a mW_2N sample (cell SnInP-WC2). The cell was started the same way as cell SnInP-WC1, with hydrogen at the cathode (2.01 L/hour). However, it turned out that the hydrogen flow repressed the electrolysis process. When current was applied a competing process kept the voltage at 0.19 V. While it was possible to do chronoamperometric measurements chronopotentiometry was not. Therefore the hydrogen flow was turned off. This made the cell behave as previously seen for cell SnInP-WC1 and the cell was tested for 42 hours at 7.5 mA/cm^2. It was speculated that the reason for the competing process was related to hydrogen crossover through the electrolyte. The electrolyte might not have been completely dense and it might be somewhat gas permeable when a pressure gradient was existing across the membrane. As the anode was at ambient pressure and the cathode was connected to the gas supply in one end and a gas trap in the other a gradient may well have existed. The highest initial current density measured was 73 mA/cm^2 at 1.9V.
The lack of hydrogen did not influence the cell in any obvious way. It does unfortunately make it somewhat difficult to compare cells SnInP-WC1 and SnInP-WC2 directly as the conditions are not identically. Both are shown in Figure 9.4(a) for good measure and it can be seen that the performances are quite similar in the end. It is also seen from the figure that Cell SnInP-WC2 showed greater stability than cell SnInP-WC1 over time.

Cell SnInP-WC2 was after the experiment with temperature (see Section 9.2.2) left to run at 250 °C for 65 hours. As can be seen in Figure 9.4(b) this had a detrimental effect on the cell. Impedance data (not shown) showed degradation of all parts of the cell.

9.2.2 Temperature experiment with WC cathode

A temperature experiment mirroring cell SnInP-Temp2 was done for the tungsten carbide cell SnInP-WC2. It should be noted that the WC(mW_2N) cell had a history, contrary to the Pt cell. It had already been tested for 42 hours before the temperature experiment was initiated. While this made direct comparison difficult it also had the possible positive side

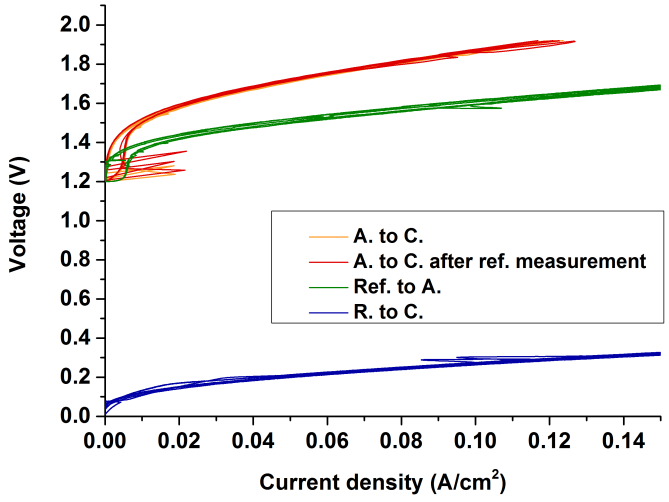

(a)

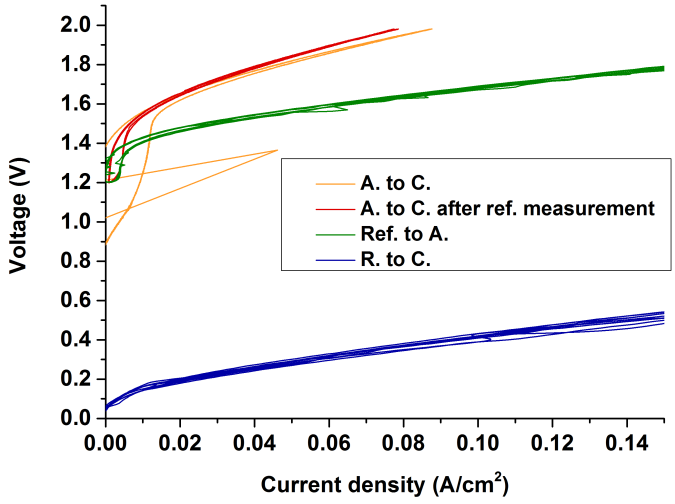

(b)

Figure 9.3: Reference electrode measurements for a WC(mWO_3) (cell SnInP-WC1) electrocatalyst (a) at beginning and (b) at the end of 5 days of testing. A., C. and Ref. denotes anode, cathode and reference respectively.

effect of the cell having been allowed to stabilise. All initial time related losses would have happened and all changes seen would be expected to be due to temperature.
Cell SnInP-WC2 mirrored cell SnInP-Temp2 very closely. The only difference was the cathode electrocatalyst. During the experiment temperature was raised after a cycle of 1 hour of constant current (7.5 mA/cm^2) plus polarisation and impedance measurements. The temperature interval was 200-250 °C and the temperature was raised 10 degrees every cycle.
Figure 9.5(a) shows the polarisation data for cell SnInP-WC2 during the temperature experiment. Its general behaviour was as hoped and expected. The activation part of the

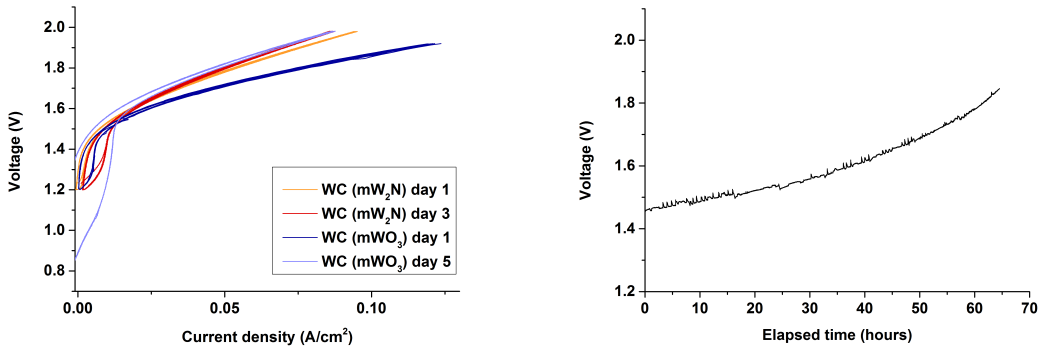

(a) (b)

Figure 9.4: (a) shows the polarisation curves for a WC(mW_2N) electrocatalyst (cell SnInP-WC2) compared to a WC(mWO_3) electrocatalyst (SnInP-WC1). (b) shows the WC(mW_2N) samples stability at 250 °C.

Table 9.3: Conditions of a $Sn_{0.9}In_{0.1}P_2O_7$ cell with variation of temperature and WC cathodes.

Cell #	Flowplates	Steam	temperature	Incriment	Impedance	Amplitude
SnInP-WC2	2 Ta coated	steam on anode	200 - 250 °C	10 °C	yes	30 mV

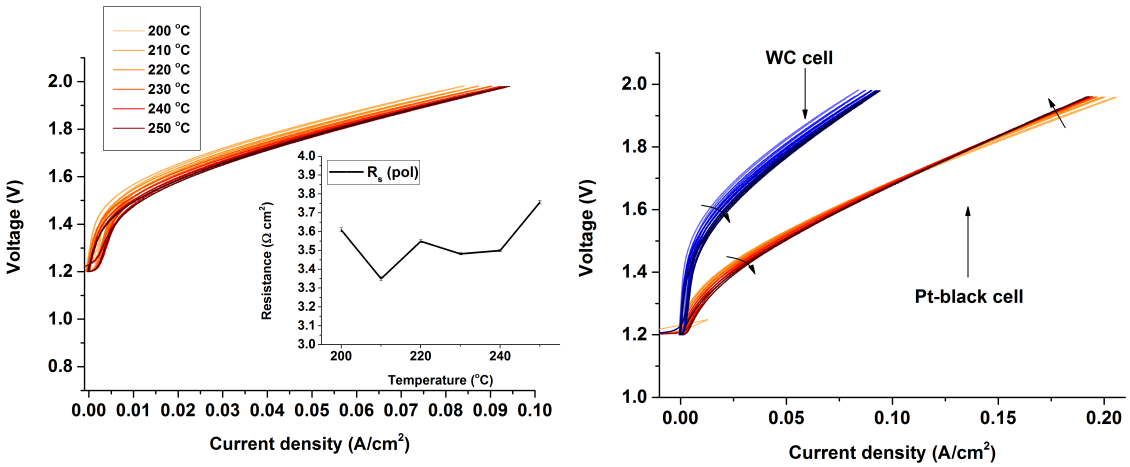

(a) (b)

Figure 9.5: (a) Polarisation curves for a WC(mW_2N) electrocatalyst at 200 to 250 °C (cell SnInP-WC2). (b) The comparison of these results to a Pt black electrocatalyst cell (cell SnInP-Temp2).

polarisation curve lowered with rising temperature indicating increased activity on the electrodes. Fitting of the polarisation curves and estimating the ohmic resistance shows R_s to be changing somewhat erratically (insert in Figure 9.5(a)). One explanation can be that an increase in electrolyte resistance is offset by an electrode component in the estimation from the polarisation curve. Two such battling contributions may give strange results as these.

Figure 9.5(b) compared the Pt black cell and the WC cell. The WC electrocatalyst had a visibly lower performance.

Compared to the behaviour of the Pt black cell the WC cell behaved more as expected

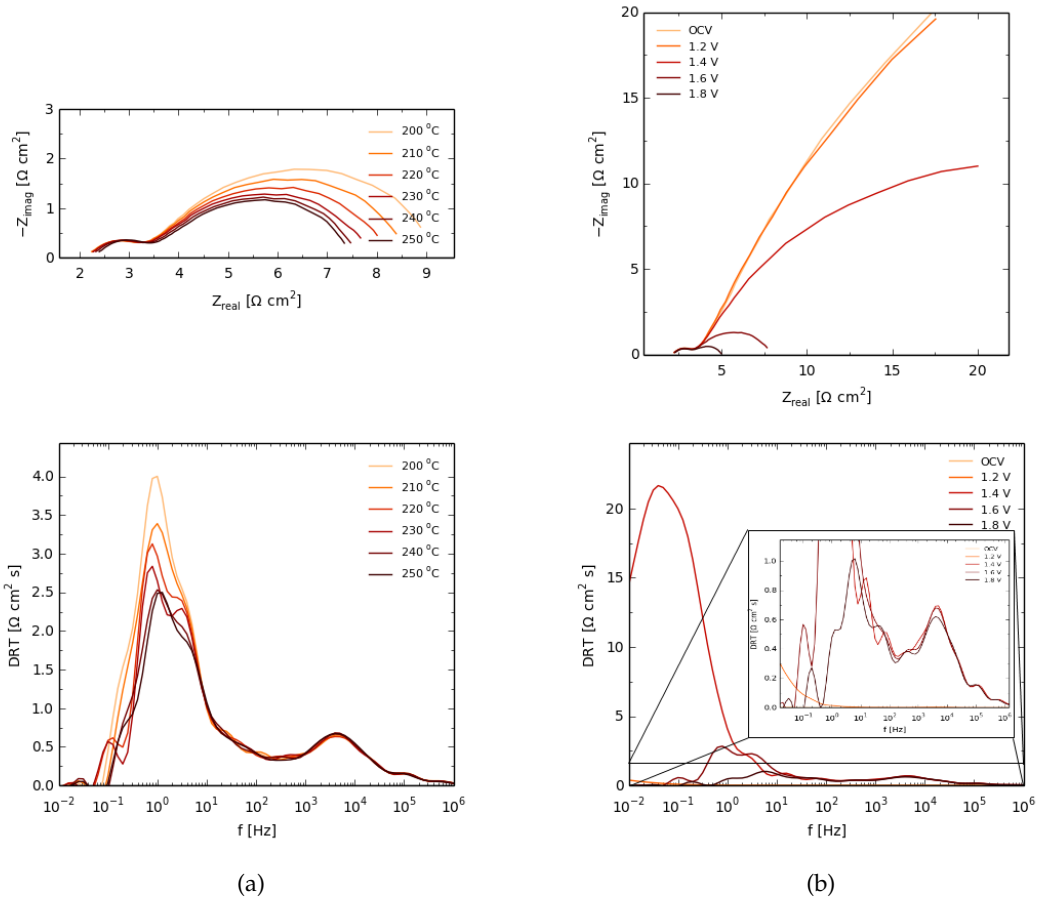

(a) (b)

Figure 9.6: Nyquist plots and DRT over time for a WC electrocatalyst cell (cell SnInP-WC2). (a) is recorded at a polarisation of 1.6V and (b) is recorded at 230 °C.

(Figure 9.6(a)). The high frequency peak (4.2 kHz) was almost unchanged with temperature. In contrast to the Pt cell it may even be slightly activated with temperature. The low frequency peak (1.0 Hz) is clearly activated with temperature. An activation of the sluggish OER on the anode would be expected. This again indicates that the low frequency response is dominated by the processes on the anode.

Looking at Figure 9.6(b) it was seen that the behaviour with voltage of the cell was similar to that seen for cell SnInP-Temp2.

Values for σ_e, R_{p_1} and R_{p_2} were calculated from CNLS fits. The results obtained at 1.8 V are shown in Figure 9.7 and compared with the results from cell SnInP-Temp2. Both electrolytes saw an overall decrease in resistance with temperature. Where cell SnInP-temp2 initially increased slightly cell SnInP-WC2 only decreased. The latter electrolyte exhibited a generally lower conductivity, approximately a difference of $1{\cdot}10^{-2}$ S·cm^{-1}, but otherwise the losses with temperature seemed comparable between the two cells. Both cells

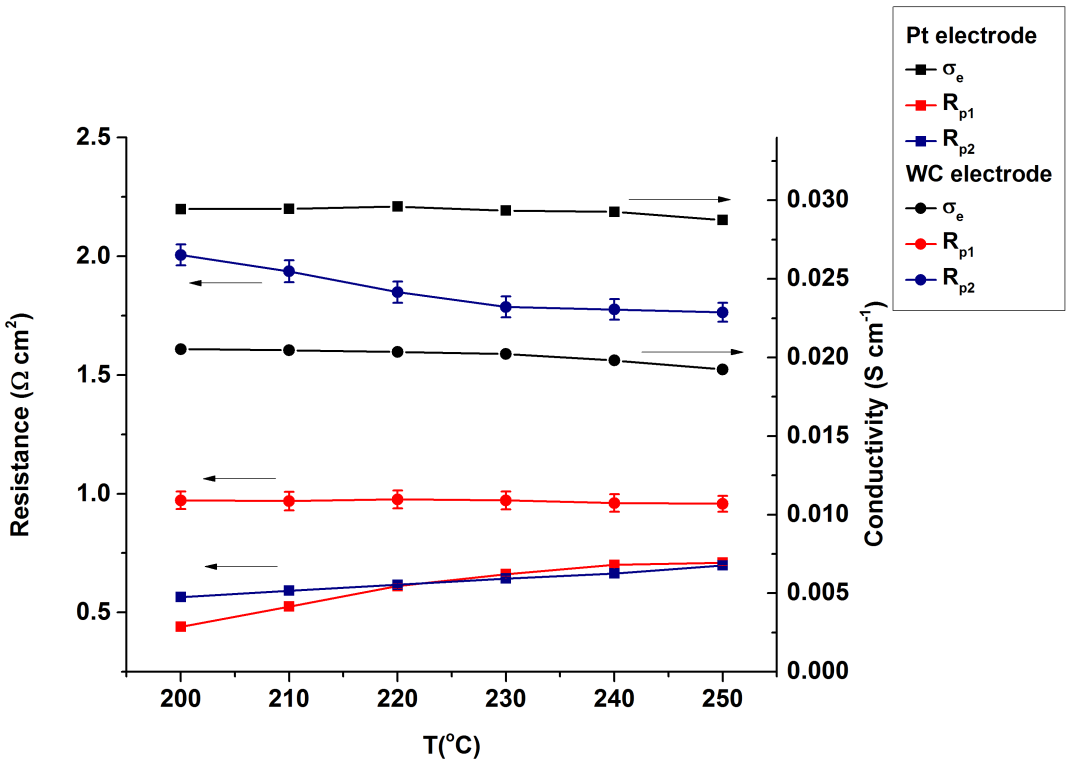

Figure 9.7: Conductivity and resistances as a function of temperature for Pt and WC cathodes obtained at 1.8 V.

were made with the same electrolyte and had similar thicknesses, 0.64 and 0.62 for SnInP-Temp2 and cell SnInP-WC2 respectively. Thus the reason for the difference in electrolyte conductivity is uncertain.

R_{p_1} showed a trend of decreasing with temperature for the WC cell for all applied potentials where an increase was seen for the platinum cell. This points to an activation of the WC electrode while the platinum electrode degrades more than it activates.

R_{p_2} decreases with temperature for all current densities for both cells except for the Pt cell at 1.8 V (only 1.8 V shown). In general R_{p_2} was larger for the WC cell than for the Pt cell. The reason for this is unclear as R_{p_2} should mostly be related to the anode processes and the anodes should be identical for these two cells. If there is a contribution from the cathode to R_{p_2} it may be the reason for the high low frequency polarisation resistance.

These results suggests an improvement of the performance of the WC electrocatalyst with temperature. This is very important for the prospect of using WC at these temperatures and higher. WC could work well with alternative electrolytes capable of functioning at temperatures even higher than 250 °C.

Table 9.4: Components and loadings of $Sn_{0.9}In_{0.1}P_2O_7$ cells with Ni electrodes.

Cell #	Flowplates	Steam	temperature	Impedance	Amplitude
SnInP-Ni-an	2 Ta coated	Steam on anode	200 °C	yes	10 mV
SnInP-Ni-cat	2 Ta coated	Steam on anode	200 °C	yes	10 mV

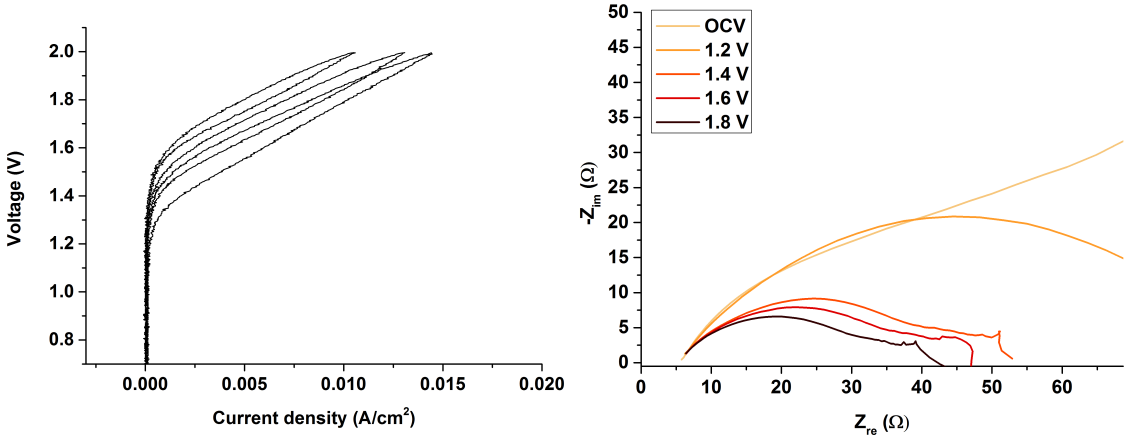

(a) (b)

Figure 9.8: (a)Polarisation curves and (b) Nyquist plots of a $Sn_{0.9}In_{0.1}P_2O_7$ cells with a Ni anode (cell SnInP-Ni-an). Low performance and high instability can be seen. Recorded at 200 °C.

9.2.3 Ni as electrocatalyst

Nickel was tested both as an anode and a cathode material. Figure 9.8(a) shows the polarisation curve of Ni foam used as an anode (cell SnInP-Ni-an). It was seen that the cell performed very poorly with a maximum current density of 15 mA/cm^2 at 2.0 V. The cell even lost performance over the three scans recorded.
Impedance recorded prior to the polarisation showed both high polarisation resistance, high ohmic resistance and only one clearly seen semi circle. Estimating R_e from the impedance data gave an ohmic resistance of 6.64 $\Omega \cdot$ cm^2. This was higher than what has been seen for other cells and could be indicative of contact problems.
The poor performance was thought to be a result of the formation of a thick oxide layer on the surface of the Ni felt or dissolution of metallic nickel. The cell not being stable over polarisation indicates a too acidic environment. Thus the surface acidity of the pyrophosphate lies outside the window of stability for nickel.

The preliminary investigation of Ni as cathode material yields much better results than the testing of Ni as anode material. Again a cut piece of nickel foam was used as combined electrode and GDL. No additional treatment or material was applied. The cell (cell SnInP-Ni-cat) was first tested for one day and then subjected to an additional test of 60 hours. The chosen amplitude for the impedance measurements, 10 mV, was too low giving signal-to-noise problems at low frequencies. Therefore the impedance data for this experiment has not been evaluated by DRT or CNLS.

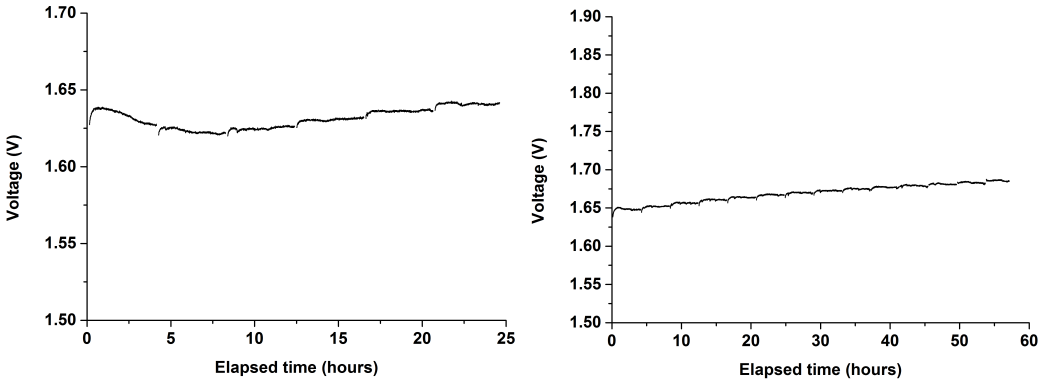

(a) (b)

Figure 9.9: The stability of a Ni cathode electrolyser cell (cell SnInP-Ni-cat). The cell was (a) first tested for 20 hours at 7.5 mA/cm^2 and then (b) 60 hours at 7.5 mA/cm^2.

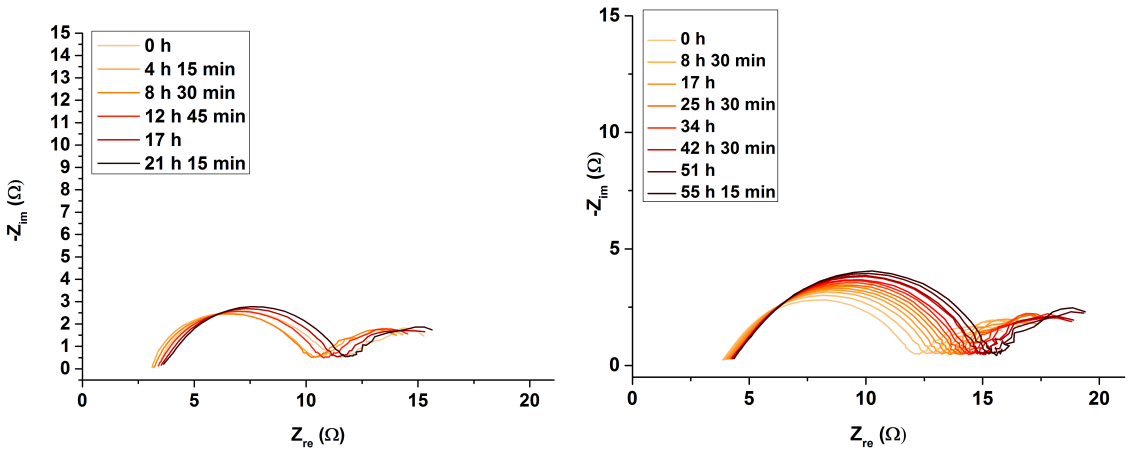

(a) (b)

Figure 9.10: Impedance recorded for a Ni cathode electrolyser cell (cell SnInP-Ni-cat). The impedance is here shown for 1.6V polarisation and (a) recorded the first 20 hours of testing and (b) the next 60 hours of testing.

Figure 9.9(a) and Figure 9.9(b) shows the voltage response of the cell at 7.5 mA/cm^2 over the first 20 hours and the next 60 hours respectively.
Compared to cells with Pt-black as electrocatalyst the voltage was very high. However, the voltage loss over time is small at 1.14 mV/h and 0.70 mV/h for the first and second test respectively. This was comparable to the degradation seen for the Pt black cell named cell SnInP-2xS. It should also be kept in mind that the voltage was much higher at the chosen current density for this cell compared to cell SnInP-2xS. It should be expected that the larger the voltage the faster the degradation. Thus the Ni cell was under harsher conditions but degraded at the same rate as the Pt cell thereby showing a greater stability.
Figure 9.10(a) and Figure 9.10(b) shows impedance recorded at 1.6 V for the first and

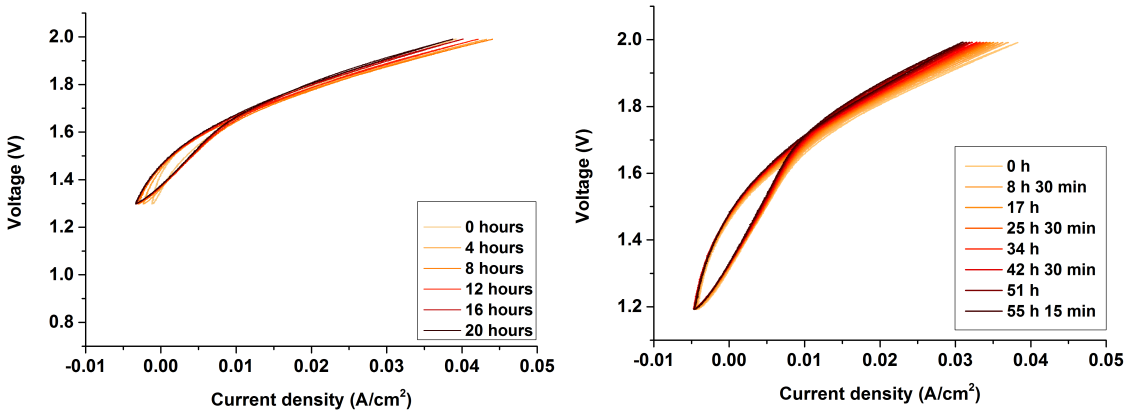

(a) (b)

Figure 9.11: Polarisation curves recorded for a Ni cathode electrolyser cell (cell SnInP-Ni-cat). (a) shows the first 20 hours of testing and (b) shows the next 60 hours of testing.

second test respectively. The ohmic resistance grew over time and so did the polarisation resistance. The growth in ohmic resistance slowed down during the second test but the polarisation resistance did not.
These trends were also found in the polarisation curves for the cell (Figure 9.11(a) and Figure 9.11(b)).
Electrolyte batch H was found to be a bad batch. This can be qualified by Figure 7.4 as seen in Section 7.1.1. Batch (H) appeared to have less or at least less available conducting phase. This would most certainly have influenced the results of this experiment and have a portion of the blame for the high ohmic resistance seen. Nickel may well be a much better electrode material than what these results indicates. A less porous foam combined with an electrolyte with higher conductivity could give a much better cell. As would high surface area Ni powders if sufficiently supported. It is likely that nickel foam could be used as a GDL instead of carbon cloth.

9.2.4 $LaNiO_3$ as anode material

$LaNiO_3$ was used as anode electrocatalyst material (cell SnInP-LNO). It was sprayed onto Ta-coated SSF with 10 % $Sn_{0.9}In_{0.1}P_2O_7$ as binder.

Table 9.5: Components and loadings for a $Sn_{0.9}In_{0.1}P_2O_7$ cell with a $LaNiO_3$ anode (cell SnInP-LNO).

Cell #	Flowplates	Steam	temperature	Impedance	Amplitude
SnInP-LNO	2 Ta coated	Steam on anode	200 °C	yes	10 mV

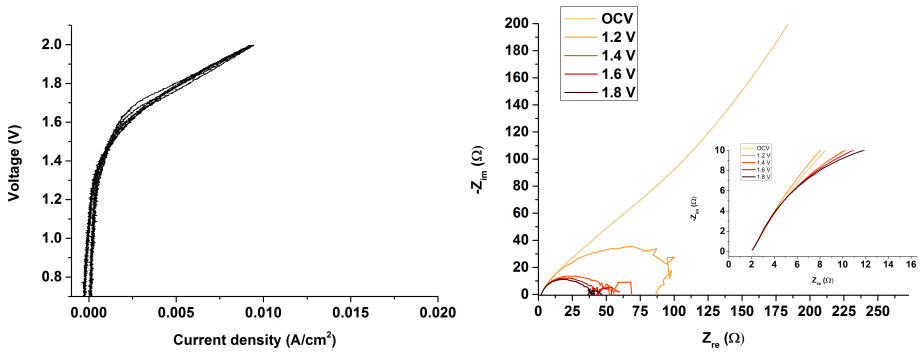

(a) (b)

Figure 9.12: Polarisation curves (a) and impedance (b) recorded for a $LaNiO_3$ anode electrolyser cell.

Cell SnInP-LNO performed poorly. Polarisation reached 2.0 V at a current density of 10 mA/cm^2 (seen Figure 9.12(a)). This high voltage at very low current density made it for all practical purposes impossible to do testing for more than a few minutes.
Impedance data was recorded before the polarisation. As can be seen in Figure 9.12(b) the polarisation impedance for all voltages was very high. Only one semi circle is discernible due to the poorly performing anode dominating all other processes.
While $LaNiO_3$ gave low current densities it was stable over the polarisation experiment. This was considered interesting as the interaction with the somewhat acidic electrolyte and the highly oxidative environment did not destroy the material. Thus perovskites and spinels may be a vein of further study.

9.3 Summary of results for electrocatalysts and electrodes

A $Pt|Sn_{0.9}In_{0.1}P_2O_7|Pt$ hydrogen pump experiment revealed a clear degradation in the previously used Pt black on PTFE stabilised micro-porous cathodes. While the degradation mechanism was not determined it was seen that the polarisation resistance for each of the observed impedance arcs increased threefold. This indicated contact problems or a similar mode of resistance increase. No true stabilisation was seen within the first 120 hours, only a lessening of the loss. Raising the temperature to 250 °C activated one process. The other was not truly evaluable due to large errors from the CNLS fit. The ohmic resistance from the same fit showed a stable electrolyte at 200 °C but clear instability at 250°C. As the electrolyte was old the high temperature instability was ascribed to water uptake and subsequent mobilisation of the conducting phase.
Two types of WC were tested, $WC(mWO_3)$ and $WC(mW_2N)$, as cathode electrocatalysts both showing lower performance than Pt black with highest recorded current densities

being 129 mA/cm^2 and 73 mA/cm^2 at 1.9V respectively. While WC(mWO_3) showed the highest performance WC(mW_2N) showed less loss over time. This may not be absolutes as the electrocatalysts unfortunately were not tested under directly comparable conditions. It was however certain that both materials showed catalytic activity and seemed well suited for practical application in electrolysis. Optimisation of the electrocatalyst and electrode structure could give electrodes with performances closer to that of Pt black and of higher stability.
Testing material WC(mW_2N) at increasing temperature from 200 °C to 250 °C revealed the expected improvement in performance with temperature. No maximum was seen suggesting an even higher gain by further raising the temperature.
Additionally Ni foam was tested as a cathode electrocatalyst and showed a highest initial current density of 40 mA/cm^2. While this is low the stability of the material over the 80 hours tested was high suggesting a possible use as cathode GDL. Furthermore the activity of the material may well be improved as the tested sample was a highly porous piece of foam. A combination of a high surface area materials with a less porous foam as GDL could be a next step.
Ni was also tested as an anode electrocatalyst this time to no great success. The highest initial current density was 15 mA/cm^2 at 2.0V and performance was lost during polarisation. The reason for this was believed to be the formation of a thick oxide layer or the dissolution of Ni. Lastly $LaNiO_3$ was tested as an anode electrocatalyst. While low in activity it was stable over polarisation opening the possibility of other mixed oxides being used.

CHAPTER 10

Conclusion and further work

10.1 Conclusion

This work centred on the design and development of a novel steam electrolysis concept based on phosphate electrolytes capable of operating in the intermediate temperature (IT, 200-400 °C) range. Central for the work was the selection and evaluation of the materials and components for this system as well as technological issues and challenges.
A setup allowing for electrolysis testing up to 400 °C was built. 3 different cell housing designs were produced and two of them were tested in practice. A final design allowing for testing of small electrolyser cells with 1.33 cm^2 active area was selected. Tantalum coating via chemical vapour deposition (CVD) was used to create corrosion resistant layers on components used on the oxidative anode side. Corrosion and formation of a phosphate rich phase was seen on the cathode stainless steel flow plate and the use of Ta coated flow plates on the cathode was introduced to good results.
The surface porosity of Ta coated stainless steel felt gas diffusion layers (GDLs) were found to depend highly on deposition rate of Ta during the chemical vapour deposition. Samples with the least Ta deposited, measured in weight per area, were found to be unusable due to a lack of surface opening. This would make it impossible for steam to reach the electrolyte. Furthermore, a more uniform distribution made the felt easier to cut without breaking the fibres of the felt.
$Sn_{0.9}In_{0.1}P_2O_7$ was used as electrolyte and it was synthesised via a treatment of SnO_2 with phosphoric acid. Investigation of the synthesis showed a dependence of the O-H IR band from 1500 cm^{-1} to 3800 cm^{-1} and the initial heat treatment temperature used in the synthesis. This band had previously been seen to be related to protonic conductivity of the electrolyte material. An initial heat treatment temperature of 270 °C was proposed.
Electrolysis using $Sn_{0.9}In_{0.1}P_2O_7$ as electrolyte, Pt black as cathode electrocatalyst and IrO_2 as anode electrocatalyst gave current densities as high as 313 mA/cm^2 at 1.9 V. Stability of the electrolyte was found to be high at 200 °C. Stability at higher temperatures is dependant on water partial pressure. p_{H_2O}=0.05 atm was insufficient to stabilise a sample at 250 °C. Electrolyte conductivities calculated from impedance estimations of electrolyte resistance were as high as $6.56 \cdot 10^{-2}$ $S \cdot cm^{-1}$, slightly lower than the $7.29 \cdot 10^{-2}$ $S \cdot cm^{-1}$ measured in a dedicated conductivity measurement. This high effective conductivity boded well for the further use of $Sn_{0.9}In_{0.1}P_2O_7$ as electrolyte and indicated thin electrolyte layers as a good avenue for further study.
Variation of temperature from 200-250 °C showed a deactivation of the fast electrode processes with increasing temperature. This was contrary to what would be expected and believed to be caused by electrode degradation.
Testing of a mixture of monoclinic $Bi_2P_4O_{13}$, $BiPO_4$ and 2 wt.% PBI as well as phosphoric

acid treated monoclinic $Nb_5P_7O_{30}$ showed fast degradation and they were deemed unsuitable a electrolytes.
Testing of CsH_2PO_4 as electrolyte revealed a need for steam on both anode and cathode as well as mechanical stabilisation. ZrO_2 and SiC were tested. SiC was found to give the best stabilised composites with a highest measured current density of 60 mA/cm^2 at 2.0 V and 250 °C. Direct comparison with $Sn_{0.9}In_{0.1}P_2O_7$ was not possible as Pt/C was used as cathode electrocatalyst.
Electrodes for hydrogen evolution (HER) consisting of a carbon micro-porous layer with a PTFE binder on carbon paper were found to be unstable at 200 °C and tripled in polarisation resistance over 20 hours. This may have been caused by loss of Pt particles, PTFE softening or degradation of carbon in the electrode.
Testing of $Sn_{0.9}In_{0.1}P_2O_7$ cells with two WC cathode electrocatalysts, named WC(mWO_3) and WC(mW_2N), gave results of 129 mA/cm^2 and 73 mA/cm^2 at 1.9 V respectively. WC(mWO_3) was made by carburisation of WO_3 while WC(mW_2N) was made by converting WO_3 to W_2N and then carburising. The WC(mW_2N) was deemed the most stable. Even though the current densities were low these results were encouraging as many parameters for optimisation are available. One such thing was temperature and it was seen that increased temperature gave better performance. No plateauing was seen at 250 °C boding well for even higher temperature applications.
Ni tested as a cathode electrocatalyst showed fair stability but poor activity. Ni as anode electrocatalyst and $LaNiO_3$ as cathode electrocatalyst were found to be lacking in activity as well as stability.

10.2 Further Work

As with so many aspects of life time was a limiting factor. In the end not all questions raised were answered, far from it. Here are some of the most prominent together with suggested further work.
The exact nature of the stability of $Sn_{0.9}In_{0.1}P_2O_7$ was newer fully resolved. While not a primary point of investigation it was important for much of this work and much would be benefited if this was answered. A series of (long term) experiments testing the conductivity of the material at 200 °C and a range of water partial pressures would illuminate the role of water in the suppression of degradation. Expanding further and testing at multiple temperatures could also resolve whether the conductivity drop seen above 210 °C is caused by degradation and establish whether or not $Sn_{0.9}In_{0.1}P_2O_7$ is suitable for operation at these elevated temperatures.
The exact role of PTFE, carbon and Pt in the degradation of the cathodes is uncertain. While it would at any rate be gainful to remove the PTFE from the electrodes to be able to raise the temperature above 250 °C the other two components would be nice to keep for the time being. Being able to assess components against a well known electrocatalyst makes the work all the easier. A study of the effect of temperature on the micro-porous layer and platinum particles using TEM would be suggested.
WC showed promise in this work. Only very preliminary experiments were done and lots remains to be tested. A simple study of loading of carbide would be an easy way to start. A study of techniques to lower the particle size and supporting said particles would be of great interest. While WC have not shown catalytic activity on the level of Pt its limit has

not been reached in this project and finding ways of testing it a even higher temperatures with alternative electrolytes would be extremely interesting.
Another interesting thread of investigation would be Ni as HER catalyst and cathode GDL alike. In this work a simple piece of high porosity foam was used but a more dimensionally stable sample could conceivably replace the Toray paper which may not itself be stable at the required temperatures. Looking into ways of increasing the active surface area of the nickel material could lead to much better results of the HER as well.

Bibliography

[1] *Key World Energy Statistics 2013*; International Energy Agency, 2013.

[2] *International Energy Outlook 2013*; U.S. Energy Information Administration, 2013.

[3] Hubbert, M. K. *Nuclear Energy and the Fossile Fuels*; Report, 1956.

[4] Luthi, D.; Le Floch, M.; Bereiter, B. et al. High-resolution carbon dioxide concentration record 650,000-800,000 years before present. *Nature* **2008**, *453*, 379–82.

[5] Laboratory, E. S. R. Trends in Atmospheric Carbon Dioxide. 2014; `http://www.esrl.noaa.gov/gmd/ccgg/trends/global.html`.

[6] *Regeringens klimaplan*; Report, 2013.

[7] Moebius, E. Amount of Energy the Earth Gets from the Sun. 2005; `http://cosmicopia.gsfc.nasa.gov/qa_sun.html#sunenergymass`.

[8] Larsen, H., Sønderberg Petersen, L., Eds. *DTU International Energy Report 2013*; Technical University of Denmark, 2013.

[9] *Energiscenarier frem mod 2020, 2035 og 2050*; Report, 2014.

[10] Balat, M. Possible Methods for Hydrogen Production. *Energy Sources, Part A: Recovery, Utilization, and Environmental Effects* **2008**, *31*, 39–50.

[11] Sircar, S.; Waldron, W. E.; Rao, M. B. et al. Hydrogen production by hybrid SMR-PSA-SSF membrane system. *Sep. Purif. Technol.* **1999**, *17*, 11–20.

[12] Andreasen, S. J.; Vang, J. R.; Kær, S. K. High temperature PEM fuel cell performance characterisation with CO and CO2 using electrochemical impedance spectroscopy. *Int. J. Hydrog. Energy* **2011**, *36*, 9815–9830.

[13] Wang, W.; Su, C.; Wu, Y. et al. Progress in solid oxide fuel cells with nickel-based anodes operating on methane and related fuels. *Chem. Rev.* **2013**, *113*, 8104–51.

[14] Onsite®, P. G4800. 2014; `http://protononsite.com/products/g4800/`.

[15] Trasatti, S. Water electrolysis: who first? *J. Electroanal. Chem.* **1999**, *476*, 90–91.

[16] Trasatti, S. 1799-1999: Alessandro Volta's 'Electric Pile': Two hundred years, but it doesn't seem like it. *J. Electroanal. Chem.* **1999**, *460*, 1–4.

[17] Carmo, M.; Fritz, D. L.; Mergel, J. et al. A comprehensive review on PEM water electrolysis. *Int. J. Hydrog. Energy* **2013**, *38*, 4901–4934.

[18] Weber, A. Z.; Newman, J. Effects of Microporous Layers in Polymer Electrolyte Fuel Cells. *J. Electrochem. Soc.* **2005**, *152*, A677.

[19] Gilliam, R.; Graydon, J.; Kirk, D. et al. A review of specific conductivities of potassium hydroxide solutions for various concentrations and temperatures. *Int. J. Hydrog. Energy* **2007**, *32*, 359–364.

[20] Ursua, A.; Gandia, L. M.; Sanchis, P. Hydrogen Production From Water Electrolysis: Current Status and Future Trends. *Proc. IEEE* **2012**, *100*, 410–426.

[21] Appleby, A. J.; Crepy, G.; Jacquelin, J. High-efficiency Water Electrolysis in Alkaline Solution. *Int. J. Hydrog. Energy* **1978**, *3*, 21–37.

[22] Vermeiren, P.; Adriansens, W.; Leysen, R. Zirfon®: A new separator for Ni-H2 batteries and alkaline fuel cells. *Int. J. Hydrog. Energy* **1996**, *21*, 679–684.

[23] Rosa, V. M.; Santos, M. B. F.; da Silva, E. P. New materials for water electrolysis diaphragms. *Int. J. Hydrog. Energy* **1995**, *20*, 697–700.

[24] Pletcher, D.; Li, X. Prospects for alkaline zero gap water electrolysers for hydrogen production. *Int. J. Hydrog. Energy* **2011**, *36*, 15089–15104.

[25] Li, X.; Walsh, F. C.; Pletcher, D. Nickel based electrocatalysts for oxygen evolution in high current density, alkaline water electrolysers. *Phys. Chem. Chem. Phys.* **2011**, *13*, 1162–7.

[26] Allebrod, F.; Chatzichristodoulou, C.; Mogensen, M. B. Alkaline electrolysis cell at high temperature and pressure of 250 °C and 42 °bar. *J. Power Sources* **2013**, *229*, 22–31.

[27] Sone, Y.; Ekdunge, P.; Simonsson, D. Proton Conductivity of Nafion 117 as Measured by a Four-Electrode AC Impedance Method. *J. Electrochem. Soc.* **1996**, *143*, 1254–1259.

[28] Hansen, M. K. PEM Water Electrolysis at Elevated Temperatures. Ph.D. Thesis, 2012.

[29] Hansen, M. K.; Aili, D.; Christensen, E. et al. PEM steam electrolysis at 130 degrees C using a phosphoric acid doped short side chain PFSA membrane. *Int. J. Hydrog. Energy* **2012**, *37*, 10992–11000.

[30] Hauch, A.; Ebbesen, S. D.; Jensen, S. H. et al. Solid Oxide Electrolysis Cells: Microstructure and Degradation of the Ni/Yttria-Stabilized Zirconia Electrode. *J. Electrochem. Soc.* **2008**, *155*, B1184.

[31] Zhang, C.; Li, C.-J.; Zhang, G. et al. Ionic conductivity and its temperature dependence of atmospheric plasma-sprayed yttria stabilized zirconia electrolyte. *Materials Science and Engineering: B* **2007**, *137*, 24–30.

[32] Xu, S.; Li, S.; Yao, W. et al. Direct electrolysis of CO2 using an oxygen-ion conducting solid oxide electrolyzer based on La0.75Sr0.25Cr0.5Mn0.5O3 - δ electrode. *J. Power Sources* **2013**, *230*, 115–121.

[33] Ebbesen, S. D.; Graves, C.; Hauch, A. et al. Poisoning of Solid Oxide Electrolysis Cells by Impurities. *J. Electrochem. Soc.* **2010**, *157*, B1419.

[34] Zahid, M.; Schefold, J.; Brisse, A. In *Hydrogen and fuel cells*; Stolten, D., Ed.; Wiley-VCH Verlag: Weinheim, Germany, 2010; pp 227–242.

[35] Schefold, J.; Brisse, A.; Zahid, M. Electronic Conduction of Yttria-Stabilized Zirconia Electrolyte in Solid Oxide Cells Operated in High Temperature Water Electrolysis. *J. Electrochem. Soc.* **2009**, *156*, B897.

[36] Norby, T. Solid-state protonic conductors: principles, properties, progress and prospects. *Solid State Ionics* **1999**, *125*, 1–11.

[37] Marx, D. Proton transfer 200 years after von Grotthuss: insights from ab initio simulations. *Chemphyschem* **2006**, *7*, 1848–70.

[38] Kreuer, K. D. In *Perovskite Oxide for Solid Oxide Fuel Cells*; Ishihara, T., Ed.; Fuel Cells and Hydrogen Energy; Springer US, 2009; Chapter 13, pp 261–272.

[39] Kreuer, K. D.; Paddison, S. J.; Spohr, E. et al. Transport in proton conductors for fuel-cell applications: Simulations, elementary reactions, and phenomenology. *Chem. Rev.* **2004**, *104*, 4637–4678.

[40] Han, J.; Zhou, X.; Liu, H. Ab initio simulation on the mechanism of proton transport in water. *J. Power Sources* **2006**, *161*, 1420–1427.

[41] Boysen, D. A.; Uda, T.; Chisholm, C. R. et al. High-performance solid Acid fuel cells through humidity stabilization. *Science* **2004**, *303*, 68–70.

[42] Uda, T.; Haile, S. M. Thin-membrane solid-acid fuel cell. *Electrochem. Solid St.* **2005**, *8*, A245–A246.

[43] Haile, S. M.; Boysen, D. A.; Chisholm, C. R. I. et al. Solid acids as fuel cell electrolytes. *Nature* **2001**, *410*, 910–913.

[44] Norby, T.; Friesel, M.; Mellander, B. E. Proton and deuteron conductivity in $CsHSO_4$ and $CsDSO_4$ by in-situ isotopic exchange. *Solid State Ionics* **1995**, *77*, 105–110.

[45] Uda, T.; Boysen, D. A.; Haile, S. M. Thermodynamic, thermomechanical, and electrochemical evaluation of CsHSO4. *Solid State Ionics* **2005**, *176*, 127–133.

[46] Haile, S. M.; Chisholm, C. R. I.; Sasaki, K. et al. Solid acid proton conductors: from laboratory curiosities to fuel cell electrolytes. *Faraday Discuss.* **2007**, *134*, 17.

[47] Taninouchi, Y. K.; Uda, T.; Awakura, Y. et al. Dehydration behavior of the superprotonic conductor CsH_2PO_4 at moderate temperatures: 230 to 260 °C. *J. Mater. Chem.* **2007**, *17*, 3182–3189.

[48] Taninouchi, Y.-k.; Uda, T.; Awakura, Y. Dehydration of CsH_2PO_4 at temperatures higher than 260 °C and the ionic conductivity of liquid product. *Solid State Ionics* **2008**, *178*, 1648–1653.

[49] Park, J.-H. Possible origin of the proton conduction mechanism of CsH_2PO_4 crystals at high temperatures. *Phys. Rev. B* **2004**, *69*.

[50] Kim, G.; Blanc, F.; Hu, Y.-Y. et al. Understanding the Conduction Mechanism of the Protonic Conductor CsH_2PO_4 by Solid-State NMR Spectroscopy. *J. Phys. Chem. C* **2013**, *117*, 6504–6515.

[51] Ikeda, A.; Haile, S. M. The thermodynamics and kinetics of the dehydration of CsH_2PO_4 studied in the presence of SiO_2. *Solid State Ionics* **2012**, *213*, 63–71.

[52] Hallinder, J.; Holtappels, P.; Mogensen, M. B. Electrochemical reduction of CO_2 at temperatures below 300 °C. *E. C. S. Trans.* **2012**, *41*, 61–73.

[53] Hallinder, J. Electrolytes and Electrodes for Electrochemical Cells Operating at 200 - 300 °C. Thesis, 2013.

[54] Ziolek, M. Niobium-containing catalysts–the state of the art. *Catal. Today* **2003**, *78*, 47–64.

[55] Florentino, A.; Cartraud, P.; Magnoux, P. et al. Textural, acidic and catalytic properties of Niobium phosphate and of Niobium oxide - influence of the pretreatment temperature. *Appl. Catal., A* **1992**, *89*, 143–153.

[56] Armaroli, T.; Busca, G.; Carlini, C. et al. Acid sites characterization of niobium phosphate catalysts and their activity in fructose dehydration to 5-hydroxymethyl-2-furaldehyde. *J. Mol. Catal. A: Chem.* **2000**, *151*, 233–243.

[57] Weng, W.; Davies, M.; Whiting, G. et al. Niobium phosphates as new highly selective catalysts for the oxidative dehydrogenation of ethane. *Phys. Chem. Chem. Phys.* **2011**, *13*, 17395–404.

[58] Chai, Z.; Dong, D.; Wang, C. et al. Nanoporous niobium phosphate electrolyte membrane for low temperature fuel cell. *J. Membrane Sci.* **2010**, *356*, 147–153.

[59] Huang, Y. J.; Li, Q. F.; Pan, C. et al. Metal Phosphates as Intermediate Temperature Proton Conducting Electrolytes. *E C S Transactions* **2012**, *45*, 99–104.

[60] Huang, Y.; Li, Q.; Jensen, A. H. et al. Niobium phosphates as an intermediate temperature proton conducting electrolyte for fuel cells. *J. Mater. Chem.* **2012**, *22*, 22452–22458.

[61] Nagao, M.; Kamiya, T.; Heo, P. et al. Proton Conduction in In^{3+} -Doped SnP_2O_7 at Intermediate Temperatures. *J. Electrochem. Soc.* **2006**, *153*, A1604.

[62] Matsui, T.; Takeshita, S.; Iriyama, Y. et al. Proton conductivity of $(NH_4)_2TiP_4O_{13}$-based material for intermediate temperature fuel cells. *Electrochem. Commun.* **2004**, *6*, 180–182.

[63] Matsui, T.; Takeshita, S.; Iriyama, Y. et al. Proton-Conductive Electrolyte Consisting of NH_4PO_3/TiP_2O_7 for Intermediate-Temperature Fuel Cells. *J. Electrochem. Soc.* **2005**, *152*, A167.

[64] Kwon, K.; Yano, M.; Sun, H. et al. New proton conductor comprising tin phosphate useful in a fuel cell (that comprises tin phosphate in its cathode, anode or electrolyte membrane) and in other electrochemical devices such as an electrochemical sensor. 2006.

[65] Nagao, M.; Takeuchi, A.; Heo, P. et al. A Proton-Conducting In^{3+} -Doped SnP_2O_7 Electrolyte for Intermediate-Temperature Fuel Cells. *Electrochem. Solid-State Lett.* **2006**, *9*, A105.

[66] Nagao, M.; Namekata, Y.; Hibino, T. et al. Intermediate-Temperature NO_x Sensor Based on an In^{3+} -Doped SnP_2O_7 Proton Conductor. *Electrochem. Solid-State Lett.* **2006**, *9*, H48.

[67] Nagao, M.; Yoshii, T.; Hibino, T. et al. Electrochemical Reduction of NO_x at Intermediate Temperatures Using a Proton-Conducting In^{3+} -Doped SnP_2O_7 Electrolyte. *Electrochem. Solid-State Lett.* **2006**, *9*, J1–J4.

[68] Wang, H.; Xiao, J.; Zhou, Z. et al. Ionic conduction in undoped SnP_2O_7 at intermediate temperatures. *Solid State Ionics* **2010**, *181*, 1521–1524.

[69] Tao, S. Conductivity of SnP_2O_7 and In -Doped SnP_2O_7 prepared by an aqueous solution method. *Solid State Ionics* **2009**, *180*, 148–153.

[70] Park, C.-J.; Kim, D.-H.; Kim, J.-K. et al. Synthesis of Proton-Conducting, In-Doped SnP_2O_7 Core-Shell-Structured Nanoparticles by Coprecipitation. *J. Electrochem. Soc.* **2009**, *156*, E23.

[71] Nalini, V.; Haugsrud, R.; Norby, T. High-temperature proton conductivity and defect structure of TiP2O7. *Solid State Ionics* **2010**, *181*, 510–516.

[72] Nalini, V.; Sørby, M. H.; Amezawa, K. et al. Structure, Water Uptake, and Electrical Conductivity of TiP2O7. *J. Am. Ceram. Soc.* **2011**, *94*, 1514–1522.

[73] Sato, Y.; Shen, Y.; Nishida, M. et al. Proton conduction in non-doped and acceptor-doped metal pyrophosphate (MP_2O_7) composite ceramics at intermediate temperatures. *J. Mater. Chem.* **2012**, *22*, 3973.

[74] Heo, P.; Shibata, H.; Nagao, M. et al. Performance of an Intermediate-Temperature Fuel Cell Using a Proton-Conducting $Sn_{0.9}In_{0.1}P_2O_7$ Electrolyte. *J. Electrochem. Soc.* **2006**, *153*, A897.

[75] Chen, X.; Wang, C.; Payzant, E. A. et al. An Oxide Ion and Proton Co-Ion Conducting $Sn_{0.9}In_{0.1}P_2O_7$ Electrolyte for Intermediate-Temperature Fuel Cells. *J. Electrochem. Soc.* **2008**, *155*, B1264.

[76] Zhang, H.; Xiao, J.; Yang, Z. et al. Ionic Conduction in In^{3+} -Doped ZrP_2O_7 at Intermediate Temperatures. *Chin. J. Chem.* **2012**, *30*, 1826–1830.

[77] Einsla, M. L.; Mukundan, R.; Brosha, E. et al. In *Proton Exchange Membrane Fuel Cells 8, Pts 1 and 2*; Fuller, T., Shinohara, K., Ramani, V. et al. , Eds.; ECS Transactions; Electrochemical Society Inc: Pennington, 2008; Vol. 16; pp 2165–2170.

[78] Kreller, C. R.; Wilson, M. S.; Mukundan, R. et al. Stability and Conductivity of In^{3+} -Doped SnP_2O_7 with Varying Phosphorous to Metal Ratios. *ECS Electrochemistry Letters* **2013**, *2*, F61–F63.

[79] Xu, X.; Tao, S.; Wormald, P. et al. Intermediate temperature stable proton conductors based upon SnP_2O_7, including additional H_3PO_4. *J. Mater. Chem.* **2010**, *20*, 7827.

[80] Harley, G.; Yu, R.; Dejonghe, L. Proton transport paths in lanthanum phosphate electrolytes. *Solid State Ionics* **2007**, *178*, 769–773.

[81] Heo, P.; Harada, T.; Hibino, T. Nanostructured Pt-$Sn_{1-x}In_xP_2O_7$ Cathodes for High-Temperature Proton Exchange Membrane Fuel Cells. *Electrochem. Solid-State Lett.* **2009**, *12*, B1.

[82] Genzaki, K.; Heo, P.; Sano, M. et al. Proton Conductivity and Solid Acidity of Mg-, In-, and Al-Doped SnP_2O_7. *J. Electrochem. Soc.* **2009**, *156*, B806.

[83] Tomita, A.; Kajiyama, N.; Kamiya, T. et al. Intermediate-Temperature Proton Conduction in Al^{3+} -Doped SnP_2O_7. *J. Electrochem. Soc.* **2007**, *154*, B1265.

[84] Shen, Y.; Kojima, K.; Nishida, M. et al. Proton conduction in $A^{III}_{0.5}B^{V}_{0.5}P_2O_7$ compounds at intermediate temperatures. *J. Mater. Chem.* **2012**, *22*, 14907–14915.

[85] Heo, P.; Shen, Y.; Kojima, K. et al. $Fe_{0.4}Ta_{0.5}P_2O_7$-based composite membrane for high-temperature, low-humidity proton exchange membrane fuel cells. *Electrochim. Acta* **2014**, *128*, 287–291.

[86] Shen, Y.; Heo, P.; Pak, C. et al. Intermediate-temperature, non-humidified proton exchange membrane fuel cell with a highly proton-conducting $Fe_{0.4}Ta_{0.5}P_2O_7$ electrolyte. *Electrochem. Commun.* **2012**, *24*, 82–84.

[87] Lapina, A.; Chatzichristodoulou, C.; Hallinder, J. et al. Electrical conductivity of titanium pyrophosphate between 100 and 400 °C: effect of sintering temperature and phosphorus content. *J. Solid State Electrochem.* **2014**, *18*, 39–47.

[88] Tomita, A.; Yoshii, T.; Teranishi, S. et al. Selective catalytic reduction of NO_x by H_2 using proton conductors as catalyst supports. *J. Catal.* **2007**, *247*, 137–144.

[89] Hibino, T.; Shen, Y.; Nishida, M. et al. Hydroxide ion conducting antimony(V)-doped tin pyrophosphate electrolyte for intermediate-temperature alkaline fuel cells. *Angew. Chem. Int. Ed. Engl.* **2012**, *51*, 10786–90.

[90] Hibino, T.; Kobayashi, K. An intermediate-temperature alkaline fuel cell using an $Sn_{0.92}Sb_{0.08}P_2O_7$-based hydroxide-ion-conducting electrolyte and electrodes. *J. Mater. Chem. A* **2013**, *1*, 1134–1140.

[91] Hibino, T.; Kobayashi, K.; Nagao, M. An all-solid-state rechargeable aluminum-air battery with a hydroxide ion-conducting Sb(v)-doped SnP_2O_7 electrolyte. *J. Mater. Chem. A* **2013**, *1*, 14844.

[92] Man, I. C.; Su, H.-Y.; Calle-Vallejo, F. et al. Universality in Oxygen Evolution Electrocatalysis on Oxide Surfaces. *ChemCatChem* **2011**, *3*, 1159–1165.

[93] Fabbri, E.; Habereder, A.; Waltar, K. et al. Developments and perspectives of oxide-based catalysts for the oxygen evolution reaction. *Catal. Sci. Technol.* **2014**,

[94] Kötz, R.; Lewerenz, H. J.; Stucki, S. XPS Studies of Oxygen Evolution on Ru and RuO_2 Anodes. *J. Electrochem. Soc.* **1983**, *130*, 825–829.

[95] Antonucci, V.; Di Blasi, A.; Baglio, V. et al. High temperature operation of a composite membrane-based solid polymer electrolyte water electrolyser. *Electrochim. Acta* **2008**, *53*, 7350–7356.

[96] Marshall, A.; Børresen, B.; Hagen, G. et al. Hydrogen production by advanced proton exchange membrane (PEM) water electrolysers-Reduced energy consumption by improved electrocatalysis. *Energy* **2007**, *32*, 431–436.

[97] Marshall, A.; Sunde, S.; Tsypkin, M. et al. Performance of a PEM water electrolysis cell using $Ir_xRu_yTa_zO_2Ir_xRu_yTa_zO_2$ electrocatalysts for the oxygen evolution electrode. *Int. J. Hydrog. Energy* **2007**, *32*, 2320–2324.

[98] Di Blasi, A.; D'Urso, C.; Baglio, V. et al. Preparation and evaluation of RuO_2-IrO_2, IrO_2-Pt and IrO_2-Ta_2O_5 catalysts for the oxygen evolution reaction in an SPE electrolyzer. *J. Appl. Electrochem.* **2008**, *39*, 191–196.

[99] Cheng, J. B.; Zhang, H. M.; Ma, H. P. et al. Preparation of $Ir_{0.4}Ru_{0.6}Mo_xO_y$ for oxygen evolution by modified Adams' fusion method. *Int. J. Hydrog. Energy* **2009**, *34*, 6609–6624.

[100] Polonský, J.; Petrushina, I. M.; Christensen, E. et al. Tantalum carbide as a novel support material for anode electrocatalysts in polymer electrolyte membrane water electrolysers. *Int. J. Hydrog. Energy* **2012**, *37*, 2173–2181.

[101] Polonský, J.; Mazúr, P.; Paidar, M. et al. Performance of a PEM water electrolyser using a TaC-supported iridium oxide electrocatalyst. *Int. J. Hydrog. Energy* **2014**, *39*, 3072–3078.

[102] Kjartansdóttir, C. K.; Nielsen, L. P.; MÃ¸ller, P. Development of durable and efficient electrodes for large-scale alkaline water electrolysis. *Int. J. Hydrog. Energy* **2013**, *38*, 8221–8231.

[103] Nikiforov, A.; Petrushina, I.; Jensen, J. O. et al. Corrosion behavior of construction materials for intermediate temperature steam electrolysers. **2013**, *699*, 596–605.

[104] Bockris, J. O.; Otagawa, T. The Electrocatalysis of Oxygen Evolution on Perovskites. *J. Electrochem. Soc.* **1984**, *131*, 290–302.

[105] Mohamed, R.; Fabbri, E.; Levecque, P. et al. Understanding the Influence of Carbon on the Oxygen Reduction and Evolution Activities of BSCF/Carbon Composite Electrodes in Alkaline Electrolyte. *ECS Transactions* **2014**, *58*, 9–18.

[106] Nikiforov, A. V.; Puebla, A. R. d. l. O.; Jensen, J. O. et al. Perovskites As Electrocatalysts for Alkaline Water Electrolysis. *Meeting Abstracts* **2014**, *MA2014-01*, 613.

[107] Loferski, P. J. Platinum-Group Metals. 2014; `http://minerals.usgs.gov/minerals/pubs/commodity/platinum/mcs-2014-plati.pdf`.

[108] Alayoglu, S.; Nilekar, A. U.; Mavrikakis, M. et al. Ru-Pt core-shell nanoparticles for preferential oxidation of carbon monoxide in hydrogen. *Nat Mater* **2008**, *7*, 333–338.

[109] Xu, W.; Liu, C.; Xing, W. et al. A novel hybrid based on carbon nanotubes and heteropolyanions as effective catalyst for hydrogen evolution. *Electrochem. Commun.* **2007**, *9*, 180–184.

[110] Carmo, M.; Sekol, R. C.; Ding, S. et al. Bulk Metallic Glass Nanowire Architecture for Electrochemical Applications. *ACS Nano* **2011**, *5*, 2979–2983.

[111] Hinnemann, B.; Moses, P. G.; Bonde, J. et al. Biomimetic Hydrogen Evolution: MoS_2 Nanoparticles as Catalyst for Hydrogen Evolution. *J. Am. Chem. Soc.* **2005**, *127*, 5308–5309.

[112] Millet, P.; Ngameni, R.; Grigoriev, S. A. et al. PEM water electrolyzers: From electrocatalysis to stack development. *Int. J. Hydrog. Energy* **2010**, *35*, 5043–5052.

[113] Papandrew, A. B.; Zawodzinski, T. A. Nickel catalysts for hydrogen evolution from CsH_2PO_4. *J. Power Sources* **2014**, *245*, 171–174.

[114] Armstrong, R. D.; Bell, M. F. Tungsten carbide catalysts for hydrogen evolution. *Electrochim. Acta* **1978**, *23*, 1111–1115.

[115] Tomas-Garcia, A. L.; Li, Q.; Jensen, J. O. et al. High Surface Area Tungsten Carbides: Synthesis, Characterization and Catalytic Activity towards the Hydrogen Evolution Reaction in Phosphoric Acid at Elevated Temperatures. *Int. J. Electrochem. Sci.* **2014**, *9*, 1016–1032.

[116] Nikiforov, A. V.; Petrushina, I. M.; Christensen, E. et al. WC as a non-platinum hydrogen evolution electrocatalyst for high temperature PEM water electrolysers. *Int. J. Hydrog. Energy* **2012**, *37*, 18591–18597.

[117] Da Silva, L. M.; Franco, D. V.; De Faria, L. A. et al. Surface, kinetics and electrocatalytic properties of $Ti/(IrO_2 + Ta_2O_5)$ electrodes, prepared using controlled cooling rate, for ozone production. *Electrochim. Acta* **2004**, *49*, 3977–3988.

[118] Liu, Z.; Wainright, J. S.; Huang, W. et al. Positioning the reference electrode in proton exchange membrane fuel cells: calculations of primary and secondary current distribution. *Electrochim. Acta* **2004**, *49*, 923–935.

[119] Boukamp, B. A. A Linear Kronig-Kramers Transform Test for Immittance Data Validation. *J. Electrochem. Soc.* **1995**, *142*, 1885–1894.

[120] Boukamp, B. Electrochemical impedance spectroscopy in solid state ionics: recent advances. *Solid State Ionics* **2004**, *169*, 65–73.

[121] Boukamp, B. A. Kramers-Kronig test for Windows. 1999.

[122] Sonn, V.; Leonide, A.; Ivers-Tiffée, E. Combined Deconvolution and CNLS Fitting Approach Applied on the Impedance Response of Technical Ni/8YSZ Cermet Electrodes. *J. Electrochem. Soc.* **2008**, *155*, B675.

[123] Kirkwood, J. G.; Fuoss, R. M. Anomalous Dispersion and Dielectric Loss in Polar Polymers. *J. Chem. Phys.* **1941**, *9*, 329.

[124] Schichlein, H.; Müller, A. C.; Voigts, M. et al. Deconvolution of electrochemical impedance spectra for the identification of electrode reaction mechanisms in solid oxide fuel cells. *J. Appl. Electrochem.* **2002**, *32*, 875–882.

[125] Leonide, A.; Sonn, V.; Weber, A. et al. Evaluation and modeling of the cell resistance in anode-supported solid oxide fuel cells. *J. Electrochem. Soc.* **2008**, *155*, B36–B41.

[126] Graves, C. RAVDAV data analysis software. 2012.

[127] Voorhees, V.; Adams, R. The use of the oxides of platinum for the catalytic reduction of organic compounds I. *J. Am. Chem. Soc.* **1922**, *44*, 1397–1405.

[128] Marshall, A.; Børresen, B.; Hagen, G. et al. Preparation and characterisation of nanocrystalline $Ir_xSn_{1-x}O_2$ electrocatalytic powders. *Mater. Chem. Phys.* **2005**, *94*, 226–232.

[129] Adams, R.; Voorhees, V.; Shriner, R. L. Platinum Catalyst for Reductions. *Org. Synth.* **1928**, *8*, 92.

[130] Depauli, C. P.; Trasatti, S. Electrochemical Surface Characterization of Iro2+Sno2 Mixed-Oxide Electrocatalysts. *J. Electroanal. Chem.* **1995**, *396*, 161–168.

[131] Kishor Mal, N.; Fujiwara, M. Synthesis of hexagonal and cubic super-microporous niobium phosphates with anion exchange capacity and catalytic properties. *Chem. Commun.* **2002**, 2702–2703.

[132] Nikiforov, A. V.; Petrushina, I. M.; Christensen, E. et al. Corrosion behaviour of construction materials for high temperature steam electrolysers. *Int. J. Hydrog. Energy* **2011**, *36*, 111–119.

[133] Selli, E.; Forni, L. Comparison between the surface acidity of solid catalysts determined by TPD and FTIR analysis of pre-adsorbed pyridine. *Microporous Mesoporous Mater.* **1999**, *31*, 129–140.

[134] Desai, P. D.; Chu, T. K.; James, H. M. et al. Electrical Resistivity of Selected Elements. *J. Phys. Chem. Ref. Data* **1984**, *13*, 1069–1096.

[135] Lecuyer, S.; Quemerais, A.; Jezequel, G. Composition of Natural Oxide-Films on Polycrystalline Tantalum Using XPS Electron Take-off Angle Experiments. *Surf. Interface Anal.* **1992**, *18*, 257–261.

[136] Shimizu, K.; Brown, G. M.; Habazaki, H. et al. Direct observation of anodic films formed on tantalum in concentrated phosphoric and sulphuric acid solutions. *Corros. Sci.* **1998**, *40*, 963–973.

[137] Smeltzer, W. W. Oxidation of Aluminum in the Temperature Range 400°C-600 °C. *J. Electrochem. Soc.* **1956**, *103*, 209–214.

[138] Chou, Y.-S.; Thomsen, E. C.; Williams, R. T. et al. Compliant alkali silicate sealing glass for solid oxide fuel cell applications: Thermal cycle stability and chemical compatibility. *J. Power Sources* **2011**, *196*, 2709–2716.

[139] Adler, S. B.; Henderson, B. T.; Wilson, M. A. et al. Reference electrode placement and seals in electrochemical oxygen generators. *Solid State Ionics* **2000**, *134*, 35–42.

[140] Adler, S. B. Reference electrode placement in thin solid electrolytes. *J. Electrochem. Soc.* **2002**, *149*, E166–E172.

[141] He, W.; Nguyen, T. V. Edge Effects on Reference Electrode Measurements in PEM Fuel Cells. *J. Electrochem. Soc.* **2004**, *151*, A185.

[142] Moustafa, Y. M.; El-Egili, K. Infrared spectra of sodium phosphate glasses. *J. Non-Cryst. Solids* **1998**, *240*, 144–153.

[143] Tarafdar, A.; Panda, A. B.; Pradhan, N. C. et al. Synthesis of spherical mesostructured zirconium phosphate with acidic properties. *Microporous Mesoporous Mater.* **2006**, *95*, 360–365.

[144] Aihara, Y.; Sonai, A.; Hattori, M. et al. Ion Conduction Mechanisms and Thermal Properties of Hydrated and Anhydrous Phosphoric Acids Studied with 1H, 2H, and 31P NMR. *The Journal of Physical Chemistry B* **2006**, *110*, 24999–25006.

[145] Risskov Søe rensen, D.; Nielsen, U. G.; Skou, E. M. Solid state 31P MAS NMR spectroscopy and conductivity measurements on NbOPO4 and H3PO4 composite materials. *J. Solid State Chem.* **2014**, *219*, 80–86.

[146] Jespersen, J. L. k.; Schaltz, E.; Kæ r, S. r. K. Electrochemical characterization of a polybenzimidazole-based high temperature proton exchange membrane unit cell. *J. Power Sources* **2009**, *191*, 289–296.

[147] Tamayama, M.; Andersen, T. N.; Eyring, H. Melting and Pyrolysis of Teflon and Melting of Silver Chloride and Iodine under High Pressure. *Proceedings of the National Academy of Sciences of the United States of America* **1967**, *57*, 554–561.

[148] Linkous, C. A. Development Of Solid Polymer Electrolytes For Water Electrolysis At Intermediate Temperatures. *Int. J. Hydrog. Energy* **1993**, *18*, 641–646.

[149] Otomo, J.; Tamaki, T.; Nishida, S. et al. Effect of water vapor on proton conduction of cesium dihydrogen phosphateand application to intermediate temperature fuel cells. *J. Appl. Electrochem.* **2005**, *35*, 865–870.

[150] Anfimova, T. Metal Phosphates as Proton Conducting Materials for Intermediate Temperature Fuel Cell and Electrolyser Applications. Thesis, 2014.

[151] Schmidt, J. P.; Berg, P.; Schönleber, M. et al. The distribution of relaxation times as basis for generalized time-domain models for Li-ion batteries. *J. Power Sources* **2013**, *221*, 70–77.

APPENDIX **A**

Appendix

A.1 Kramers-Kronig relation and derivation

If the four conditions mentioned in Section 4.2.4, causality, linearity, stability and finiteness, are fulfilled by a data set then the Kramers-Kronig relation states that the imaginary and real part of the impedance are interdependant. More specifically the real impedance can be calculated by one of the following equations:

$$\mathrm{Z_{re}}(\omega) = \mathrm{R}_\infty + \frac{2}{\pi}\int_0^\infty \frac{\mathrm{x}\mathrm{Z_{im}}(x) - \omega \mathrm{Z_{im}}(\omega)}{\mathrm{x}^2 - \omega^2} d\mathrm{x} \tag{A.1}$$

$$\mathrm{Z_{re}}(\omega) = \mathrm{R}_\infty + \frac{2\omega}{\pi}\int_0^\infty \frac{(\omega/\mathrm{x})\mathrm{Z_{im}}(x) - \mathrm{Z_{im}}(\omega)}{\mathrm{x}^2 - \omega^2} d\mathrm{x} \tag{A.2}$$

A few things should be noted here. Some systems will show a ohmic resistance when $\mathrm{Z}(\omega) \rightarrow \mathrm{Z}(\infty)$ ($\mathrm{R_{ohm}}$). Others will show a DC resistance at $\mathrm{Z}(\omega) \rightarrow \mathrm{Z}(0)$ (R_0). Both are not transformable by KK transformation as can be seen from Equations A.1 and A.2. This is due to them only having real values. This means that for high quality data this is a means of finding these resistances as the difference between the transformed data and the recorded data at all frequencies will be said resistance. Care must however be taken as a systematic error can hide in this difference.
The imaginary part can be calculated as:

$$\mathrm{Z_{im}}(\omega) = \frac{2\omega}{\pi}\int_0^\infty \frac{\mathrm{Z_{re}}(x) - \mathrm{Z_{re}}(\omega)}{\mathrm{x}^2 - \omega^2} d\mathrm{x} \tag{A.3}$$

While not included this equation as an analog to the resistances seen in the previous two equations. If a stray inductance, or any inductor not in parallel with another circuit element, is present it will not be transformed by this transformation as it only has an imaginary part. This is often used to do inductanse corrections of data as any discrepancy between measured data and calculated data is assumed to be inductive in nature. This in of cause dangerous as real errors may hide in the supposed inductance.
These equations are as previously mentioned only valid for data over the entirety of frequencies. As this is a physical impossebility to record the data must be extended to (approximately) $\omega = 0$ and $\omega = \infty$. The method used in this work is based on the work of Boukamp.[119] Here the data was fitted to a series of parallel RC circuits. Every circuit has a time constant associated with it defined as $\tau_\mathrm{k} = \mathrm{R_k C_k}$. For a data set of N values M time constants are distributed over the range of the data and $\tau_1 = \omega_1^{-1}$ and $\tau_M = \omega_N^{-1}$ with M<N. The impedance is the simulated by:

$$\mathrm{Z}(\omega_\mathrm{i}) = \mathrm{R}_\infty + \sum_{\mathrm{k}=1}^{M} \mathrm{R_k}\{\frac{1}{1+\omega_\mathrm{i}^2\tau_k^2} - \mathrm{i}\frac{\omega_\mathrm{i}\tau_\mathrm{k}}{1+\omega_\mathrm{i}^2\tau_k^2}\} \tag{A.4}$$

The difference between the original data set and the calculated data set is a set of linear equations which may be solved by simple matrix manipulation. Residuals may then be calculated between the original data set and the fit and these residuals are then the basis of the evaluation of the KK test. If no clear system of the residuals around the frequency axis is observed and the residuals are small then the data set can be said to fulfill the KK requirements.

A.2 An elaboration on the concepts of Distribution of Relaxation Times

As mentioned in Section 4.2.5 the polarisation impedance of a given system can be described by the convolution equation 4.5:

$$Z_{pol}(\omega) = R_{pol} \int_0^\infty \frac{\gamma(\tau)}{1 + i\omega\tau} d\tau, \qquad \int_0^\infty \gamma(\tau) d\tau = 1 \tag{A.5}$$

This means that the polarisation impedance can be interpreted as the sum on an infinite number of RC circuits. Due to the discrete and finite nature of impedance measurements this expression cannot be solved analytically. Instead the impedance data is extrapolated to as near infinity as possible by Kramers-Kronig and is fitted to a finite series of N RC circuits. As τ = RC this means that N relaxation times are treated. This is done in discreet intervals which are equidistant on a logarithmic scale. This means that the polarisation impedance is approximated by the following finite sum:[151]

$$Z_{pol}(\omega) \approx R_{pol} \sum_{n=1}^{N} \frac{g_n}{1 + i\omega\tau_n} \delta_\tau \tag{A.6}$$

where g_n is the desired distribution function, τ_n is the n^{th} relaxation time and δ_τ is the distance between relaxation times on a log scale. The n^{th} resistance contribution, the resistance contribution for a given relaxation time, can be calculated by $R_n = g_n \cdot \delta_\tau \cdot R_{pol}$. Similarly the n^{th} capacitance contribution can be calculated by $C_n = \tau_n / R_n$. This is the reason why $\gamma(\tau)$ can be seen as the contribution distribution of R_{pol}.
The above discrete form of the function is what the data is fitted to and the result is then Fourier transformed. A suitable number of relaxation times, N, and frequency range is chosen for the fitting of the obtained data. When the fitted data is transformed it is filtered and transformed back to obtain g(f), which is the approximated distribution of relaxation times. g(f) is a continuous function of frequency.
When g(f) is presented it is always normalised to R_{pol} so integration over the entire function gives R_{pol}. While this is sensible it is a bit of a trap to unsuspecting readers as the phrasing used gives the impression that g is presented in its raw form. Usually only the unit gives this away.

A.3 FT-IR

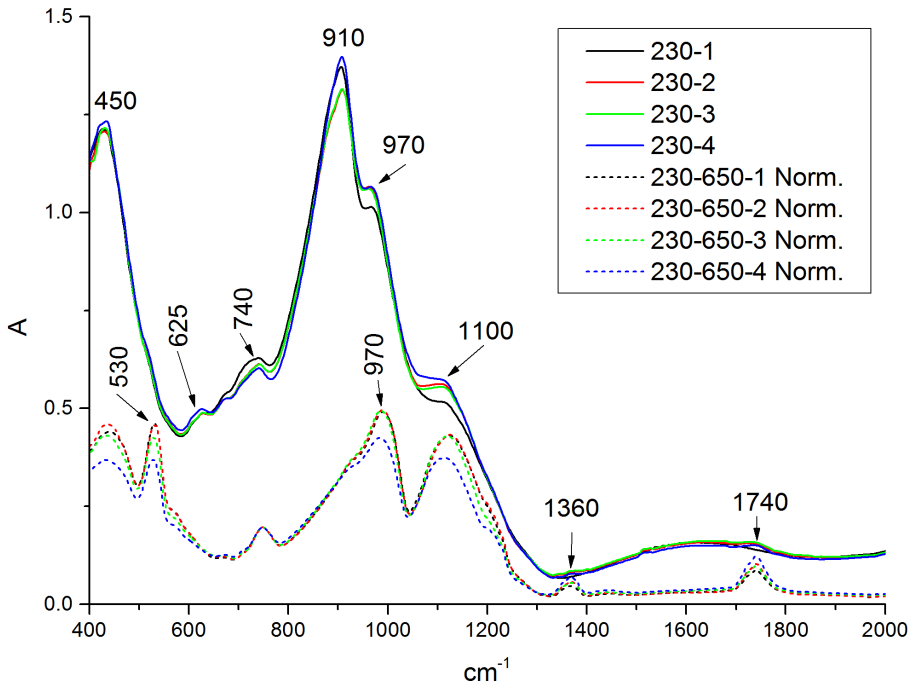

Figure A.1: IR spectrum of samples pre heated to 230 °C

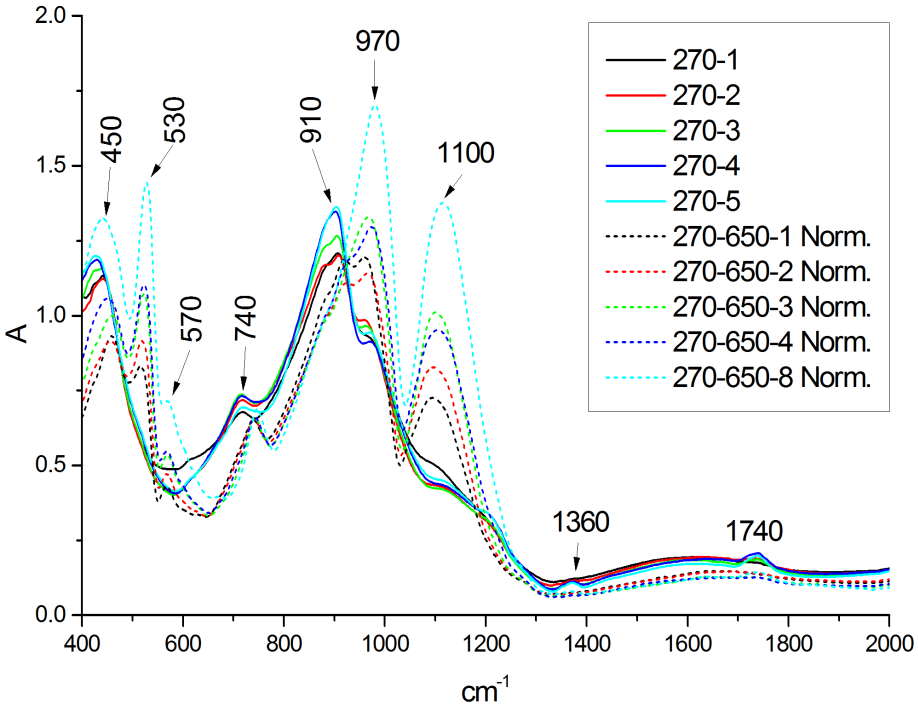

Figure A.2: IR spectrum of samples pre heated to 270 °C

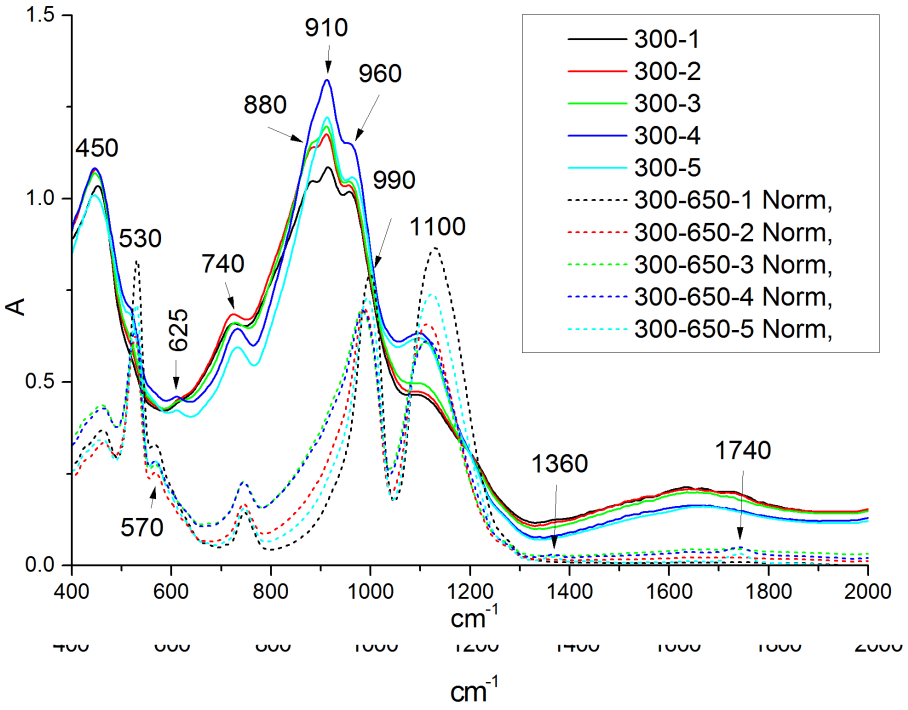

Figure A.3: IR spectrum of samples pre heated to 300 °C